Politecnico di Torino

Politecnico di Torino

Academic Year 2024/25

Master's Thesis in Aerospace Engineering

Multibody analysis of a space debris capture mechanism based on origami principle

Supervisors:
Prof. Alfonso Pagani
Ing. Daniele Catelani

Candidate:
Giuseppe Balsamo

Abstract

The issue of space debris is one of the greatest challenges that space exploration and utilization face today. It refers to the accumulation of non-functional artificial objects orbiting the Earth, such as decommissioned satellites, spacecraft fragments, rocket stages. These debris pose an increasing risk to operational satellites, crewed space missions, and space infrastructure such as the International Space Station. Preventive measures and regulations are therefore necessary to mitigate the problem. For some time now, the European Space Agency has been working to ensure that new space missions have a deorbiting time of no more than five years.

In addition to these regulations, dedicated space missions have been developed with the goal of Active Debris Removal (ADR). This work contributes to the ADR field through the design and analysis of a debris capture system inspired by Origami principles, which allow for compact storage and lightweight yet mechanically robust deployable structures. The central contribution of this study is the development of a methodology for the sizing of the actuation system and the subsequent definition of its architectural design. A further contribution lies in the modeling of structural flexibility, which was introduced to better capture the realistic dynamic behavior of the system.

The multibody simulation environment is utilized to evaluate the deployment sequence and to study the forces and torques involved. A comparative analysis is also carried out between rigid-body and flexible-body modeling, highlighting the impact of flexibility on the overall performance and precision of the actuation system.

The system is designed for operations in Low Earth Orbit, a favorable yet challenging environment due to factors such as gravitational gradients and radiation effects that can influence both structural and control performance.

Contents

Acronyms

ESA	European Space Agency
ISS	International Space Station
IADC	Inter-Agency Space Debris Coordination Committee
LEO	Low Earth Orbit
GEO	Geostationary Earth Orbit
CMS	Component Mode Synthesis
FEA	Finite Element Analysis
MNF	Modal Neutral File
MPC	Multipoint Constraint
DOF	Degree Of Freedom
CFRP	Carbon Fiber Reinforced Polymer
RVM	Requirements Validation Matrix
PD	Proportional-Derivative
ECSS	European Cooperation for Space Standardization
VP	Verification Plan
UHMPWE	Ultra-High Molecular Weight Polyethylene
SAF	Short Aramid Fiber

List of Figures

Chapter 1

Introduction

Since the moment humankind first looked up at the sky and began asking questions about the universe, interest in space has grown, driven by curiosity, a spirit of adventure, and an intrinsic desire for knowledge.
However, one of the main challenges in space exploration and utilization is represented by space debris. These consist of fragments from satellites, rockets, and other artificial objects orbiting the Earth, released during space launches or as a result of collisions.
With the exponential increase in space activities over the past decades, the number of these debris has dramatically grown, posing a serious threat to both active satellites and the International Space Station (ISS). Even small fragments, due to the high velocities at which they travel in orbit, can cause significant damage to space infrastructure.
The proliferation of space debris raises critical challenges for safety and sustainability: each collision can generate additional fragments, triggering a chain reaction known as the *Kessler syndrome* (named after Donald J. Kessler, a NASA consultant in 1978), which could render certain orbits unusable in the future. Moreover, the increasing commercial use of space, with the launch of mega-constellations of satellites, has intensified the need for effective solutions to manage and mitigate this issue.
In the contemporary era, the management of space debris has emerged as a matter of shared global concern. Space agencies around the world are collaborating to develop common strategies for ensuring the safety and sustainability of Earth orbit. Moreover, the entry of private operators into the space sector has accentuated the need for effective solutions to avoid major economic losses and ensure the continuity of space services. These services are critical for telecommunications, meteorology, navigation, and national security.

Several solutions have been proposed to address this problem, primarily focusing on **prevention** of the creation of new debris and **removal** of existing ones. Regarding prevention, space agencies and regulatory bodies are developing regulations that require private companies and states to follow stricter protocols for debris control, such as the requirement to de-orbit satellites within a certain timeframe after the end of their mission.

Among the active debris removal solutions, there are satellites capable of capturing or disintegrating smaller debris. An innovative idea in this field is the

use of structures based on the *origami principle*. Origami, from the Japanese words "Ori" (fold) and "Kami" (paper), has found applications in engineering in recent years. The growing interest in this technique is due to the inherent properties of origami, namely compactness and lightweight design, as well as their adaptability to complex mission profiles. Origami-based mechanisms offer a unique balance between structural stiffness in the deployed phase and high compliance during folding, making them particularly suitable for space environments, where constraints on volume and mass are critical. Some examples of aerospace applications include deployable antennas and foldable solar panels.

In this study, a model of a capture system based on the origami principle will be introduced and refined from a structural perspective by incorporating flexible bodies. The goal is to size the actuation mechanism and assess the feasibility of such a prototype. The study will be conducted through a multi-body analysis using the MSC Adams software.
Multibody dynamics simulation is an engineering method employed for the digital modeling of systems comprising numerous interconnected components. Due to the intricate nature of these systems, which encompass numerous bodies in constantly evolving states of motion, multibody dynamics simulation is imperative for predicting the complete behavior and structural integrity of the system. This approach also ensures the avoidance of physical testing expenses, as any design issues can be identified prior to the construction of the entire system.

1.1 Space debris

In 2002, the Inter-Agency Space Debris Coordination Committee (IADC), of which ESA is a member, published the Space Debris Mitigation Guidelines, which outline how to design, operate, and dispose of space missions to prevent the creation of additional debris.

Since 2016, ESA's Space Debris Office has been publishing an annual report on the space environment (*Space Environment Report* [1]) to provide a transparent overview of global space activities. It also assesses to what extent these and other international debris reduction measures are improving the long-term sustainability of spaceflight.
The amount of space debris in orbit continues to grow rapidly. Approximately 35,000 objects are currently tracked by space surveillance networks. Around 9,100 of these are active payloads, while the remaining 26,000 are debris fragments larger than 10 cm.

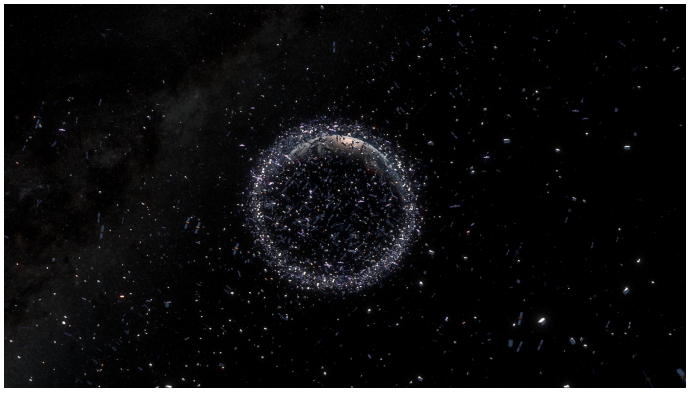

Figure 1.1: Orbiting objects around the Earth

However, the estimated number of space debris with dimensions greater than 1 cm (large enough to cause catastrophic damage) exceeds one million. The 2024 report highlights a significant increase in debris, particularly over the past fifteen years, mainly due to the growing number of satellite launches and space missions.

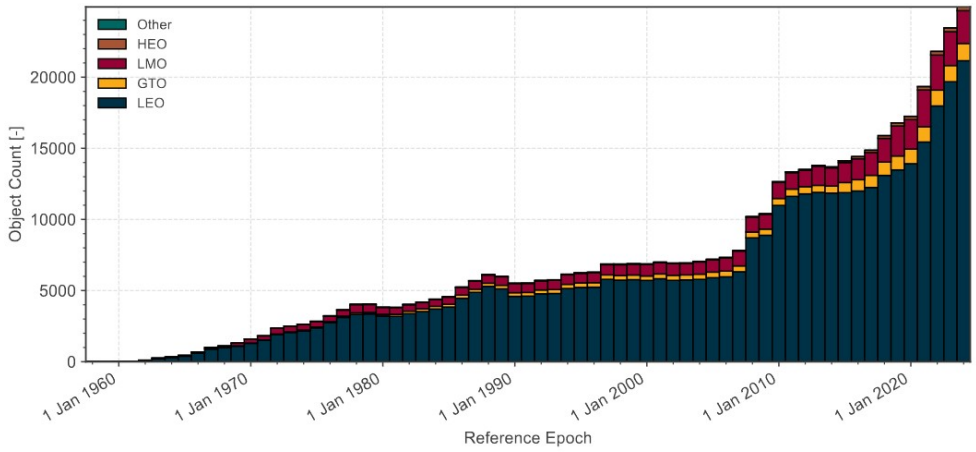

Figure 1.2: Evolution of the number of objects launched in orbit over the years

Within Low Earth Orbit (LEO), there are preferred altitude ranges for communication constellations, leading to a clear peak in satellite concentration. This trend is expected to continue, as the majority of new satellites launched in 2023 were also directed toward these orbits. In recent years, efforts to improve compliance with space debris mitigation guidelines have intensified, aiming to remove end-of-life satellites from critical orbits. This has led to a rapid increase in the number of satellites re-entering the atmosphere.

The 2024 Space Environment Report assessed all tracked objects against the 25-year compliance rule in effect in 2023. In the next edition, new ESA debris mitigation guidelines will be introduced; among other changes, the time required to vacate valuable orbits will be reduced from 25 to 5 years.
There are several causes of debris formation:

- **Collisions between spacecraft and space objects**: when two satellites or other in orbit objects collide, they generate thousands of fragments (one example is the 2009 collision between the Russian satellite Cosmos 2251 and the American commercial satellite Iridium 33).

- **Spacecraft and rockets explosions**: after a satellite launch, some parts of the rocket remain in orbit. These upper rocket stages can explode due to leftover fuel or tank malfunctions. Explosions release numerous fragments into orbit. Satellites can also explode due to malfunctions or collisions with other debris.

- **No more operative spacecraft**: many satellites at the end of their operational life, as well as equipment used during space missions (such as solar panels, instruments, and covers), remain in orbit, becoming debris.

- **Anti-Satellite Weapon Tests (ASWT)**: these tests deliberately destroy a satellite in orbit, releasing numerous fragments. A recent example is the test conducted by China in 2007, which destroyed the Fengyun-1C satellite, generating thousands of hazardous fragments.

- **Release of Objects During Space Operations**: during crewed space missions, small objects such as tools, bolts, covers, can be accidentally released. These objects, even if small, can become hazardous debris.

According to the numbers provided by ESA, the objects orbiting the Earth are categorized in percentages as shown in Figure 1.3. This highlights the importance of de-orbiting end-of-life satellites, as well as the breakthrough achieved with reusable rockets. Debris, regardless of their origin, poses several challenges to space utilization.
Such debris can threaten crewed space missions, as a fragment could puncture the protective shielding of the International Space Station (ISS), endangering the lives of astronauts.
Additionally, space debris travel at extremely high velocities, meaning even a small fragment can cause significant damage to operational satellites, disrupting communications, GPS navigation systems, and Earth monitoring. As a result, space agencies and private companies must allocate substantial resources to avoid collisions, including continuous monitoring and evasive maneuvers (which require fuel consumption).

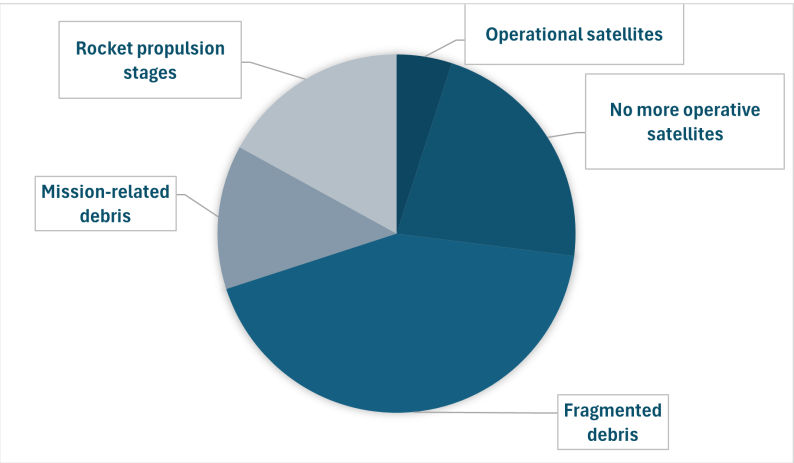

Figure 1.3: Classification of objects in orbit

The increasing amount of debris is further reducing the available space for new satellites, particularly in LEO and Geostationary Earth Orbit (GEO), the most crowded regions.

1.1.1 Kessler Syndrome

As the number of artificial satellites in Earth's orbit increases, the probability of satellite collisions also rises. Collisions between satellites can generate fragments in orbit, thus further increasing the likelihood of additional collisions, leading to the growth of a debris belt around Earth. The flow of debris in such a belt orbiting Earth could exceed the natural influx of meteoroids, affecting the design of future spacecraft.

In 1978, NASA astrophysicist Donald J. Kessler demonstrated that debris in LEO orbits, through a chain reaction of collisions, could lead to the formation of a belt similar to those of meteoroids, with a relatively rapid process if the production trend remained unchanged [3].
The hypothesized scenario was named the Kessler Syndrome:

> *"We will eventually reach a point where accessing space will become nearly impossible because the density of debris will be so high that collisions—creating even more debris—will be more likely than avoiding them, making successful space missions increasingly difficult."*

Long-term simulations conducted by ESA indicate that, within a few decades, fragments generated by collisions will dominate orbits between 800 and 1,400 km.
The IADC has carried out studies including mega-constellations of small satellites in LEO, concluding that a chain reaction could be triggered between 900 and 1,400 km due to the density of debris and the insufficient effect of atmospheric drag.
These long-term simulations take into account compliance with the *space debris mitigation guidelines.*

1.1.2 Mitigation strategies

As previously mentioned, mitigation strategies are divided into **preventive** measures and **active** removal methods.

Among the preventive measures, ESA has imposed a reduction in the disposal phase of satellites from 25 years to a maximum of 5 years after the end of the mission, with a disposal success probability greater than 90%.
In addition to developing stricter regulations, preventive measures include *Collision Avoidance* maneuvers: the collision event is identified, the risk is analyzed (by comparing the probability of collision with the accepted risk level), and separation maneuvers—either temporal or spatial—are applied.
Furthermore, monitoring and identifying existing debris is crucial, using telescopes, radars, and lasers.

In addition to preventive measures, there are methods that allow for the active removal of debris:

- **Capture with robotic arm**, widely used and easily testable on Earth.
- **Capture with net**, difficult to test on Earth, but effective on a wide variety of debris and does not require precise thrust accuracy.
- **Space harpoon**, a well-known technology on Earth, but it carries the risk of generating additional debris since it is difficult to predict how the target will react upon impact.
- **Ground-based or space-based laser system**, which can be used to alter the trajectory of debris by applying a force through laser ablation, gradually lowering their orbit until they burn up in the atmosphere.

These types of devices include origami-based mechanisms, which will be presented in this study.

(a) Capture with robotic arm

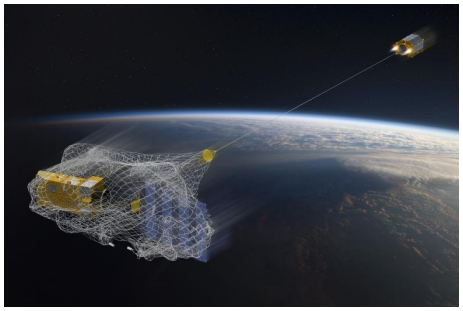

(b) Capture with net

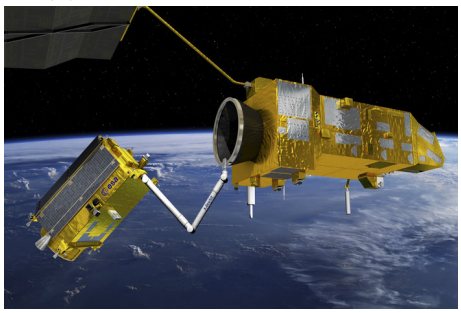

(c) Space harpoon

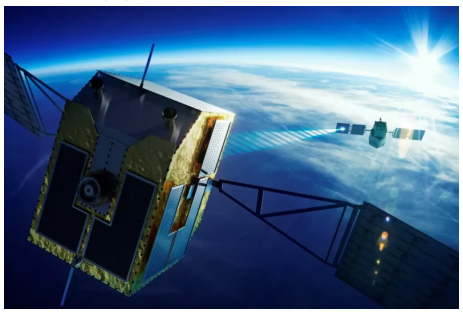

(d) Space-based laser system

Figure 1.4: Active removal of debris

1.2 Origami and Engineering

The term *Origami*, from Japanese *Ori* (fold) and *kami* (paper), refers to the ancient Japanese art in which, through paper folding, different shapes are created without using traditional cutting or gluing techniques.
Having gained worldwide popularity in the 1950s thanks to the Japanese artist Akira Yoshizawa, origami has captured the attention of mathematicians and engineers, finding applications in various fields—from aluminum cans to solar sails for satellites—due to the scalability of this technique. Mathematical principles have been applied to real origami structures, leveraging the advantage of having a fully defined three-dimensional model derived from its corresponding two-dimensional flat pattern. It is therefore easy to understand the importance of such structures in the aerospace field, as they allow for volume savings in their compact launch configuration while maximizing surface area in their deployed configuration.

1.2.1 The folding

At the geometric level, a fold is the result of the movement of a flat surface. At the mechanical level, this translates into an improvement in the structural characteristics of the quintessential flat element, the plate. By applying a fold, material is placed farther from the neutral plane, increasing the moment arm of bending stresses. Consequently, loads are transmitted differently, allowing for increased structural stiffness while minimizing material usage.
However, structures cannot be obtained by folding the material arbitrarily. A developable structure has zero Gaussian curvature everywhere.
As thoroughly delineated in the work [5], the Gaussian curvature of a surface K is defined as follows:

$$K = k_1 k_2$$

where k_1 and k_2 are the principal curvatures of the surface.
According to this, surfaces are divided into:

- $K > 0$: elliptical points. The two curvatures have the same sign, either both positive (the surface is convex), or both negative (the surface is concave). In both cases, the surface bends in the same manner in all directions.

- $K < 0$: hyperbolic points. One principal curvature is positive, the other is negative. At these points the surface bends in opposite directions, in one direction the surface is convex, in the other it is concave.

- $K = 0$: at least one of the two principal curvatures is zero. This does not mean that the surface is flat. If only one of the two curvatures is zero, then the surface is flat in one direction, but curves in the other, and in this case the point is called a parabolic point. If on the other hand $k_1 = k_2 = 0$, then the surface does not curve in any direction and the point is called planar. Under these conditions the fundamental second quadratic form vanishes, but this does not necessarily imply that the surface is locally flat. The local shape is determined by the higher order terms in Taylor's development.

At each point on a surface, a tangent plane can be identified. The normal vector $\hat{n}$ is defined as a unit vector that is perpendicular to the tangent plane. That is to

say, it represents the direction perpendicular to the surface at a given point.
Moving along the surface, this direction can change, and the more it changes, the more the surface is curved in that direction. This curvature is called *normal curvature*.
Since the normal is a versor, i.e. a vector of modulus 1, each normal corresponds to a point on the unit sphere S^2 (the sphere of radius 1 centred in the origin).
The Gauss map transfers the surface $\sigma(u, v) : U \to \mathbb{R}^3$ onto the sphere S^2 according to how the normals change.
The integral of the Gauss curvature over the entire surface represents the total curvature.

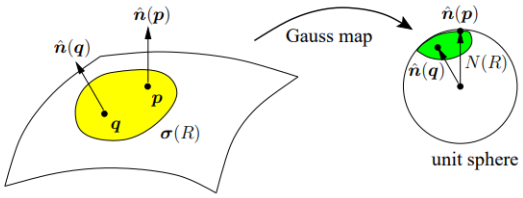

Figure 1.5: Gaussian map [5]

1.2.2 Aerospace applications

In addition to what has already been mentioned, origami are of great interest in the aerospace field as they allow the structure to be folded and unfolded with a single continuous movement, saving volume in the payload.
Here there are some examples of the use of origami systems in the aerospace field.

Solar sail

A first practical example of origami applications in the space sector is that of a solar sail, based on the *Miura-Ori* pattern. It relies on inverse folding and consists of a series of parallelograms arranged in a herringbone pattern, alternating valley and mountain folds in both directions. This configuration exhibits different behaviors in-plane and out-of-plane: during compression and tension, it has a negative Poisson's ratio, while it becomes positive under bending and torsion.

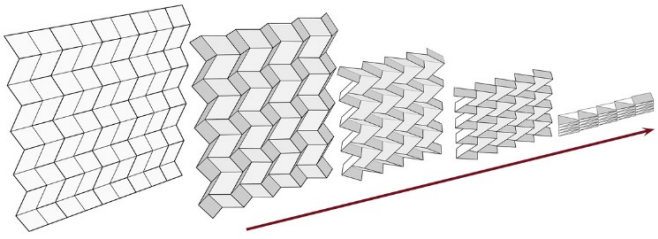

Figure 1.6: Miura-Ori Pattern

Starshade

Another application of origami techniques is the Starshade, a foldable screen designed by NASA to reduce the brightness of stars, used in combination with a space telescope to improve image quality. Given its large size (26 meters in diameter),

an origami-based mechanism was chosen because it can be folded smoothly and predictably.

The folding technique of the Starshade is similar to the *square-twist* method, where folds and twists transform a two-dimensional square sheet into a three-dimensional structure. In reality, the central part of the Starshade is circular rather than square, and the structure folds into a cylindrical shape, but the fundamental mechanism remains the same. When deployed, it takes the shape of a flower, with a circular central body surrounded by petal-like structures.

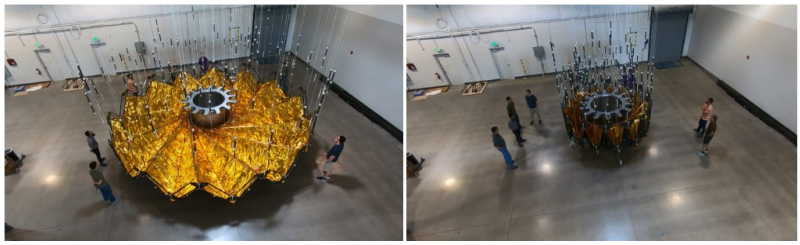

Figure 1.7: Starshade

Experimental collector debris

A final example presented here is an experimental prototype of a space debris collector [6].
The device is based on the conical origami model of Kresling.

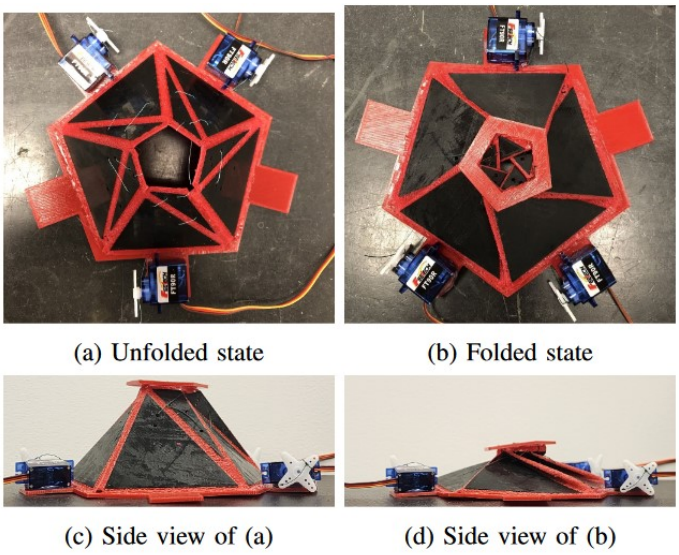

(a) Unfolded state (b) Folded state

(c) Side view of (a) (d) Side view of (b)

Figure 1.8: Deployed and compact configurations of the debris collector prototype

Chapter 2

Model and preliminary results

This chapter presents the model of the capture device under investigation, along with the preliminary results obtained previously, which served as the starting point for this thesis work.

2.1 Origami model

The device is composed of pentagonal and hexagonal plates and is specifically inspired by the Truncated Icosahedron, a Euclidean solid with 32 faces, including 20 hexagonal and 12 pentagonal ones. A debris capture mechanism of this type was presented in 2019 [8], and this thesis work draws inspiration from that project.
In the compact configuration, the plates are folded on top of each other and arranged in five levels. This design ensures deployment without interference 2.1.

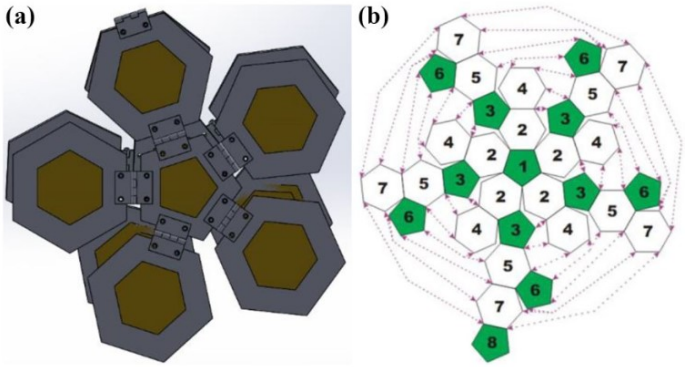

Figure 2.1: (a) Compact planar structure with five levels (b) Planar deployed structure [8]

The plates are connected to each other with hinge-type constraints. To transition from the compact to the deployed configuration, each plate rotates around its respective hinge by an angle of 180°.
As shown in Figure 2.2, once the structure is deployed, the capture mechanism consists of transitioning from the configuration shown in the first image to a shape similar to that of a soccer ball. To reach the capture configuration, the angle between a pentagon plate and an adjacent hexagon plate is 142.62°, and the angle between two regular hexagons is 138.19°.

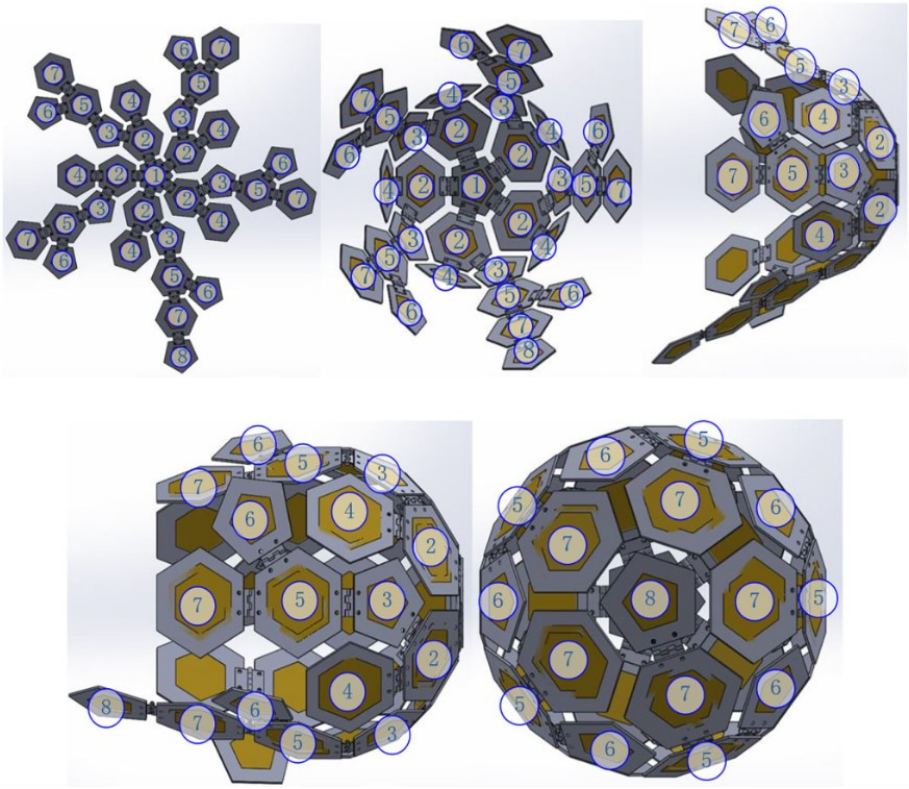

Figure 2.2: Capture mechanism [8]

Building upon the previously cited study, a preliminary investigation was conducted in the thesis work [7], wherein a structural model was developed and an initial kinematic analysis of the mission was performed. In this model, the plates have a side length of 0.2 m and a thickness of 0.01 m, and are made of carbon fiber composite with epoxy resin and Teflon, the latter being used alongside carbon to reduce friction between mechanical parts due to its self-lubricating properties.
The friction characteristics have been included in the definition of the hinges.

2.2 Preliminary analysis

The preliminary simulation conducted in the thesis [7] considered a chaser that pursues, captures, and decelerates a target. The target is assumed to have a cubic shape with a side length of 25 cm, characteristic of a CubeSat. It is positioned at a certain distance from the chaser and has an initial tangential velocity and rotational motion.
In contrast, the chaser is initially stationary. The simulation includes not only the opening of the origami structure but also the alignment, approach, and capture phases of the device, which ultimately captures the target.
Relative angular position and relative angular velocity between the chaser and the target were measured along all three spatial components, using the functions AX,AY,AZ for angular position, and WX,WY,WZ for angular velocity.
The AX function ($AX(i[,j])$) returns the rotational displacement (in radians) of marker i about the x-axis of marker j [13], `C++ Functions p.24`. Similarly for the AY and AZ functions.

The WX function ($WX(i[,j][,k])$) returns the x-component of the difference between the angular velocity vector of marker i in ground and the angular velocity vector of marker j in ground, and expressed in the coordinate system of marker k [13], `C++ Functions p.189`. Similarly for the WY and WZ functions.
To control the position (AX,AY,AZ) and the angular velocity (WX,WY,WZ) of the chaser relative to the target, the following relation was used:

$$T = -C_T \frac{d\theta}{dt} - K_T\theta + T_0 \tag{2.1}$$

where K_T is the torsional stiffness coefficient and C_T the viscous damping coefficient.
This is the torque function used by Adams when defining a *VTORQUE*.
The VTORQUE statement ($VTORQUE/id, I = id, JFLOAT = id, RM = id$) creates a rotational force element that applies a vector torque between two parts of the system, an action to the part to which the I marker belongs and a corresponding reaction to the part to which the JFLOAT marker belongs. The JFLOAT marker is a floating marker and it is on a different part than the I marker. Adams Solver moves the JFLOAT marker to keep it superimposed on the I marker. Since JFLOAT marker is on the ground part in this case, Adams Solver does not calculate reaction forces. The direction of the torque action is determined by the resultant vector formed by the three component torque you defined along the RM marker axes. The reaction is equal and opposite to the action [13], `C++ Statement p.431`.

Attitude control of the chaser was achieved using the VTORQUE function. Subsequently, forces were applied to simulate the alignment with the target and its tracking. This was achieved by defining three SFORCE statements, one for each spatial component.
The SFORCE statement applies a force or torque to two parts. You specify a marker on each part for force or torque application. In this case, three translational action-reaction forces ($SFORCE/id, I = id, J = id$) were defined. Adams applies a translational action and reaction force along the line connecting the I and the J markers [13], `C++ Statements, p.392`.
Under the assumption of uniform rectilinear motion and constant mass, the equations of dynamics can be derived:

$$F = Ma = \frac{\partial q}{\partial t} = M\frac{\partial V}{\partial t} \tag{2.2}$$

The chaser must approach the target with a nonzero relative velocity, which will decrease to zero when they reach a certain distance detected by a sensor.

In the alignment phase, the chaser transition from the compact to the deployed configuration was simulated, using kinematic motion laws with *STEP5* functions. The plates rotate by 180° around the hinges at a constant velocity.
It is now necessary to explain what the function *STEP5* does. This function provides an approximation to the step function with a quintic polynomial. It has continuous first and second derivatives. Its third derivative is discontinuous at $x = x_0$ and $x = x_1$. It has a syntax of the type:

$$STEP5(x, x_0, h_0, x_1, h_1)$$

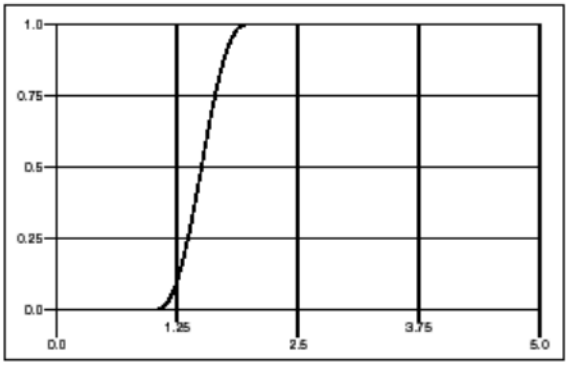

Figure 2.3: STEP5 function [13], `C++ Functions, p.139`

where x is the independent variable, x_0 and x_1 the values of x at the beginning and end of the function, h_0 and h_1 the initial and final values of the step. In this way, we obtain a *MOTION* that has a smooth and regular profile between the two extremes of the function [13], `C++ Functions, p.139`.

When the target is detected at a sufficiently close position, the chaser initiates the plate closure phase, generating inertia torques. This is followed by a deceleration phase, during which the target has been captured but remains free to move within the chaser. This inevitably leads to impacts due to contact between the target and the chaser's plates. These interactions are simulated using *contact forces* and *friction forces*, which will be analyzed in more detail later.

The first feasibility study carried out in the thesis work [7] brought results that will be used in the first part of this work.
In particular, the time histories of the torques acting on the hinges, obtained from the laws of motion, will be used for the preliminary dimensioning of the actuation system.
Below are frames from the simulation conducted in the thesis [7].

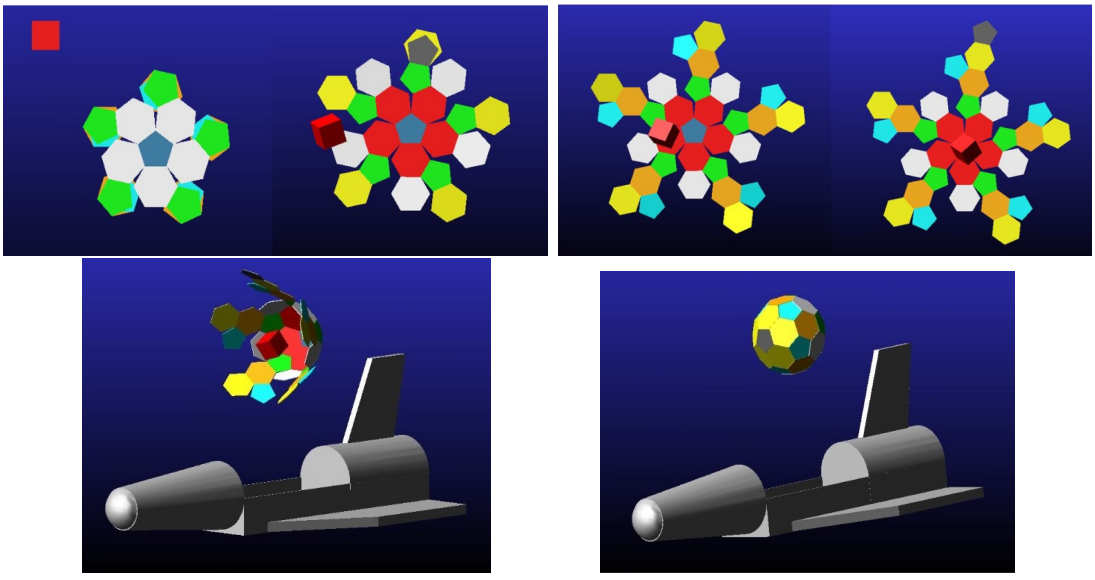

Figure 2.4: Simulation of the pursuit and capture phases [7]

2.2.1 Friction Force

To simulate friction in hinges, we choose to use the LuGre (Lund-Grenoble) formulation, a state variable dynamic friction model in which specific state variables are introduced to determine the level of friction.

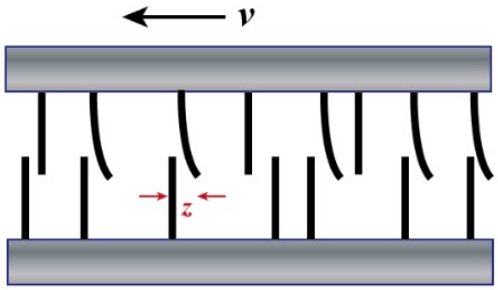

Figure 2.5: LuGre friction model [12]

The interface between the bodies is represented by bristles, and the friction can be considered as the forces produced by the bending of the bristles. In the case of *translational joint* 1D the friction is given by:

$$F = \sigma_0 z + \sigma_1 \dot{z} + \sigma_2 v \tag{2.3}$$

where σ_0 is the stiffness of the bristles, σ_1 the microscopic damping, σ_2 the viscous friction; $\dot{z}$ is the average speed of bristle deflection, different from v, which is the speed of the contact body.
To determine z in the LuGre formulation, an additional differential equation is used:

$$\dot{z} = v - \sigma_0 \frac{|v|}{F_{ss}(v)} z \tag{2.4}$$

where $F_{ss}(v) = F_d + (F_s - F_d)e^{-|\frac{v}{v_y}|^a}$
F_d and F_s represent respectively maximun dynamic and static friction.
Always for 1D case, the torque M is calculated as:

$$M = F \cdot R_p = (\sigma_0 z_\theta + \sigma_1 \dot{z}_\theta + \sigma_2 \omega) \cdot R_p^2 \tag{2.5}$$

where z_θ represents the angular displacement.
Thus, from 2.4 it results:

$$\dot{z} = \omega - \sigma_0 \frac{|\omega|}{M_{ss}(\omega)} z \cdot R_p^2 \tag{2.6}$$

where $M_{ss}(\omega) = M_d + (M_s - M_d)e^{-|\frac{\omega R_p}{v_s}|^\alpha}$ and represents the stationary LuGre model for a given ω, where $\dot{z}_\theta = 0$ (i.e. z_θ remains constant); the exponent α determines the decay rate, i.e., the shape of the Stribeck effect curve depicted in figure 2.6.

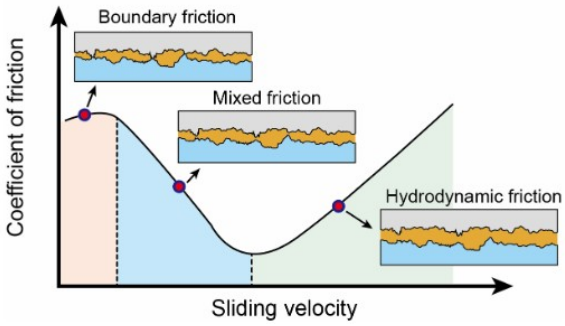

Figure 2.6: Stribeck effect, Trend of the friction coefficient as a function of slip velocity between two bodies [12], `Joints, p.146`

The LuGre model is used to describe non-linear loads and enables analytical studies where they are generally not feasible with discontinuous friction models. The following parameters for hinge friction were included in the model:

- $\mu_s = 0.25$: static friction
- $\mu_d = 0.2$: dynamic friction
- $v_s = 1 \cdot 10^{-4}\ m/s$: *stiction transition velocity*
- *Transition velocity coefficient* $= 1.5$: defines the transition from static and dynamic regime
- $\delta_{max} = 1 \cdot 10^{-5}\ m$: *max stiction deformation*, is the maximum deformation that occurs during the contact between the two bodies
- *Friction Arm* $= 1 \cdot 10^{-3}$: defines the friction torque of the hinge
- *Bending Reaction Arm* $= 1 \cdot 10^{-3}$: defines the moment of the reaction torque
- *Pin radius* $= 1 \cdot 10^{-3}\ m$: radius of the circumference around which the rotation occurs

2.2.2 Contact Force

Contact forces were used in the model to simulate the collisions between the target and the chaser plates during the capture phase. Specifically, the algortirm *IMPACT-Function Based Contact* available in MSC Adams was used. The software calculates the contact force as:

$$F_n = K \cdot g^e \tag{2.7}$$

where K is the stiffness and depends on the material used, g is the penetration of one geometry into the other, e is a positive value and indicates the force exponent.

Damping and frictional force can be added to this simple formulation of contact force. To do this Adams uses Coulomb friction model to compute the frictional forces [13], p.962. The coefficient of friction varies with the *slip velocity* as shown in figure 2.7; the *slip velocity* represents the difference in velocity between two surfaces in contact in the plane tangent to the point of contact.

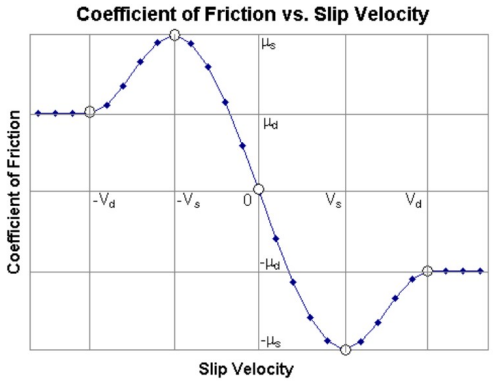

Figure 2.7: Friction model in the contact forces [12], `Contacts, p.233`

where V is the *slip velocity* in the contact point; v_s is the *stiction transition velocity*, the relative sliding velocity between two contacting surfaces below which the contact is considered static (hence with static friction) and above which the contact becomes dynamic (hence with dynamic friction); v_d is the *friction transition velocity*, the velocity at which the system gradually transitions from static to dynamic friction; μ_s and μ_d are the static and dynamic friction coefficients, respectively.

Considering the materials chosen, from the table in [12], `Contacts, p.234`, the following parameters are entered for the contact forces:

- $K = 3.5 \cdot 10^7$ N/m: *Stiffness*
- $C = 28 \cdot 10^3$ $N/(m\ s)$: *Damping*
- $d = 0.1$ mm: penetration depth; beyond this threshold, the software sets the damping coefficient to its maximum value as shown in figure 2.8
- $\mu_s = 0.25$: static friction coefficient
- $\mu_d = 0.2$: dynamic friction coefficient
- $v_s = 1 \cdot 10^{-4}$ m/s: *stiction transition velocity*
- $v_d = 1 \cdot 10^{-2}$ m/s: *friction transition velocity*
- $e = 1.5$: force exponent

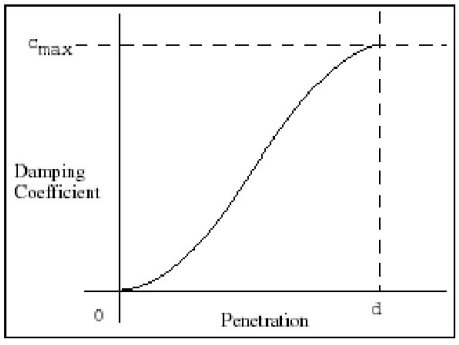

Figure 2.8: Trend of the damping coefficient as the penetration distance changes

2.3 Preliminary results

The feasibility study led to initial results that will be the starting point for the sizing of the actuation system.
It is important to note that the initial kinematic analysis of the present study differs from that conducted in [7]. This study does not focus on the impact phase following the target's capture by the chaser.
The torque results on the hinges constitute a fundamental basis for the actuators sizing developed in this study.

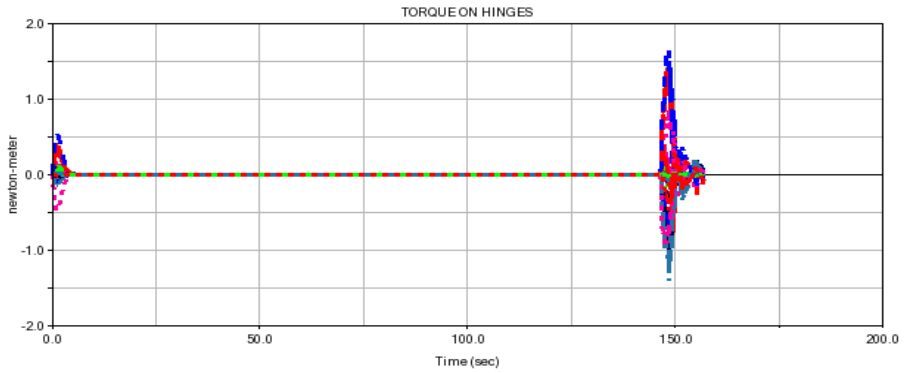

Figure 2.9: Torques acting on the hinges trends

In addition to these, the alignment forces of the chaser with the target and the pursuit are also considered, in the three directions, referred to as *SFORCE_x*, *SFORCE_y*, *SFORCE_z* in the model, as well as *VTORQUE* for attitude control.
These trends are shown in figure 2.10 2.11.
These forces also influence the relative distance and speed trends between chaser and target, shown in the figures 2.12 2.13.

The trends are not precisely linear, a phenomenon that is particularly evident in the alignment and tracking forces. This observation suggests the presence of discontinuities, which are also evident in the relative position and velocity trends between the chaser and the target. These abrupt trends are, at least in part, attributable to the formulation of the functions governing the forces.
Efforts will be made to improve this aspect, as described below.

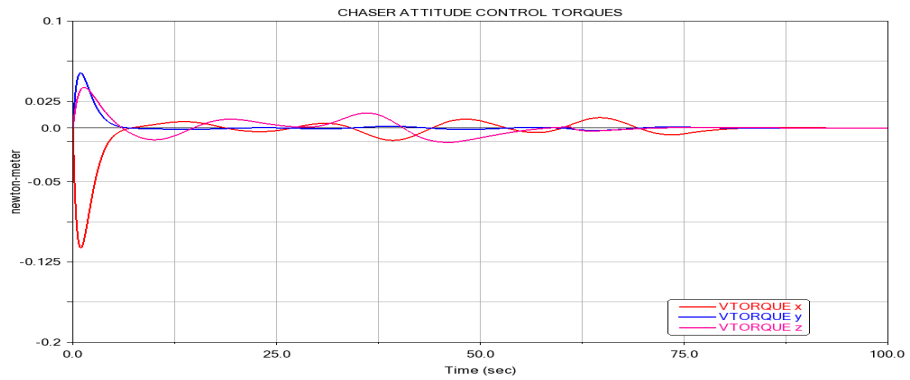

(a) Torque trend during alignment and deployment phases

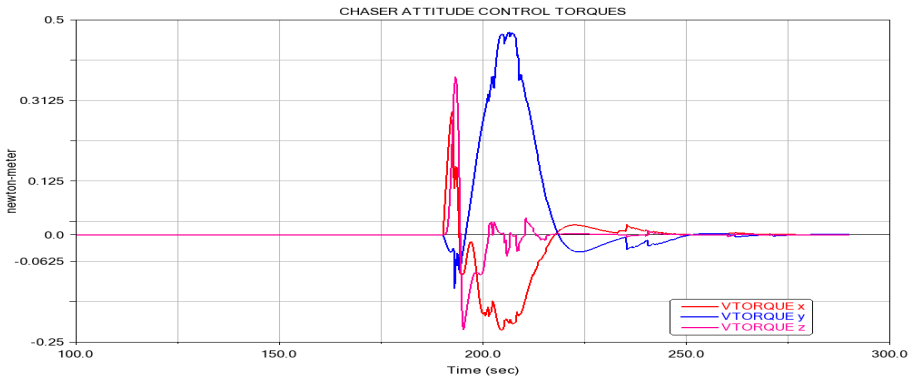

(b) Torque trend during capture phase

Figure 2.10: Torque trend for chaser attitude control

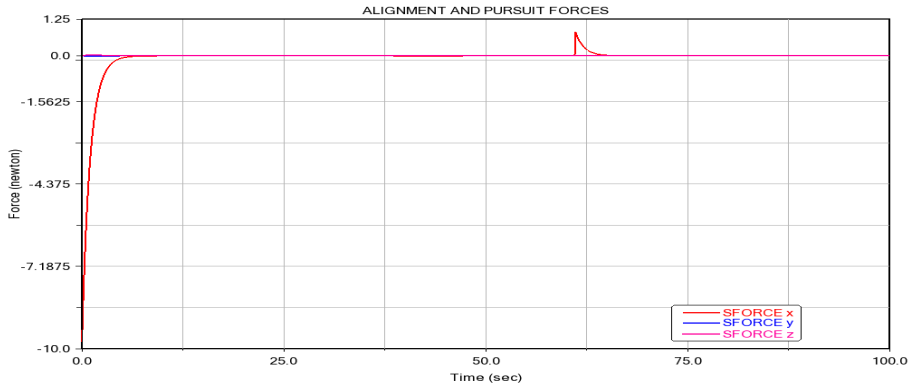

(a) SFORCEs trend during alignment and deployment phases

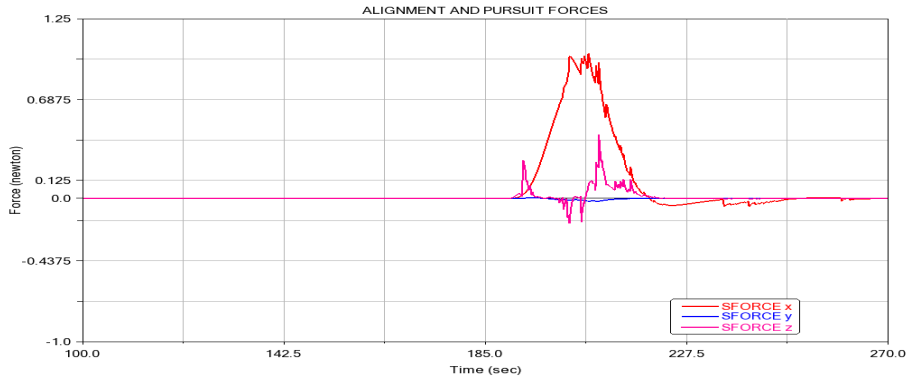

(b) SFORCEs trend during capture phase

Figure 2.11: Trend for alignment and pursuit forces

It is important to note that the deployment occurs at the beginning of the simulation, and the alignment and attitude control forces must counteract the simultaneous movement of the plates due to it.
This is an aspect that we will endeavor to enhance, as discussed subsequently.

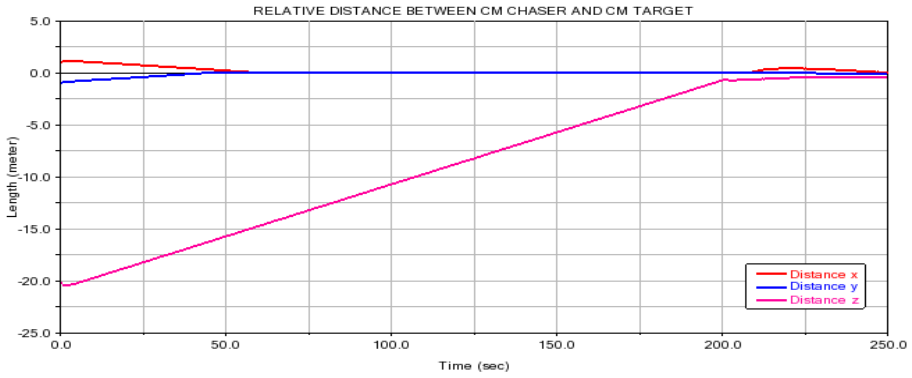

Figure 2.12: Relative distance between chaser and target

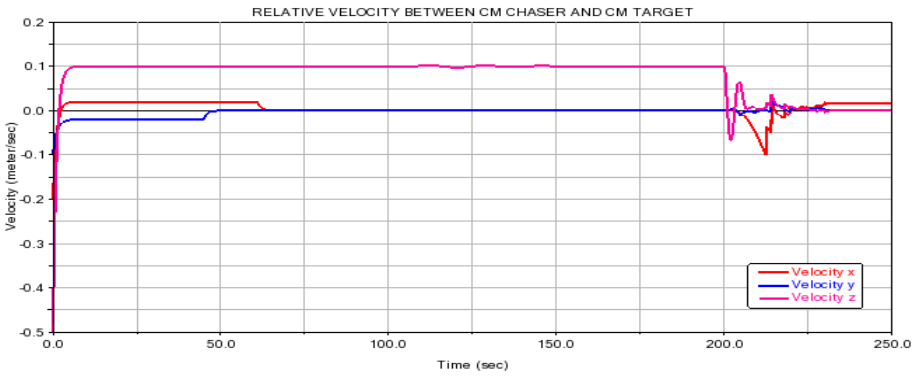

Figure 2.13: Relative velocity between chaser and target

2.4 Improvements for dynamic analysis

The preliminary analysis covered by this thesis [7] focused on a very first feasibility study of a possible realisation of the device. Hence, laws of motion were applied that are suitable for an initial kinematic analysis.
However, for the continuation of this study, modifications were necessary in order to design an actually applicable implementation system.
With the laws of motion we impose motions on the bodies which then result in torques on the joints and stresses on the plates. As shown in the previous figures, the torque trends exhibit discontinuities and unrealistic peaks that would compromise structural integrity. This needs to be softened by trying to obtain more realistic trends of the applied forces.

In particular, the alignment and tracking forces have been modified.
In the work [7], the force *SFORCE_x* is defined by the following function:

$$\begin{gathered} IF(SENVAL(SENSOR\_z) : 0, \\ -Mass \cdot (V_{x_{chaser}} - (V_{x_{target}} - IF(Distance_x : 0, 0, V_{lim}))), \\ STEP5(time, SENVAL(SENSOR\_z), 0, SENVAL(SENSOR\_z) + 40, -Mass \cdot V_{x_{ch}})) \end{gathered} \tag{2.8}$$

In 2.8, there are several elements that are very common in the Adams environment, which will be described in detail.
The first fundamental element is the IF function. This function has a syntax of the

type:

$$IF(expresion1:\ expression2,\ expression3,\ expression4)$$

This function evaluates the value of *expression*1; when this is negative it applies *expression*2, when it is null it applies *expression*3 and when it is positive it applies *expression*4.
The other important element is the *SENVAL* function. It returns the last scored value from the function expression or user-written subroutine associated with the *EVALUATE* argument on SENSOR/id [13], `C++ Functions, p.128`. In this case, the *SENVAL* function is used to detect the instant when *SENSOR_z* is triggered.
In this way, a force $F = M\ a$ is imposed, causing the chaser to approach the target with a relative velocity that is not zero, but equal to a V_{lim} that cancels when the chaser is at a certain distance from the target, measured by $SENSOR\_z$.
Such a force generates stress levels that could potentially lead to structural failure, since the IF function introduces discontinuities in the force trend and very high force peaks, which result in very high accelerations to which the plates are subjected.

Therefore, the force is corrected, defining it as follows:

$$\begin{aligned} &IF(SENVAL(SENSOR\_z):\ 0,\ STEP5(time,\ 0,\ 0,\ 10,\ (-Mass\cdot(V_{x_{chaser}}- \\ &(V_{x_{target}} - IF(Distanza\_x:\ STEP5(time,\ SENVAL(SENSOR),\ V_{x_{lim}}, \\ &SENVAL(SENSOR)+5,0),V_{x_{lim}},V_{x_{lim}}))))), \\ &STEP5(time,\ SENVAL(SENSOR\_z),\ 0,\ SENVAL(SENSOR\_z)+40, \\ &-Mass\cdot V_{x_{chaser}})) \end{aligned} \tag{2.9}$$

With this modification, we obtain a force that passes more smoothly and gradually from 0 to $F = M\ a$, thanks to the STEP5 function, eliminating the initial peak in the figure 2.11.
The discontinuity due to the fact that previously V_{lim} went from 0 to 0 as soon as the $SENSOR\_z$ was activated is also resolved by introducing a STEP5.

Similarly, the forces in the other two directions, *SFORCE_y* and *SFORCE_z*, are modified. The trends of the new forces are shown in figure 2.14.

With regard to *SFORCE_z*, an additional modification was implemented. Following a thorough examination of the relevant data, it was determined that the model should be augmented by the inclusion of an additional sensor, designated as *SENSOR_z_rel*. This sensor is activated when the distance between the centre of mass of the chaser and that of the target are at a distance of two meters or less. Consequently, the chaser initiates braking prior to commencing the capture phase, which is triggered by the activation of *SENSOR_z*, i.e., when the chaser is situated at a distance of 0.7 meters from the target. The integration of the new sensor has been demonstrated to enhance the braking performance of the chaser, thereby reducing its relative speed in relation to the target. This is due to the fact that, in contrast to an abrupt IF function, a STEP5 transition occurs from V_{lim_z} to 0 within a specified time interval.

A further improvement is made by introducing another sensor, named *SENSOR_avv* in the model. This sensor, like the *SENSOR_z*, measures the distance along the z-axis between chaser and target, but is activated when they are at a greater distance (10 meters in this study). When the chaser is at this distance from

the target, the deployment phase begins.
This makes the simulation much more realistic than the previous study, in which deployment took place at the start of the simulation, whatever the distance between the two. The introduction of this sensor is trivial in the Adams environment, but very useful if one considers that the device will be working in LEO orbit: deploying only when it is close enough to the target allows it to orbit most of the time in a compact configuration, thus with less surface area subjected to solar radiation and atmospheric friction, for example.
A review of the results of the study [7] reveals that torque levels acting upon the joints as well as the forces of alignment and tracking are elevated during the initial moments of the simulation. This phenomenon can be attributed to the deployment's occurrence at the beginning of the simulation, together with the alignment phase.

These changes are also reflected in the torque trends for attitude control. While these parameters remain constant, their trend has become more smooth. These are shown in Figure 2.15.

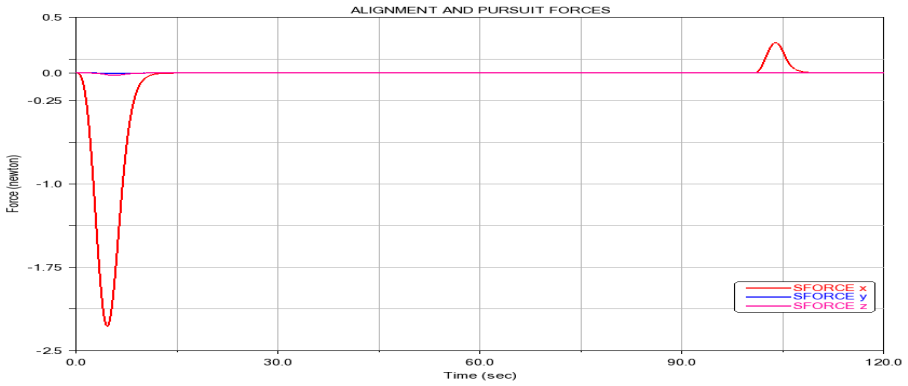

(a) Trend during pursuit phase

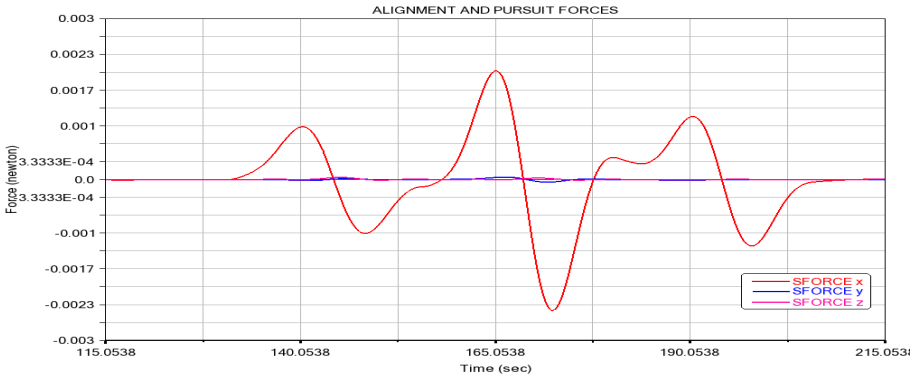

(b) Trend during deployment phase

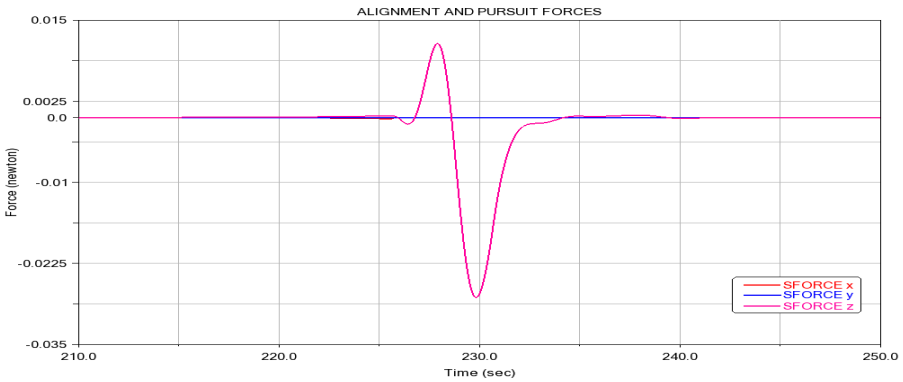

(c) Trend during capture phase

Figure 2.14: Alignment and tracking forces' profiles after improvements

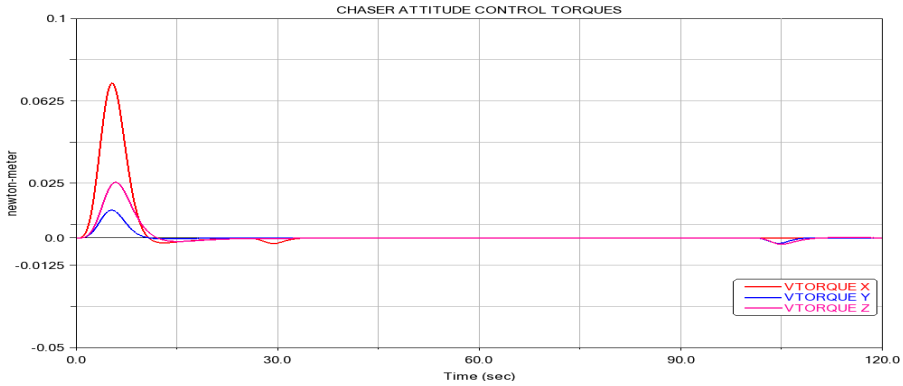

(a) Trend during alignment phase

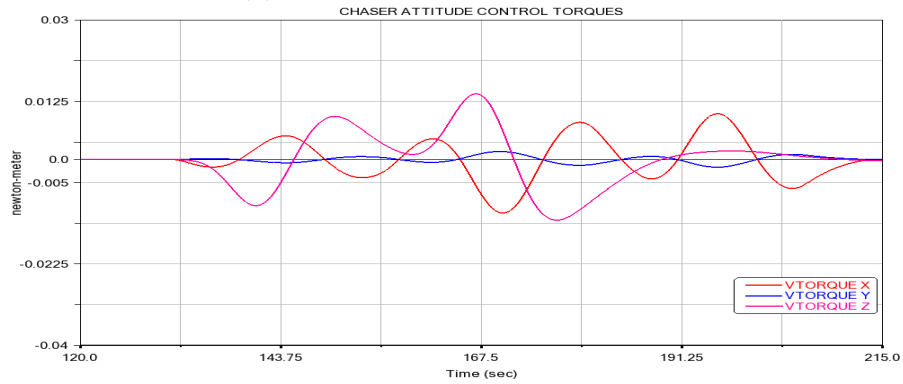

(b) Trend during deployment phase

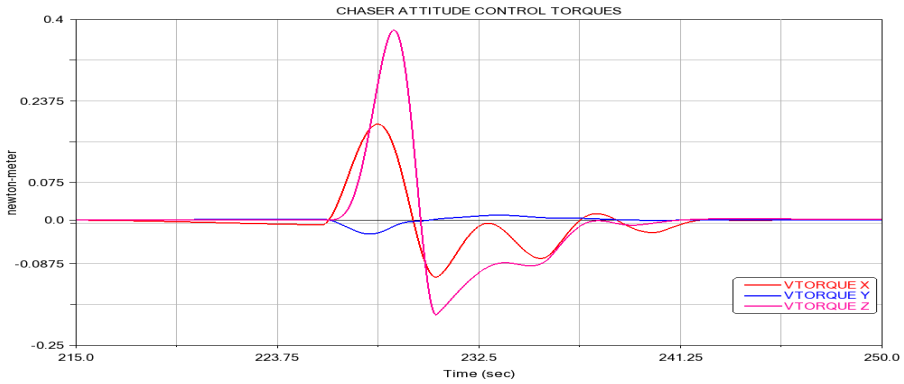

(c) Trend during capture phase

Figure 2.15: Attitude control torques' profiles after improvements

As previously noted, these forces also influence the relative position and velocity trends between chaser and target, as illustrated in the figures 2.16 2.17. It can be seen that the trends are now much smoother and without abrupt discontinuities.

These corrections also imply a softening of the torques' profiles, with peaks still present in the closing phase. However, compared to previous trends, there are no real discontinuities, as can be seen in figure 2.18, in which all torques acting on the joints are represented.

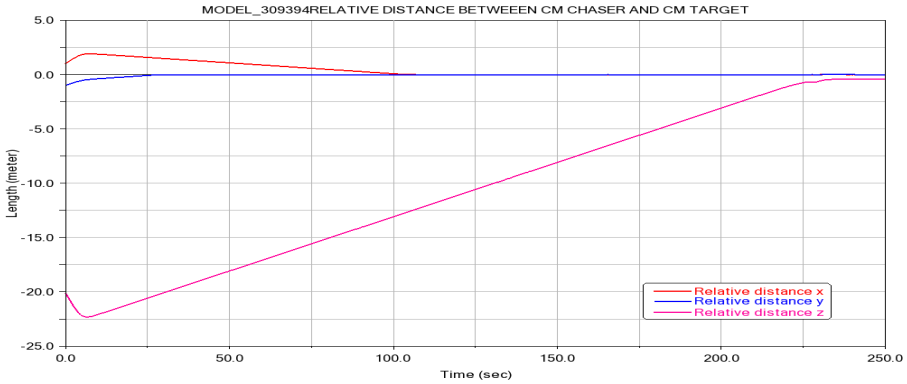

Figure 2.16: Relative distance between chaser and target after improvements

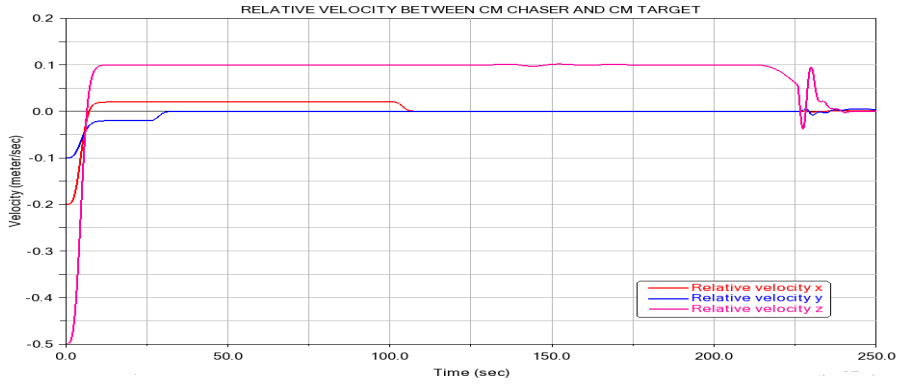

Figure 2.17: Relative velocity between chaser and target after improvements

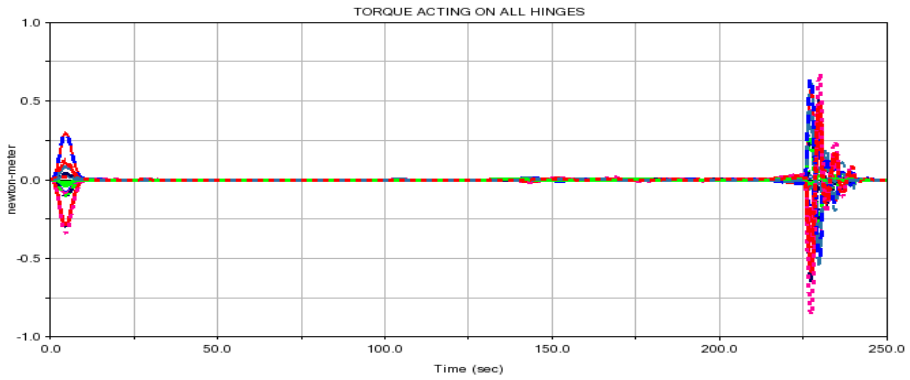

Figure 2.18: Trend of torques acting on joints after improvements

Another change was made, regarding the phase of closing the chaser and capturing the target. In the study [7] this takes place in 4 steps of 5 seconds each, so in 20 seconds in total. However, as illustrated in Figure 2.18, the torques exerted during the capture phase are notably higher than those in the deployment phase. Furthermore, the initial phase of movement in the capture phase encompasses all plates that do not rotate in the deployment phase. This process will be elaborated upon in greater detail in the paragraph 4.2.2.
Consequently, it was determined that the initial step would be subdivided into two stages, resulting in an overall phase comprising five steps of five seconds each, as opposed to the previous four-step sequence. This results in a slight increase in the time required to fully capture the target; however, it significantly enhances and simplifies the control of the movement of each plate. It also reduces the maxima and minima of the torques acting in this phase. Furthermore, the capture phase is executed in less than 30 seconds, which is less than half the time required for complete deployment. For these reasons, the decision to implement this change was deemed beneficial.

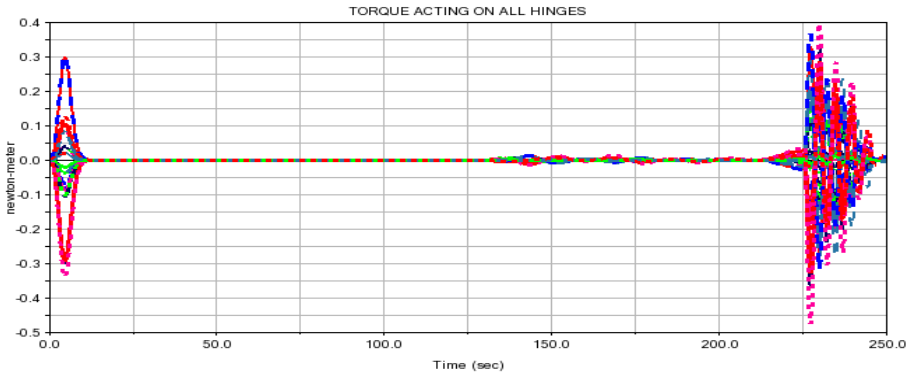

Figure 2.19: Trend of torques acting on hinges with capture in five steps

2.5 Preliminary Requirements

Upon arriving at this point, it was possible to proceed with the formulation of a preliminary set of requirements. This was possible thanks to a comprehensive understanding of the mission objectives and operations.

The formulation of these requirements was guided by the ECSS standards [20] and the recommendations provided in the *NASA Systems Engineering Handbook* [19].

This thesis focuses on a subset of elements relevant to the mission design. The proposed requirements primarily encompass the mechanical and structural components of a potential mission with this device as the payload.
To establish a comprehensive set of requirements, numerous additional aspects must be considered.
According to NASA guidelines, a good requirement must be:

- **Necessary** to the achievement of the mission objectives.
- **Unambiguous**, i.e. clearly written and interpretable only once.
- **Verifiable**, by testing, analysis, inspection or demonstration.
- **Realizable**, taking into account technological, economic and operational capabilities.

It is imperative that each requirement be subjected to **verification**, which entails confirming that the requirement meets the technical specifications. Furthermore, the requirement must undergo **validation**, the purpose of which is to ascertain that the final product meets the requirements.
During the system development process, a **Requirements Verification Matrix (RVM)** is compiled. This matrix is instrumental in maintaining a record of the requirements, their verification status, and the method used to verify each requirement. This matrix is a living document, which is updated as the project evolves. Some requirements are refined, while others are added or removed.

A well-defined requirement is characterized by several key elements. Firstly, it is imperative that a **unique identifier** be assigned to the requirement, ensuring its distinct categorization within the system. Secondly, a comprehensive and precise description of the requirement is essential, providing a clear understanding of its purpose and scope. Thirdly, the requirement should be structured within a hierarchical link, where it is positioned as the *parent* element and linked to its subordinate *child* element. Finally, the intended method of verification must be clearly specified, providing a clear framework for validation and validation outcomes. The hierarchical structure facilitates traceability throughout the development cycle, providing a clear understanding of how high-level requirements are translated into detailed technical specifications.

In this work, the following prefixes were used for the requirements:

- **MECH**: mechanical requirements;
- **STR**: structural requirements;
- **MIS**: mission-related and operative requirements;
- **PHY**: physical requirements.

Each requirement is coded according to the convention `R-ABCD-000`, where `R` denotes that the requirement is part of the set of requirements, `ABCD` indicates the category of the requirement, and `000` designates the sequential number assigned to

each requirement.
The table 2.1 presents a list of the preliminary requirements that have been identified for the system.

Req. ID	**Text**
R-MECH-010	The device shall complete full deployment within 75 seconds from the reception of the command
R-MECH-020	The deployment of the device shall occur without abrupt discontinuities in velocity, ensuring a smooth and continuous motion profile
R-MECH-030	The device shall close smoothly, without any sudden or abrupt movements, and shall complete the capture process within 30 seconds
R-MECH-040	The device shall operate automatically
R-MIS-010	The device shall be capable of capturing debris with dimensions up to $25 \times 25 \times 25$ cm^3 (equivalent to 15.6 dm^3) in LEO
R-MIS-020	The device shall not generate debris during the mission
R-STR-010	The device shall have a volume less than or equal to 35 dm^3 in its compact configuration at launch
R-STR-020	The materials used in the structural components shall not exhibit delaminations under operational and environmental loads
R-STR-030	The device shall be designed to endure the typical radiation environment encountered in Low Earth Orbit (LEO)
R-PHY-010	The device shall have a mass that is less than 20 kg

Table 2.1: List of preliminary requirements

Chapter 3

Flexible bodies

The first part of this study will focus on introducing body flexibility in multibody analysis. Flexible bodies allow for the modeling of deformations and structural vibrations, providing greater accuracy compared to rigid bodies.

3.1 Dynamic Substructuring

To achieve this, it is useful to introduce reduction methods, particularly *dynamic substructuring* techniques such as *Component Mode Synthesis* (CMS).
CMS is particularly beneficial when analyzing systems composed of numerous bodies or complex structures. It enables the division of a complex structure into substructures (*superelements*), which are then coupled through interface degrees of freedom (DOFs), thereby reducing the computational burden.
Originally developed to reduce the cost of modal analysis in complex dynamic systems, CMS is now widely adopted in finite element analysis (FEA).

One of the most commonly used CMS techniques is the Craig-Bampton method, which is implemented in commercial tools such as MSC Nastran, as will be discussed later. This method is well established in flexible multibody analysis. However, the Craig-Bampton formulation typically uses fixed-interface normal modes, which may not fully capture the dynamic behavior needed for some engineering applications.
The method can be enhanced by incorporating boundary conditions into the original Craig-Bampton matrix, redefining the mass and stiffness matrices before constructing the final reduced model. This approach allows for the inclusion of additional, non-fixed-interface modes.

3.1.1 Equation of motion of a flexible multibody system

The equation of motion of a flexible multibody system can be derived using the principle of virtual work to describe the relationship between the rigid body nodes and the flexible body nodes.
The system's generalized coordinates are partitioned into *reference coordinates* and *elastic coordinates*. The equation of motion can then be written as:

$$\begin{bmatrix} M_{rr} & M_{rf} \\ M_{fr} & M_{ff} \end{bmatrix} \begin{bmatrix} \ddot{q}_r \\ \ddot{q}_f \end{bmatrix} + \begin{bmatrix} 0 & 0 \\ 0 & K_{ff} \end{bmatrix} \begin{bmatrix} q_r \\ q_f \end{bmatrix} = \begin{bmatrix} (Q_e)_r + (Q_v)_r \\ (Q_e)_f + (Q_v)_f \end{bmatrix} \tag{3.1}$$

where M_{rr} is the mass matrix which corresponds to the rigid motion, $M_{rf} = M_{fr}^T$ is the mass matrix which represents the coupling between rigid motion and elastic deformation, M_{ff} is the mass matrix of a flexible body, q_r is the vector of rigid modes, q_f is the vector of elastic modes, K_{ff} the stiffness matrix of flexible body, Q_e the vector of generalized forces, Q_v the quadratic velocity term, which includes the centrifugal and Coriolis forces.

Since the analysis requires computing the displacement of a vast number of finite elements, the computational cost is very high. CMS is specifically used to reduce the elastic modes in the equation of motion, thereby decreasing the computational cost.
Based on equation 3.1, the equation describing the natural vibrations of the flexible body in the reference system of the rigid body can be written as:

$$\mathbf{M}_{ff}\ddot{\mathbf{q}}_f + \mathbf{K}_{ff}\mathbf{q}_f = 0 \tag{3.2}$$

where $\mathbf{M}_{ff}$ is the flexible body's mass matrix.
The eigenvalue problem of this equation can be defined as:

$$\left[\mathbf{K}_{ff} - \omega_j^2 \mathbf{M}_{ff}\right] \mathbf{A}_j = \mathbf{0} \qquad (j = 1, 2, ..., m) \tag{3.3}$$

from which the m natural frequencies and the m mode shapes can be calculated.
High-frequency modes, which have a negligible effect on nodal displacements, are truncated, leaving only the low-frequency modes. This reduces the system's degrees of freedom.
The remaining low-frequency modes form the modal transformation matrix and can be expressed as:

$$\mathbf{\Phi} = \begin{bmatrix} \mathbf{A}_1 & \mathbf{A}_2 & ... & \mathbf{A}_j \end{bmatrix} \tag{3.4}$$

The elastic modes $\mathbf{q}_f$ can be transformed into the modal coordinates $\mathbf{p}$ thanks to the modal transformation matrix:

$$\mathbf{q}_f = \mathbf{\Phi}\mathbf{p} \tag{3.5}$$

It can then be written:

$$\begin{bmatrix} \mathbf{M}_{rr} & \bar{\mathbf{M}}_{rf} \\ \bar{\mathbf{M}}_{fr} & \bar{\mathbf{M}}_{ff} \end{bmatrix} \begin{bmatrix} \ddot{\mathbf{q}}_r \\ \ddot{\mathbf{p}} \end{bmatrix} + \begin{bmatrix} \mathbf{0} & \mathbf{0} \\ \mathbf{0} & \bar{\mathbf{K}}_{ff} \end{bmatrix} \begin{bmatrix} \mathbf{q}_r \\ \mathbf{p} \end{bmatrix} = \begin{bmatrix} (\mathbf{Q}_e)_r + (\mathbf{Q}_v)_r \\ \left(\bar{\mathbf{Q}}_e\right)_f + (\bar{\mathbf{Q}}_v)_r \end{bmatrix} \tag{3.6}$$

where $\bar{\mathbf{A}} = A\Phi$

This describes how to transform the elastic modes in the equation of motion into modal coordinates using the transformation matrix. The dynamic response of the flexible body is approximated by a few low-frequency modes, greatly reducing the computational cost. This is the *normal mode* approach.

Craig-Bampton modal transformation matrix

Craig-Bampton modal transformation matrix with orthogonal modes can be obtained by solving the eigenvalues problem two times. The first time, the eigenvalue

is obtained for the normal modes of the original matrix; the second time, for the orthogonal modes of the Craig-Bampton matrix.
Therefore, the Craig-Bampton matrix with orthogonal modes can be used to decouple the equation of motion of the system, which is the generalized form used in most commercial software.
In Craig-Bampton's method, one then divides the elastic coordinates $\mathbf{q}_f$ in 3.2 into interface nodes $(\mathbf{q}_f)_b$ and internal nodes $(\mathbf{q}_f)_i$:

$$\mathbf{q}_f = \begin{bmatrix} (\mathbf{q}_f)_b^T & (\mathbf{q}_f)_i^T \end{bmatrix}^T \tag{3.7}$$

And so:

$$\begin{bmatrix} (\mathbf{M}_{ff})_{bb} & (\mathbf{M}_{ff})_{bi} \\ (\mathbf{M}_{ff})_{ib} & (\mathbf{M}_{ff})_{ii} \end{bmatrix} \begin{bmatrix} (\ddot{\mathbf{q}}_f)_b \\ (\ddot{\mathbf{q}}_f)_i \end{bmatrix} + \begin{bmatrix} (\mathbf{K}_{ff})_{bb} & (\mathbf{K}_{ff})_{bi} \\ (\mathbf{K}_{ff})_{ib} & (\mathbf{K}_{ff})_{ii} \end{bmatrix} \begin{bmatrix} (\mathbf{q}_f)_b \\ (\mathbf{q}_f)_i \end{bmatrix} = \mathbf{0} \tag{3.8}$$

The static modes are calculated by imposing zero inertial forces and considering the forces at internal nodes to be zero; this is called static correction:

$$(\mathbf{K}_{ff})_{ib} (\mathbf{q}_f)_b + (\mathbf{K}_{ff})_{ii} (\mathbf{q}_f)_i = \mathbf{0} \tag{3.9}$$

The internal nodes can be expressed using the interface nodes and the stiffness matrix $(\mathbf{K}_{ff})_{ii}$ (if it is not singular):

$$(\mathbf{q}_f)_i = -(\mathbf{K}_{ff})_{ii}^{-1} (\mathbf{K}_{ff})_{ib} (\mathbf{q}_f)_b = \mathbf{\Phi}_C (\mathbf{q}_f)_b \tag{3.10}$$

As for nodes constrained at the interface, they are obtained from a modal analysis by assigning each constrained degree of freedom a unit displacement, keeping all others fixed:

$$(\mathbf{M}_{ff})_{ii} (\ddot{\mathbf{q}}_f)_i + (\mathbf{K}_{ff})_{ii} (\mathbf{q}_f)_i = \mathbf{0} \tag{3.11}$$

Calling $\mathbf{A}_k^I$ the *k-th* modal shape, *l* the number of modes, *I* the first eigenvalue, the modes of the constrained interface nodes can be expressed as:

$$\mathbf{\Phi}_f = \begin{bmatrix} \mathbf{A}_1^I & \mathbf{A}_2^I & ... & \mathbf{A}_k^I \end{bmatrix} \tag{3.12}$$

After doing the static correction and obtaining the nodes constrained to the interface, the Craig-Bampton matrix can be assembled as:

$$\mathbf{\Phi}_{CB} = \begin{bmatrix} \mathbf{I} & \mathbf{0} \\ \mathbf{\Phi}_C & \mathbf{\Phi}_f \end{bmatrix} \tag{3.13}$$

The physical elastic coordinates of the flexible body can be written in terms of modal coordinates:

$$\mathbf{q}_f = \mathbf{\Phi}_{CB} \mathbf{p}_I \tag{3.14}$$

where $\mathbf{p}_I$ are the modal coordinates corresponding to the original Craig-Bampton matrix.

Thus, free-free modes are derived with the Craig-Bampton method, but these do not always lead to the exact solution. Therefore, one can improve the method by imposing the reference conditions directly on the identity matrix of the original Craig-Bampton matrix or on the shape functions to calculate the new mass and stiffness matrices and derive the enhanced Craig-Bampton matrix.
The quality of the reduced solution with modal truncation depends on the number of modes used.

3.1.2 CMS in MSC Nastran

The separation of elastic DOF into internal and interface components corresponds directly to how MSC Nastran manages the reduction process through dedicated sets:

- **ASET**: analysis set – interface DOFs retained after reduction [15], `p.1227`;
- **QSET**: modal coordinates preserved after reduction [15], `p.2942`;
- **CSET**: DOFs held fixed during modal analysis [15], `p.1645`;

The internal DOFs $(\mathbf{q}_f)_i$ are typically excluded from the reduction output and not included in the **ASET**, while the interface DOFs $(\mathbf{q}_f)_b$ correspond to the **ASET**, which is retained in the reduced model and serves as the connection between substructures.
During fixed-interface modal analysis, the boundary/interface DOFs are constrained using the **CSET**, while the internal DOFs are free to vibrate. The resulting mode shapes from this step (fixed-interface normal modes) populate the **QSET**, which stores the modal DOFs retained after truncation.
The modal basis $\mathbf{\Phi}_{CB}$ discussed previously is explicitly constructed in Nastran using the combination of:

- **Static constraint modes**: obtained by imposing unit displacements on ASET DOFs and computing internal response.
- **Fixed-interface normal modes**: obtained from modal analysis with CSET. The reduced coordinates are stored in QSET.

3.2 Modal Neutral File

To introduce the flexible bodies in MSC Adams is necessary creating a *Modal Neutral File (MNF)* to define the modal properties of the body. This file is generated by a FEM analysis, and in this case MSC Nastran will be used. The MNF is a binary file that contains informations about geometry (location of nodes and node connectivity), nodal mass and inertia, mode shapes, and generalized mass and stiffness corresponding to each mode shape [14], `p.3`.

To do this, the 2D geometry of the bodies was reproduced in Patran, where a mesh was created. The orthotropic material properties (carbon fiber) were then defined, and the composite laminate was created. A parametric analysis was performed by varying the number and orientation of the layers. Composite materials will be discussed later; here, we continue with the analysis setup.
Having defined the material, a 2D shell-type property was created and assigned to the finite elements.

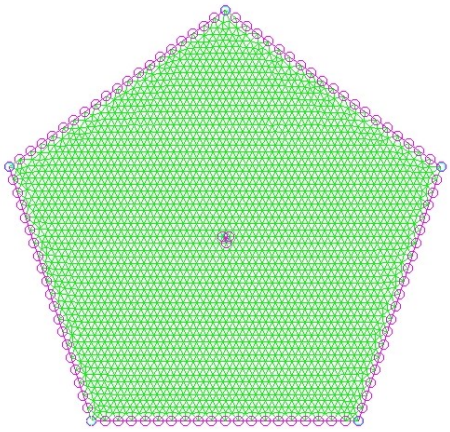

Figure 3.1: Finite element model of the pentagonal plate

As for the interface nodes, since it is a single body within a multibody system, it is necessary to determine which rigid body it will replace. An example is provided below for the central pentagon.

The central pentagon is connected with five hinges to five hexagons, meaning it is constrained on all sides. Therefore, five Multipoint Constraints (MPCs) of type RBE2 are created at each side. The master node is placed at the midpoint, while the slave nodes include all other nodes on that side, excluding one. This exclusion is necessary to prevent any node from being included in two different MPCs, which is not allowed.
In addition, control forces F_x, F_y, F_z are applied to the central pentagon in the model (because it is the barycenter of the model); this must also be reflected in the finite element model. The forces are applied to the barycenter, so a node is created at the barycenter of the pentagon, which will be the *master* node of another MPC; the *slave* nodes are those from the element closest to the barycenter.
A DOF list was then created, containing the five independent nodes positioned at the midpoints of the sides and the one located at the barycenter (Figure 3.2a). These represent the constraints of *Revolute Joints* present in the Adams model, the interface nodes of the dynamic substructuring.

We then move on to the analysis setup. A modal analysis (SOL 103) must be performed to generate the input file for Adams.
The previously defined DOF list is entered in the *Select ASET/QSET* section, and the necessary input parameters are specified in *ADAMS Preparation*.

In *ADAMS Output* section you are asked to run the analysis and generate the desired MNF file. After selecting the correct units, the number of required modes is specified. The software automatically indicates the necessary *Output Requests*, which must be included in the *Subcases* tab, together with the number of modes (figure 3.2b).
MSC Nastran uses the Craig-Bampton modal reduction method to generate two distinct sets of modes. The first consists of the fixed-interface normal modes, computed by constraining the interface degrees of freedom. The second includes the constraint (residual) modes, obtained by imposing unit displacements at the

interface nodes to simulate static deformation behavior.
After orthogonalizing the basis, these modes are transformed into a reduced set that includes six rigid motion modes (zero-frequency, disabled in Adams) and a number of flexible free-free modes, ordered by increasing frequency.
The total number of modes depends on the number of requested dynamic modes in the output and on the static modes. The latter is influenced by the number of the interface nodes and the degrees of freedom (DOFs) of each interface node. For instance, the central pentagon, which has six interface nodes, will result in a greater number of total modes than the hexagon, which has only three interface nodes.
At this point the analysis can be run.

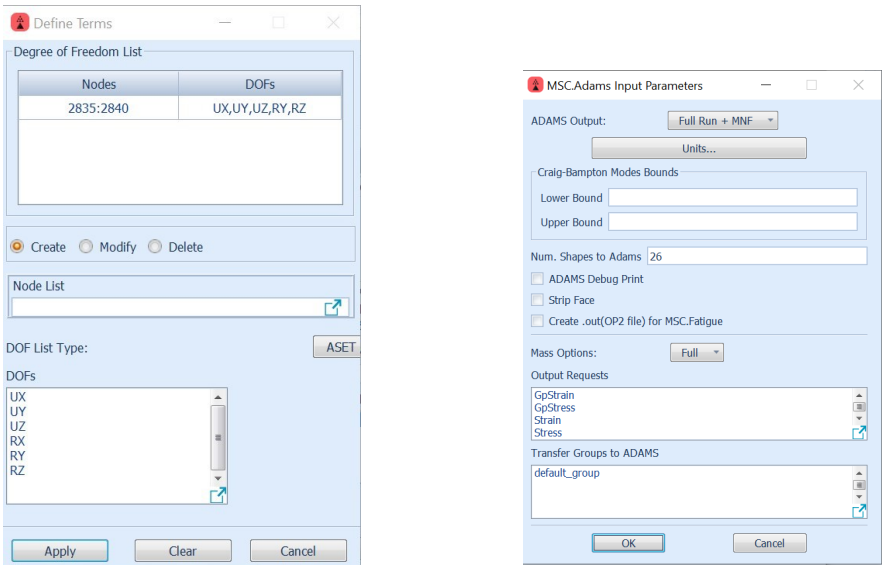

(a) DOF list (b) Adams Preparation

Figure 3.2: Analysis setup

This process produces, in addition to the modal analysis results, the input file to be imported into Adams. In the multibody model, the corresponding rigid body is selected and replaced by the flexible body by importing the created MNF file.
Since the plates are all geometrically identical, only two finite element models were created, one for the pentagonal plate and one for the hexagonal plate. Obviously, the boundary conditions vary depending on the hinge connections for each specific case.

3.2.1 Composite materials

Composite materials are combinations of two or more constituents with distinct physical and chemical properties, engineered to achieve superior performance compared to the individual components. They offer broad versatility in engineering applications due to the ability to control various parameters, such as fiber orientation, ply thickness, and matrix type. These variables allow for the precise and targeted optimization of mechanical properties such as strength, stiffness, and fatigue resistance. The main advantage of composites lies in their ability to deliver enhanced mechanical performance with reduced weight, making them widely adopted in the aerospace sector.

In this study, a Carbon Fiber Reinforced Polymer (CFRP) is used, characterized by the following properties [18]:

- $E_{11} = 181.0$ GPa Longitudinal Young's Modulus
- $E_{22} = 10.3$ GPa Transverse Young's Modulus
- $\nu_{12} = 0.29$ Poisson's Ratio
- $G_{12} = G_{13} = 7.1$ GPa In-plane Shear Modulus
- $G_{23} = 5.0$ GPa Out-of-plane Shear Modulus
- $\rho = 1600$ kg/m^3 Density

The freedom to be able to change certain material parameters is one of the reasons why the use of composites in aerospace engineering is so extensive [16]. However, this flexibility is limited because traditional analysis methods for metals cannot always be applied to composites. Therefore, there is often a tendency to obtain a composite material that behaves like a better-known material (e.g. aluminum alloy), but with a higher strength-to-weight ratio.

As commonly done in engineering practice, symmetric laminations are used to simplify the analysis of composite materials. This approach decouples in-plane and out-of-plane deformations, preventing unexpected and undesired structural behavior. As a result, the composite exhibits a quasi-isotropic response, which is significantly easier to analyze.
Another critical issue to consider when using composite materials is the free edge effect, which refers to stress concentrations that arise at the edges of the laminate due to mismatched deformations between plies with different fiber orientations. These strain gradients can lead to interlaminar stresses and potential delamination, ultimately compromising the structural integrity. To mitigate this phenomenon, symmetric and balanced layups are often adopted, typically with a maximum fiber angle difference of 45° between adjacent plies. This approach helps minimize discontinuities and reduces edge-induced stresses. Naturally, an in-depth study would be required for the optimal selection of material and stacking sequence, but in this work, the current state-of-the-art aerospace practices will be adopted.
A symmetric laminate configuration with ply orientations of $90/45/0/-45$ is used for the structural analysis.

As previously mentioned, the main advantage of composite materials lies in achieving mechanical properties equal to or superior to those of metallic materials, while significantly reducing weight. This is made possible by the specific geometry of the fibers themselves, which typically have a diameter of a few micrometers [17]. Accordingly, a ply thickness of 0.125 mm is selected.

This can be translated into further design requirements, concerning precisely the composite material chosen for the realization of the plates.
As previously, the identifier codes were composed in accordance with the `R-ABCD-000` criterion, employing the prefix `MAT`, which denotes `material`.

Req. ID	Text	Parents
R-MAT-010	The plates shall be manufactured using Carbon Fiber Reinforced Polymer (CFRP)	R-STR-030
R-MAT-020	The plates shall be manufactured with a thickness of 0.125 mm	R-PHY-010
R-MAT-030	The laminate shall exhibit quasi-isotropic behavior	R-MAT-040 (child) R-STR-020 (father)
R-MAT-040	The laminates shall have a symmetric and balanced stacking sequence	R-MAT-030

Table 3.1: List of Material Requirements

3.2.2 Effects of lamination

The structural behavior of the plates was analyzed as a function of the composite material properties. In particular, variations in the number of plies and their orientations were investigated.
In summary, plies with a thickness of 0.125 mm were used `[R-MAT-020]`, arranged in the stacking sequence $90/45/0/-45$ `[R-MAT-040]`. Four configurations with 8, 16, 24, and 32 plies were examined, all arranged in a symmetric stacking sequence `[R-MAT-030]`. This results in plate thicknesses ranging from 1 mm (8 plies) to 4 mm (32 plies), which are typical values for this type of structure in aerospace applications.
As expected, changes in these parameters lead to variations in the natural frequencies of the plates, thus affecting the dynamic behavior in the multibody model. The aim of this analysis is to optimize the dynamic response of the plates within the multibody system; the resulting eigenfrequencies are summarized in Table 3.2. For simplicity of visualization, only the first 10 natural frequencies are reported, excluding the first 6 corresponding to rigid motion as computed by Nastran.

An increase in natural frequencies with the number of plies is clearly observed. Given the preliminary nature of this study, the design will adopt CFRP plates with 32 plies, as this configuration provides the highest natural frequencies among those analyzed. In the future, if subsequent analyses confirm that very high frequencies can be excluded from the operating frequency range of the device, it may be possible to consider a laminate with fewer plies, allowing for further weight savings.
It should also be noted that the examples presented here refer to the central pentagonal plate, which is much more constrained than the others, and to the hexagonal plate with the highest number of connections in the Multibody model. Consequently, the natural frequencies obtained for these plates are higher than those of, for example, the outer pentagonal plate in the complete model.

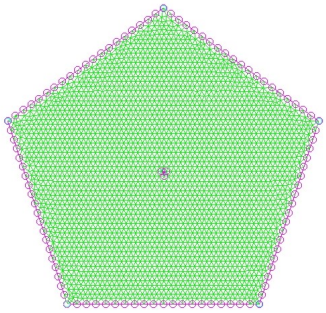

(a) Pentagonal plate

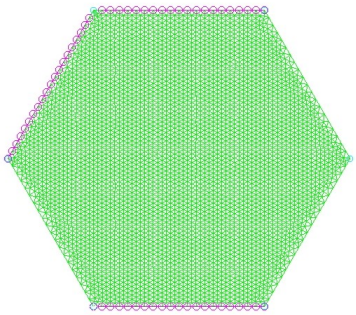

(b) Exagonal plate

Figure 3.3: (a) Finite elements model of the pentagonal plate (b) and exagonal plate

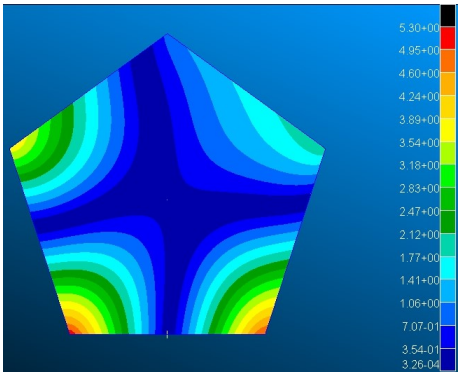

(a) Pentagonal plate - Mode 7

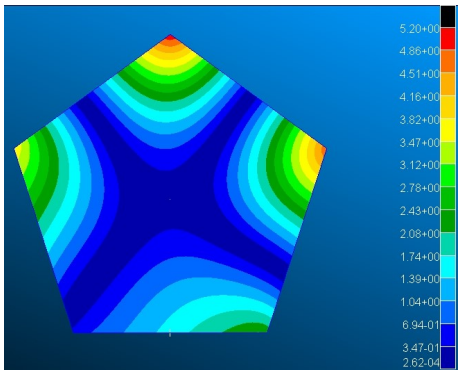

(b) Pentagonal plate - Mode 8

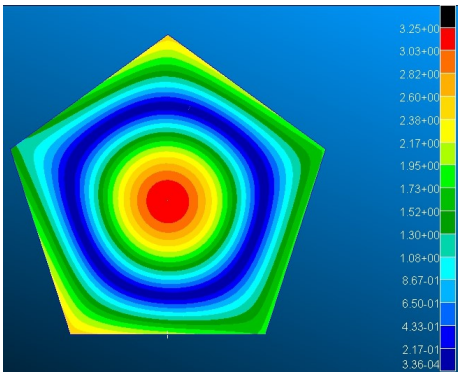

(c) Pentagonal plate - Mode 9

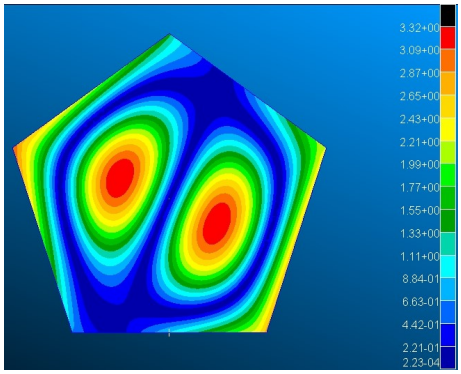

(d) Pentagonal plate - Mode 10

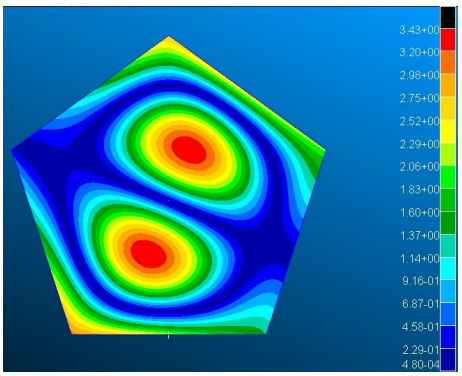

(e) Pentagonal plate - Mode 11

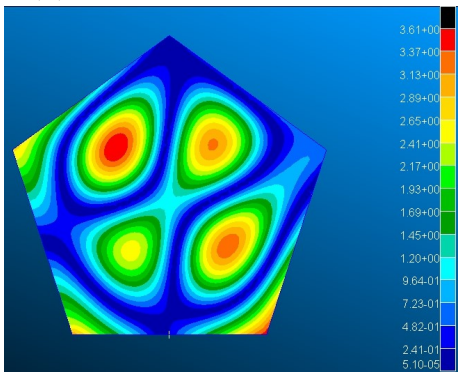

(f) Pentagonal plate - Mode 12

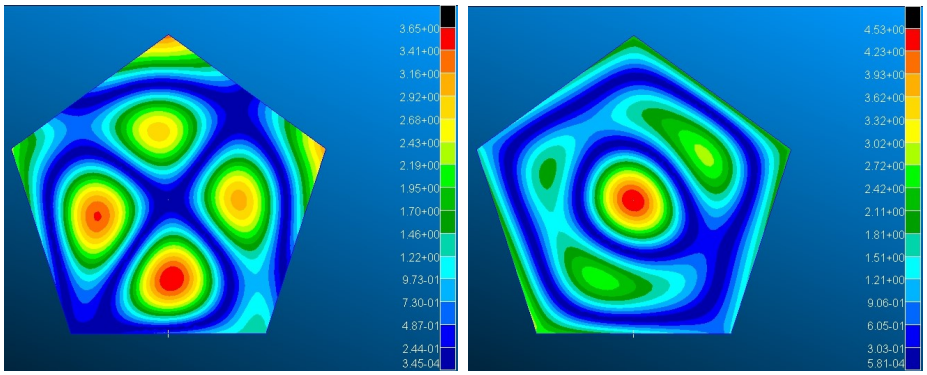

(g) Pentagonal plate - Mode 13 (h) Pentagonal plate - Mode 14

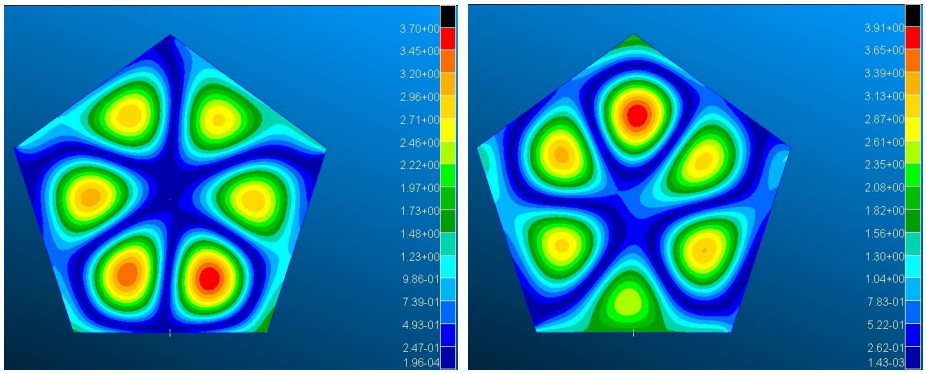

(i) Pentagonal plate - Mode 15 (j) Pentagonal plate - Mode 16

Figure 3.4: First ten elastic modal shape of the pentagonal plate

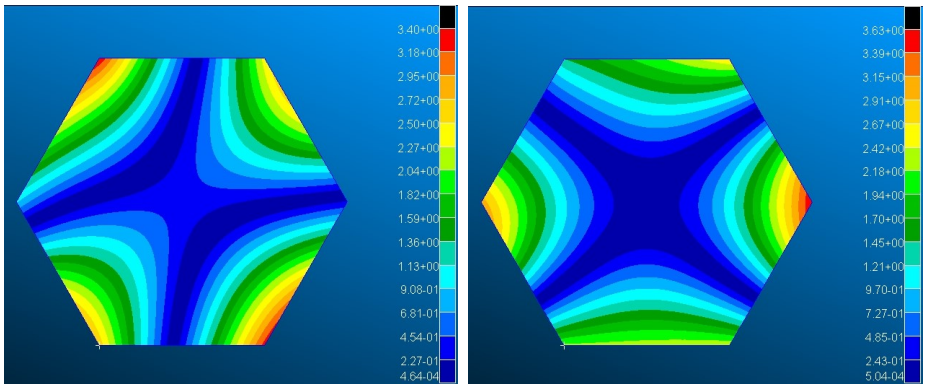

(a) Exagonal plate - Mode 7 (b) Exagonal plate - Mode 8

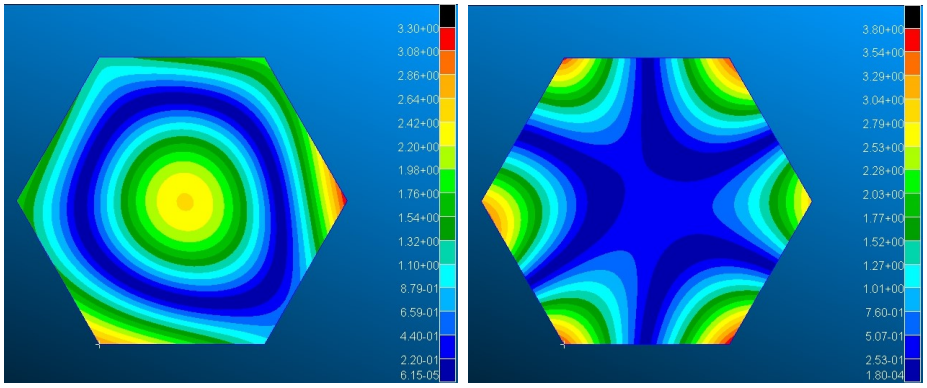

(c) Exagonal plate - Mode 9 (d) Exagonal plate - Mode 10

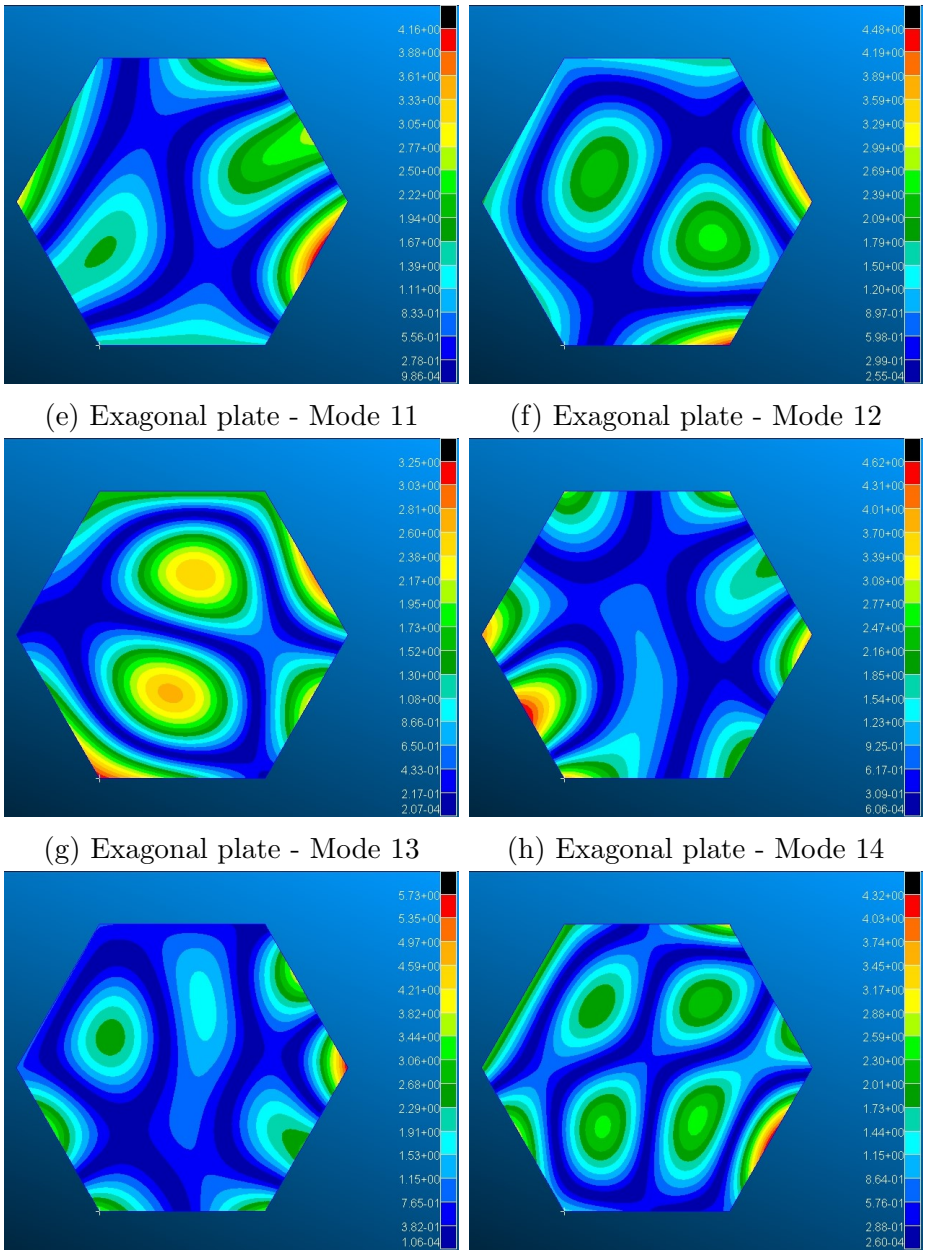

(e) Exagonal plate - Mode 11 (f) Exagonal plate - Mode 12

(g) Exagonal plate - Mode 13 (h) Exagonal plate - Mode 14

(i) Exagonal plate - Mode 15 (j) Exagonal plate - Mode 16

Figure 3.5: First ten elastic modal shape of the exagonal plate

Pentagonal plate				
Thickness	*Mass [kg]*	*Orientation*	*Eigenfreq. [Hz]*	
1 mm	0.114	$[90/45/0/-45]_{sym}$	99.196	411.489
			111.749	493.853
			163.655	585.581
			261.981	623.848
			348.015	644.163
2 mm	0.227	$[90/45/0/-45]_{2sym}$	222.753	967.450
			245.832	1028.072
			320.053	1190.100
			589.231	1324.440
			670.621	1345.743
3 mm	0.341	$[90/45/0/-45]_{3sym}$	337.893	1490.751
			367.724	1537.730
			472.743	1742.892
			905.373	1976.551
			984.082	2013.450
4 mm	0.455	$[90/45/0/-45]_{4sym}$	467.199	2053.283
			496.997	2093.056
			642.176	2385.447
			1252.585	5046.282
			1333.452	6303.491
Exagonal plate				
Thickness	*Mass [kg]*	*Orientation*	*Eigenfreq. [Hz]*	
1 mm	0.166	$[90/45/0/-45]_{sym}$	40.178	193.496
			61.473	213.056
			94.712	228.528
			110.906	284.057
			139.084	291.749
2 mm	0.333	$[90/45/0/-45]_{2sym}$	97.730	385.468
			126.491	431.684
			185.116	498.729
			236.465	605.833
			328.833	637.373
3 mm	0.499	$[90/45/0/-45]_{3sym}$	153.229	571.961
			187.645	638.031
			276.811	761.358
			357.547	917.782
			509.863	980.118
4 mm	0.665	$[90/45/0/-45]_{4sym}$	209.466	764.235
			248.376	844.377
			370.362	1042.877
			483.017	1237.417
			686.474	1346.207

Table 3.2: Influence of composite layers on the structural behaviour of plates

3.3 Flexible body in Adams

Once the input MNF files for Adams have been created, the next step is to introduce the flexible bodies into the model.
Here, the central pentagonal plate will be taken as an example.

First, the contact forces related to the rigid body that will be made flexible are removed. This is necessary because, in the previous analysis, multiple contact forces were created (one for each chaser body) to properly simulate contact with the target during the capture phase. However, since these contacts involve rigid bodies, they must be eliminated.
Next, by selecting the central pentagonal plate and using the *Make Flexible* option, the file created with Nastran is imported. It is crucial to verify that the flexible body is correctly positioned; if not, its alignment must be corrected using the software settings. There are three alignment tools available to specify the position and orientation of the replacement flexible body [14], `p.19`. In this case, *3 Point Method* was used (Figure 3.6a).

It is also important to check that all connections are properly established. Given that the exsiting body is a rigid body, Adams Flex searches for the markers on the rigid body and transfers these markers to the nodes on the replacement flexible body that are closest to the markers. If a marker is used to define joints or forces, Adams Flex searches for interface nodes. For all other markers, it searches the entire set of nodes [14], `p.19`.
In the case of the central plate, as mentioned above, the control forces are applied at the barycenter; the interface node created at the barycenter (ID 2754) serves to ensure that the previously applied forces are placed at the correct location (Figure 3.6b). The five joints that involve the central pentagonal plate are instead placed in the markers positioned at the midpoint of each side. The interface nodes were created at the same positions as described above (ID 2749:2753). It is evident that the distance between the markers corresponding to joints and forces, and the interface nodes is zero. This process serves to validate the precision of the finite element model that has been developed.

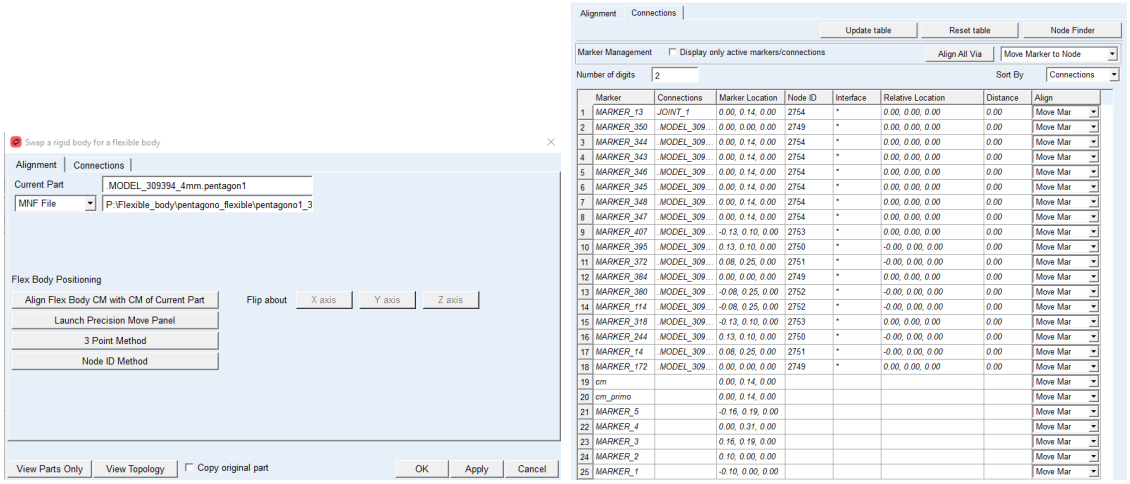

(a) Flexible body allignment (b) Flexible body connection

Figure 3.6: Steps to introduce a flexible body into the model

Figure 3.7 shows the model of the chaser after introducing flexibility in all plates.
You can notice that the mass of the chaser is now 18.76 kg, compared to 44.39 kg, in the preliminary study [7]. So, thanks to the use of CFRP, it has been possible to make considerable savings on the weight of the payload, which also results into substantial cost reductions at launch.

We will need to simulate the contact between the flexible body and the target, which is obviously different from what was done previously because the flexible body behaves differently. In fact, the flexible body behaves according to its modal representation, taking into account elastic deformations.
However, the present study will focus on the tracking, deployment, and closure of the device, without analyzing the impact phase with the target. Therefore, the contact forces previously created will be removed prior to simulation with the flexible model.

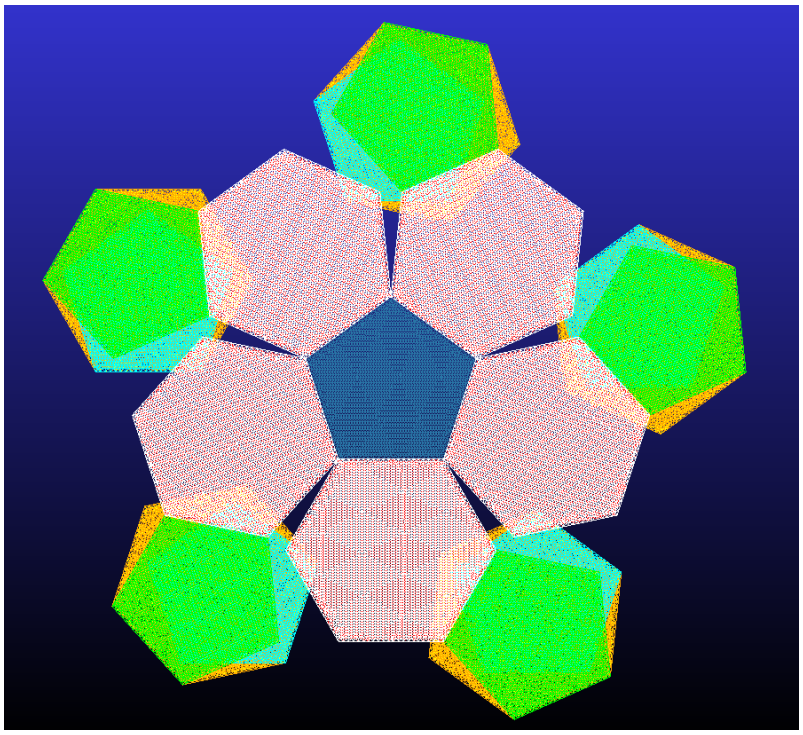

Figure 3.7: Chaser model with flexible plates

Chapter 4

Actuation system

This chapter analyses the evolution from the feasibility study [7] to the definition of a preliminary actuation system, which serves as the foundation for the final device. The process involves the transition from kinematic laws of motion, ideal and devoid of dynamic effects, to realistic force laws, capable of faithfully reproducing the behaviour of the system under the action of the actuators. These force laws represent the actual torques that the actuators will have to apply to the plates to achieve the desired motion, taking into account factors such as inertia, friction and external forces.

4.1 Laws of motion

In order to simulate the deployment and capture phases, time-dependent laws of motion have been defined, i.e. mathematical expressions that impose a certain trend of the state variable over time. These laws ensure smooth transitions between different operational configurations, allowing the system to follow optimised kinematic profiles.

Specifically, each plate follows its own law of motion, designed to satisfy geometric and kinematic constraints imposed by the system. The laws of motion have been defined in such a way as to guarantee continuity in the derivatives up to second order, avoiding sudden variations in speed or acceleration that could generate unwanted stresses.
Since the formulation of the motion laws is not the focus of this thesis, but rather a starting point, only one representative example will be shown here. However, with the improvements introduced and explained in the chapter 2, the preliminary results are different from those obtained in [7], so it is appropriate to discuss them briefly.
In MSC Adams, the laws of motion are implemented using the *MOTION* command, which in this case defines relative motion between two bodies by applying it to a pair of markers located on them. The motion law applied between the plate *pentagon 2* and the plate *hexagon 3* in the model is presented below.

$$\begin{gathered} IF(SENVAL(capt1):\ 0,\ IF(SENVAL(SENSOR\_avv):0,0, \\ STEP5(time, SENVAL(SENSOR\_avv), 0d, SENVAL(SENSOR\_avv)+25, 180d)), \\ STEP5(time, SENVAL(capt1), 180d, SENVAL(capt1)+5, 217.38d)) \end{gathered} \tag{4.1}$$

There are two IF functions in 4.1: the first evaluates the value of $SENVAL(SENSOR\_capt1)$, the second that of $SENVAL(SENSOR\_avv)$.

We now need to understand what these two elements measure.
There are two sensors in the function, *SENSOR_capt*1 and *SENSOR_avv*; the first one measures the rotation of plate p_2 with respect to plate e_1, the second one measures the relative distance between the chaser and the target. The first is activated when the plate p_2 completes the rotation of 37.38° with respect to the plate e_1, at which time the capture phase that regards the plates p_2 and e_3 begins; the second is activated when the chaser is at a distance of 10 meters from the target, at which time the deployment phase begins. The sensors have been defined so as to assess the time instant at which the event occurs. This is achieved by asking *time* as output in *Event Evaluation*, as shown in the figure 4.1.
For example, the *SENSOR_avv* is activated at the instant in time when the distance along the z-axis between the chaser and the target is, in absolute value, less than or equal to 10 meters, with a tolerance of 10^{-4}. The part under *Standard Actions* has been set so that an output is generated when the sensor is activated and the simulation continues. Using the sensors, it will be necessary to run a scripted simulation, which will be discussed in more detail later.

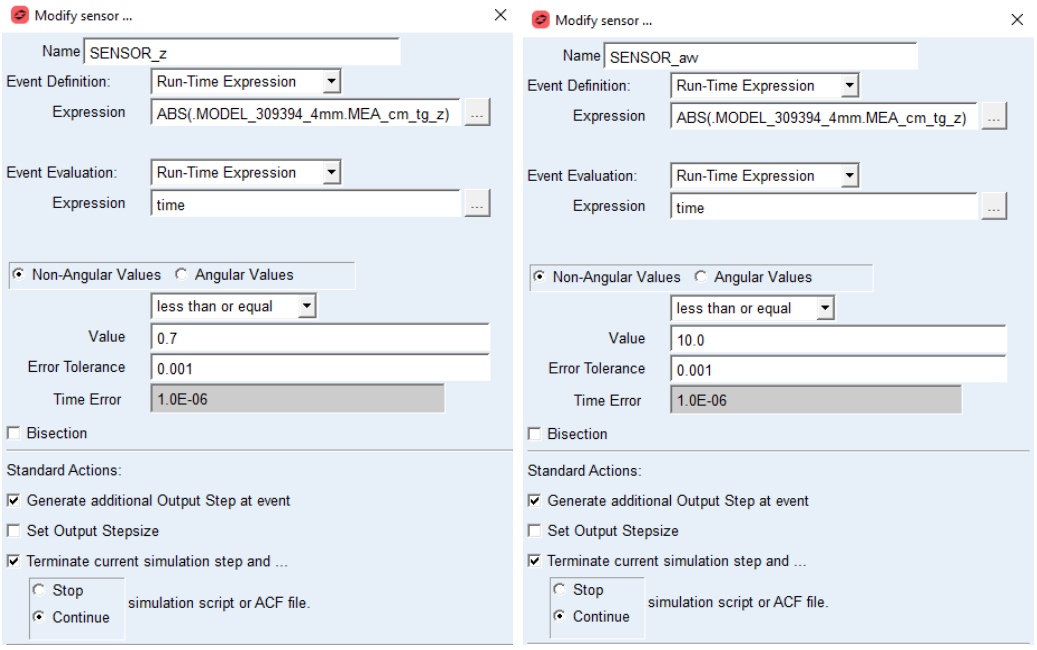

(a) *SENSOR_z* definition (b) *SENSOR_avv* definition

Figure 4.1: *SENSOR* setup

The function *SENVAL* of a sensor defined in this way has the value of 0 when the sensor is deactivated, and a certain value different from 0 when it is activated. In the field of *Event Evaluation*, the temporal instant at which the sensor is activated is requested as output. Consequently, the function *SENVAL* can be incorporated within the function *STEP5* in the time domain to utilize precisely this instant of time as the initial instant.

Putting together *STEP5* and *SENVAL* ensures that when *SENSOR_avv* is deactivated, i.e. when the chaser and target are more than 10 meters apart, no movement takes place; when they are 10 meters apart the plate *esagono 3* rotates 180° with respect to the plate *pentagono 2* in a gradual manner and in a time interval of

25 seconds, passing from the compact to the deployed configuration.

Finally, when the $SENSOR\_capt1$ is activated, i.e. when the second step of the capture phase has been completed, the closing phase begins, which as far as these two plates are concerned is a further rotation of 37.38° of the plate *esagono 3* on the plate *pentagono 2*, again smoothly and gradually, over a time interval of 5 seconds, resulting in the configuration depicted in the last figure in 2.4.

4.1.1 Kinematic analysis results - deployment

Once all laws of motion have been properly applied, a kinematic analysis is performed. This analysis provides the time histories of angles, angular velocities, and torques, which serve as inputs for the subsequent dynamic analysis.
In this first part, only the unfolding motion is analysed, without considering the capture phase; therefore only the first part of the law of motion described in 4.1 is considered.
The torque profiles acting on the joints during deployment are shown in Figure 4.2. These results were obtained by simulating the updated configuration described in Chapter 2, but after modifying the geometry of the device, i.e. with 4 mm thick plates. As a result, the torques are lower than those shown in Figure 2.18.

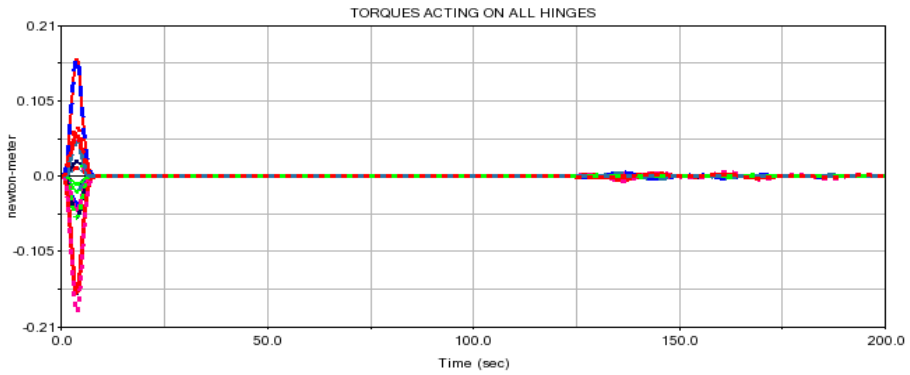

Figure 4.2: Trend of torques acting on joints during the deployment phase

Continuing with the selected example, the profiles of angular displacement, angular velocity between the two plates and the torque acting on the corresponding joint are shown.

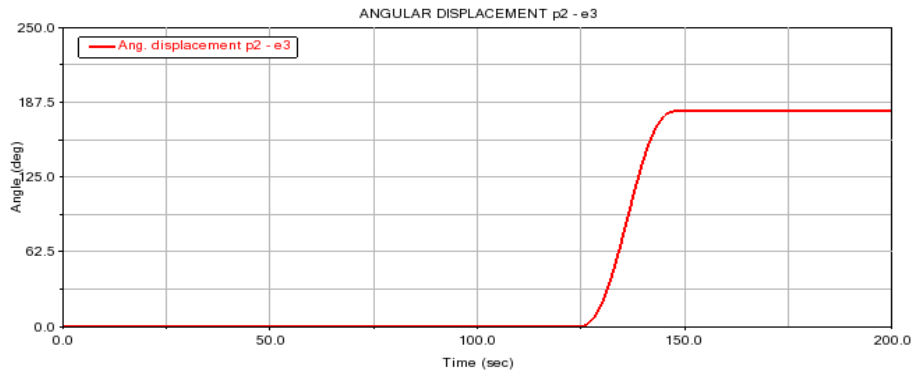

Figure 4.3: Trend of angular displacement between the two plates

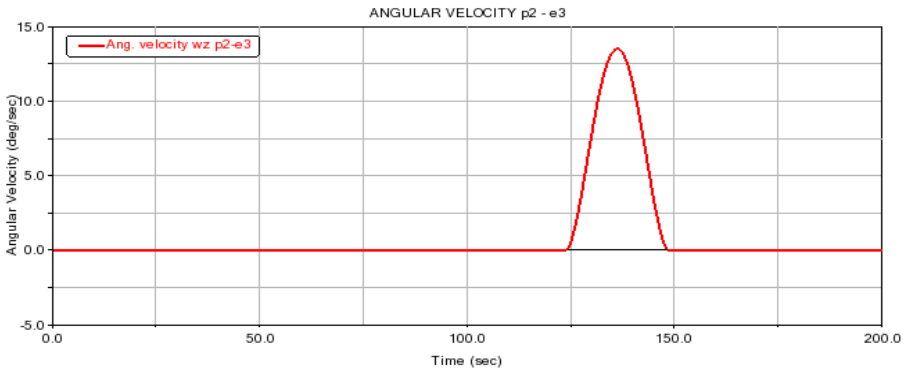

Figure 4.4: Trend of angular velocity of the hinge between the two plates

It can be seen that at the beginning of the simulation, the angle between the two plates is zero, since deployment only occurs when the chaser is 10 meters from the target. At this point, the law of motion imposes a movement of 180° in 25 seconds, after which it keeps the two plates locked.
The trend of the angular velocity of the hinge shows that the movement occurs exclusively during the 25 seconds of the deployment, while it is null for the rest of the simulation time. In the figure 4.4, it can be seen that the STEP5 function ensures smooth and uniform motion, thanks to its ability to smoothly connect to the initial and final values, avoiding drastic speed variations.

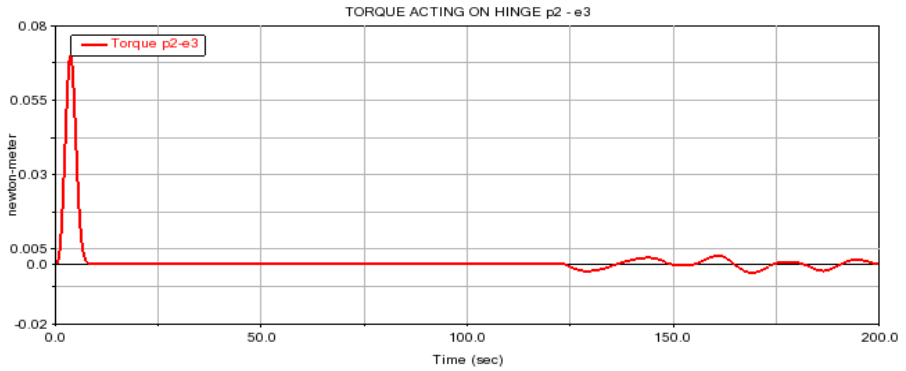

Figure 4.5: Torque trend obtained from the law of motion

Figure 4.5 shows the trend of the torque that the law of motion imposes on the joint. It can be seen that it is not different from zero only during the 25 seconds of deployment. This is due to the reaction torque applied to maintain the angle between the two plates at 180°. The deployment of the plate *esagono 3* on the plate *pentagono 2* is the most complex in the entire model, since after it, three more deployments will occur on the plate *esagono 3*, more than on any other body in the model.
As already mentioned in the chapter 2, the deployment occurs on three levels and lasts a total of 75 seconds; which is why the torque obtained from the law of motion is different from 0 in the 75 seconds of the complete deployment.
However, the actual deployment of only plate *esagono 3*, which also takes the others with it, occurs in 25 seconds; the next torque is a reaction torque to the movements of the other plates, which serves to lock *esagono 3* in the desired position.

It can also be seen that there is an initial spike. This is due to the attitude control torques discussed earlier. The modification made to the alignment and pursuit forces, that is reflected to attitude control torques, caused this peak to be significantly lower than in the preliminary study and to be smoother. With regard to the sizing of the actuation system, one could actually ignore this and consider the start of the simulation a few moments later, but in this study will be taken into account.

4.1.2 Kinematic analysis results - capture

As with deployment, Figure 4.6 shows the torque trends acting on all joints during the closing phase of the device.

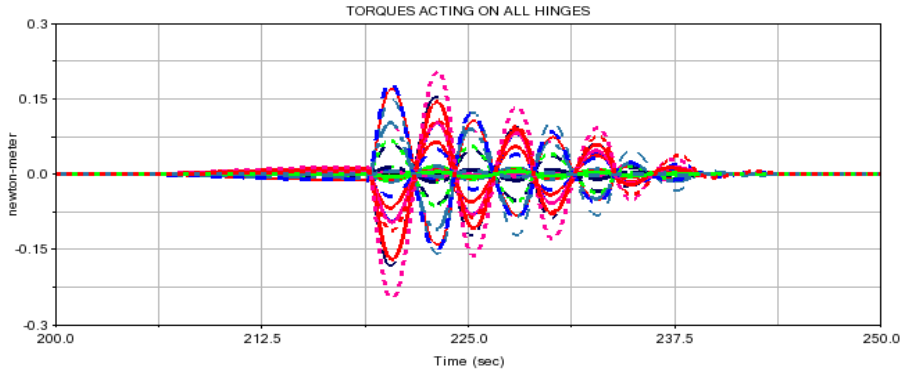

Figure 4.6: Torques acting on all hinges during capture phase

During the capture phase, the angle between the pentagon and the hexagon is 142.62°, and the angle between the two regular hexagons is 138.19° [8].
Consequently, a relative rotation of $\Delta\theta = 37.38°$ occurs between a pentagonal plate and an adjacent hexagonal plate, and $\Delta\theta = 41.81°$ between two adjacent hexagonal plates.
Once again, the movement between the plates *pentagono 2* and *esagono 3* is used as a representative example. The trends of the rotation between the two plates and the torque that allows this movement to occur are also shown.

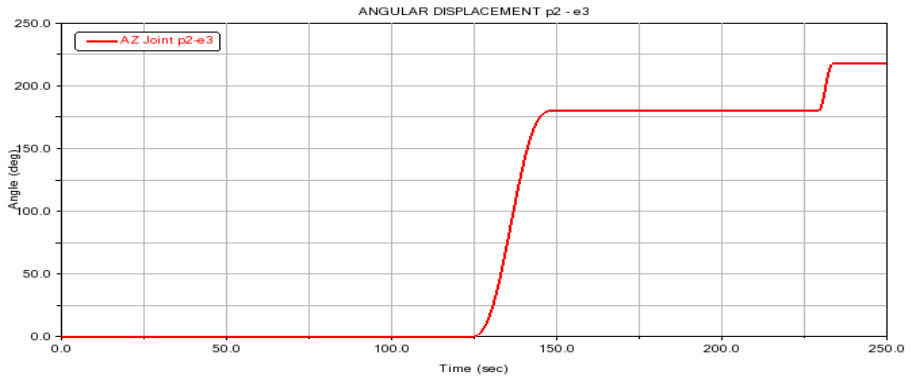

Figure 4.7: Rotation of the plate e_3 with respect to p_2

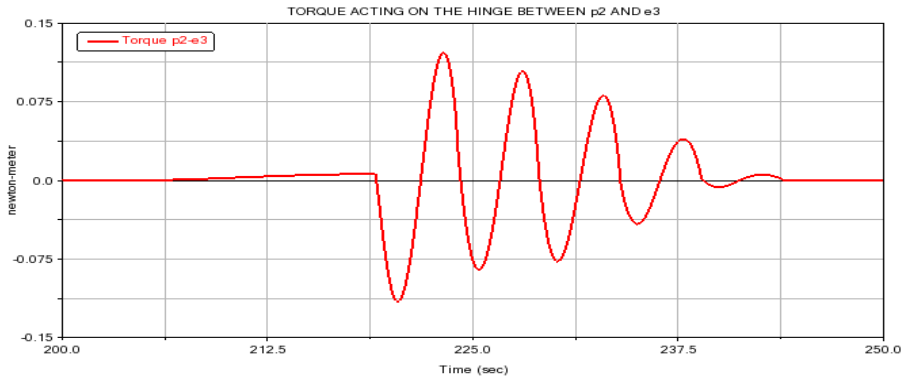

Figure 4.8: Torque acting on the hinge between p_2 and e_3

The law of motion that governs this movement is the second part of 4.1.
It has been observed that the closure phase of the device commences prior to the movement of these two plates to catch. This is due to the fact that the *pentagono 2* and *esagono 3* move in the third step of the closing phase. Accordingly, the trends preceding and following this step delineate a torque that serves to maintain the angle between the two plates at 180° before and 217.38° after.
The capture phase is initiated, and as long as the sensor *SENSOR_capt1* is not activated, the two plates maintain an angle of 180° between them. The *SENSOR_capt1* sensor is responsible for measuring the angle between the plate *esagono 1* and the plate *pentagono 2*. The sensor is activated when the angle between these two plates reaches 37.38°, given that the initial relative angle was 0°, a rotation of $\Delta\theta = 37.38°$ is consistently introduced throughout the capture phase. This sensor activation corresponds to the completion of the second closing step.
When this sensor is triggered, the law *STEP5* allows smooth movement between *pentagono 2* and *esagono 3*. This movement generates an angle of 217.38° between the plates, within a time interval of five seconds.

4.2 Dynamic analysis - rigid model

The objective is to replicate the angular displacement and velocity profiles by applying a dynamic torque to the plates, which is expected to follow a trend similar to that shown in Figure 4.5.
The kinematic law of motion is replaced by a rotational *Single-Component Force*, which applies a torque to the two bodies to which it is applied.
The *MOTION* element previously used to control angular displacement is thus replaced by a torque that reproduces the same motion profile.
The *SFORCE* element in Adams is of the *Rotational* type and is applied to the two markers corresponding to the reference joint.
The analysis presented here was conducted on the rigid model, prior to the integration of flexible bodies.

4.2.1 Deployment phase

We now focus on the deployment phase only. Figure 4.9 provides a zoomed-in view of Figure 4.5, highlighting the time interval in which the deployment actually takes place.

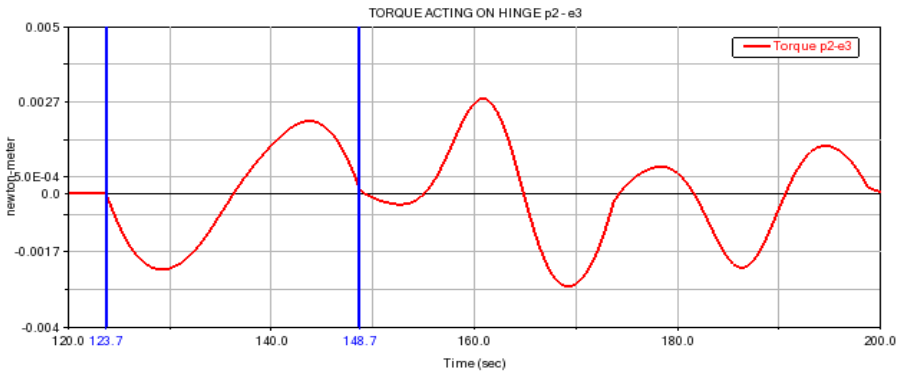

Figure 4.9: Representation of the segment of the torque trend in which the actual unfolding of e_3 on p_2 occurs

The approach used in this work involves the use of *STEP5* functions during the effective deployment (segment between the vertical blue lines in Figure 4.9), and a Proportional-Derivative (PD) control for the rest of the time, thus controlling displacement and angular velocity.
A PD control system quantifies the discrepancy between the desired value and the current value of the selected quantity, generating an output that is proportional to this discrepancy. The derivative action of the system contributes to its stabilization, reducing oscillations, while taking into account the rate of change of the current value.
It is therefore necessary to consider that of the entire trend of the torque, obtained from the kinematic analysis, only the 25 seconds following the beginning of the deployment should be replicated as faithfully as possible with the *STEP5*. All the rest of the trend should be replicated through the control system.
It is noted how the trend of the torque in the deployment phase is assimilated to a complete sinusoid. Therefore it can be well represented by the sum of three *STEP5* functions:

$$\begin{aligned} &STEP5(time, SENVAL(SENSOR\_avv), 0, SENVAL(SENSOR\_avv) + 5, C_{max}) + \\ &STEP5(time, SENVAL(SENSOR\_avv) + 5, 0, SENVAL(SENSOR\_avv) + 20, \\ &-(C_{max} + C_{min})) + \\ &STEP5(time, SENVAL(SENSOR\_avv) + 20, 0, SENVAL(SENSOR\_avv) + 25, C_{min}) \end{aligned} \tag{4.2}$$

Writing the function in this way allows the sinusoidal profile to be divided into three segments: the first, where it gradually increases from zero to its maximum; the second, where it decreases from maximum to minimum; and the third, where it rises again from minimum back to zero. The durations of these intervals have been chosen to closely replicate the kinematic profile, with the first segment lasting 5 seconds, the second 15 seconds, and the third 5 seconds, for a total deployment time of 25 seconds.

As previously mentioned, the deployment between these two plates is the most complex. A sensor named *SENSOR_disp1* has been added to monitor the rotation

angle between the two bodies. In the *Event Evaluation* tab, the sensor is set to output the activation time, which is then used to trigger the subsequent deployment phase.

As for the PD control system, it has been defined as follows:

$$-K\ (\theta - \theta_{des}) - C\ (\dot{\theta})$$

where:

- θ: actual angle;
- θ_{des}: desired angle, the one you want to maintain at the end of the deployment;
- $\dot{\theta}$: actual angular velocity.

K and C are respectively the proportional gain and the derivative gain of the PD control system that will serve to keep the plates in the desired position.
These control laws will correct any deviation due to external disturbances. Obviously there is a subtractive term in the proportional term since a certain angle θ_{des} must be maintained, while the derivative term is used to avoid oscillations and maintain zero angular velocity at the end of the unfolding.
Furthermore, there will be two different control phases, with different parameters. The first control is to be done in the initial phase, before deployment, in which the angle between the two plates must remain zero. The second control concerns the phase after deployment, in which this angle must remain equal to 180°.
Since with the sum of *STEP5* it is possible to reach 180° almost perfectly, therefore the control will be softer, with a very low proportional gain and a higher derivative gain, to avoid oscillations from the deployed configuration especially during subsequent deployments.
The coefficients K and C have been preliminarily chosen and for these two plates they are respectively 0.1 Nm/rad and 0.4 Nms/rad for the initial control, 0.0002 Nm/rad and 0.05 Nms/rad for the subsequent one.

In conclusion, the *Single-Component Force* replicating the movement of the two plates, in the first part of the simulation is defined as:

$$\begin{aligned} &IF(SENVAL(SENSOR\_capt1):\ 0,\ IF(SENVAL(SENSOR\_avv):\ 0,\\ &\quad -0.1(\theta - 0) - 0.4(\dot{\theta}),\ IF(SENVAL(SENSOR\_disp1):\ 0,\ STEP5..., \\ &\qquad -0.0002(\theta - 180) - 0.05(\dot{\theta}))),\ \textbf{“CLOSING PHASE”}) \end{aligned} \tag{4.3}$$

When $SENSOR\_capt1$ and $SENSOR\_avv$ are deactivated, i.e. chaser is more than 10 meters from the target, the control system maintains the angle between the plates equal to zero; when $SENSOR\_avv$ is activated, i.e. the chaser is less than 10 meters from the target, but $SENSOR\_disp1$ is deactivated, meaning the angle between the two plates is less than 180°, the functions *STEP5* deploy the plate *esagono 3* on the plate *pentagono 2*; when $SENSOR\_disp1$ is activated, the control system locks the plates in the desired configuration and maintains the angle equal to 180°; when $SENSOR\_capt1$ is activated, the closing phase begins, which will be discussed later.

Below are the displacement and angular velocity profiles, as well as the torque applied through the *SFORCE*, comparing the results of the kinematic analysis with those of the dynamic analysis.

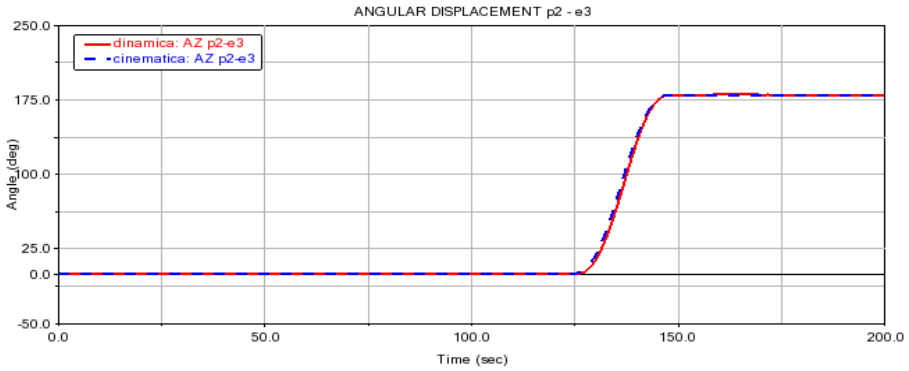

Figure 4.10: Comparison of angular displacement in kinematic and dynamic analysis

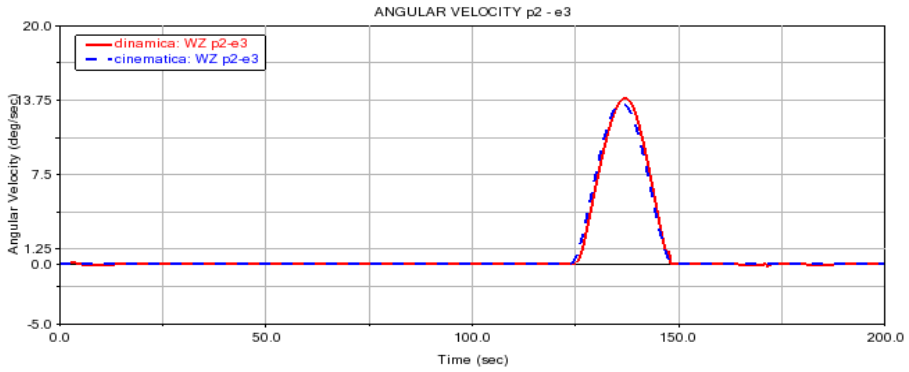

Figure 4.11: Comparison of angular velocity in kinematic and dynamic analysis

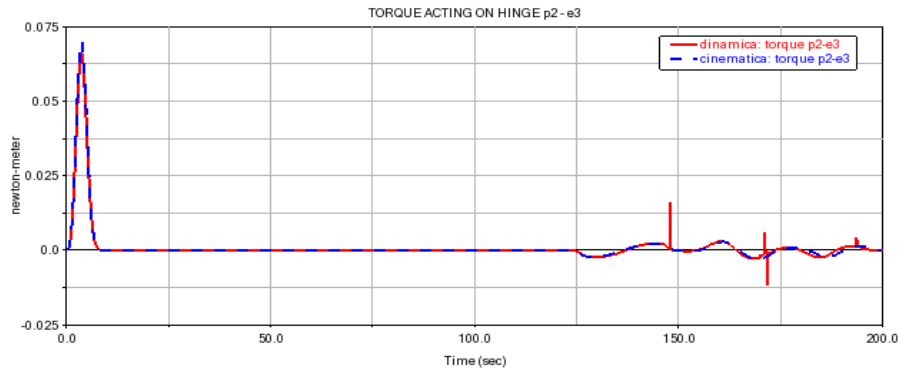

Figure 4.12: Comparison of torque in kinematic and dynamic analysis

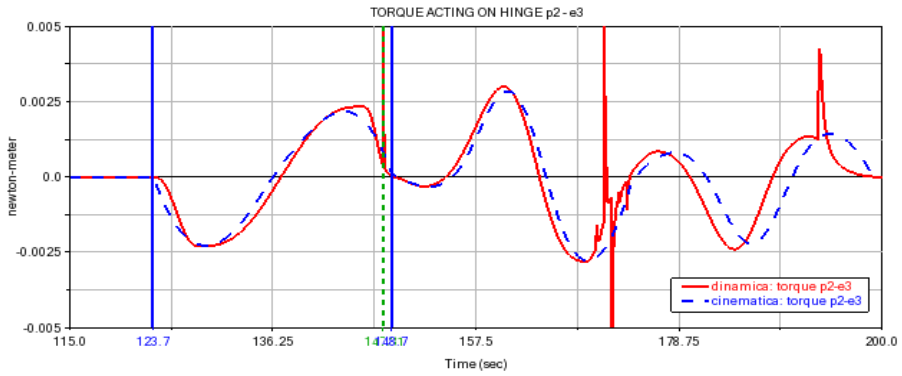

Figure 4.13: Comparison of the segment of the torque trend in which the actual unfolding occurs

It can be seen that, except for small deviations, the trends almost perfectly mirror those obtained in the kinematic analysis.
The control system induces a torque that closely matches that induced by the law of motion, so the approach used is considered satisfactory.
It is evident that the results of the dynamic analysis exhibit peaks, which can be attributed to the inability to perfectly replicate the outcomes obtained in kinematics (Figure 4.13). This is due to the fact that *STEP5* functions follow their own distinct mathematical laws, which differ from those of kinematics. Consequently, the condition for sensor activation is not met within precisely 25 seconds, as in kinematics, but rather within 24.1 seconds.
With regard to the functions describing the trend of the torques applied to the plates for the successive steps of deployment, further considerations must be made. The kinematic analysis reveals that the torque required for the initial step of deployment commences at zero and concludes after twentyfive seconds, at which point it reverts to zero. This is not the case for the subsequent steps. Consequently, it was necessary to preserve the initial values of the *STEP5* function governing each of the applied torques.
This objective was accomplished by defining other sensors. However in this case the focus was not on the time instant at which the sensor is activated, but rather on the value of a measurement.
In particular, the measurements of each of the deployed torques were created, and in the *Event Evaluation* section of the sensor setting, these measurements were entered. In contrast, the measurement of the angle from the preceding deployment was entered in the *Event Definition* section.
In summary, the second step of deployment is initiated when the plate *esagono 3* undergoes a 180° rotation in relation to the plate *pentagono 2*, which remains stationary. This process results in the creation of an equal number of sensors as there are plates involved in that step.

Given that the device is equipped with five identical fingers, with the exception of one that is distinguished by an additional pentagon, it was necessary to ensure that all plates involved in a given deployment step complete their movement within the same time interval.

The third and final deployment step pertains to the pentagonal plate alone, designated as *pentagono 4*, which is required to rotate precisely 180 degrees with

respect to the hexagonal plate, designated as *esagono 4*. Therefore, a sensor is created that evaluates the time instant at which the second step of deployment is completed (i.e., the hexagon 4 rotates 180° relative to the hexagon 3) and another that evaluates the value of the torque applied on the hinge connecting the plate *pentagono 4* and the plate *esagono 4* at the instant that the previous step is complete.
The purpose of these sensors is to eliminate discontinuities in the trend of the torques. These discontinuities would otherwise occur because it is impossible to determine the starting value of the *STEP5* a priori. Initiating the *STEP5* from the null value would introduce a discontinuity, as the torques are not null prior to the initiation of the actual deployment; however, they do exhibit a specific trend in order to maintain the position of the plates before the actual deployment.

The figures 4.14 4.15 illustrate the trends of the angular displacements and the torques relating to a plate involved in the second step, as well as those relating to the third step. These figures are intended to facilitate comprehension of the subject matter.
It is evident that the temporal interval during which these steps occur in the kinematic analysis, as delineated by the blue vertical lines in the figures, exhibits slight discrepancies compared to the dynamics depicted by the green lines. The impracticability of replicating such behavior is attributable to the fact that the *STEP5* functions are subject to a course defined by their own mathematical law, which is distinct from that obtained in kinematics.

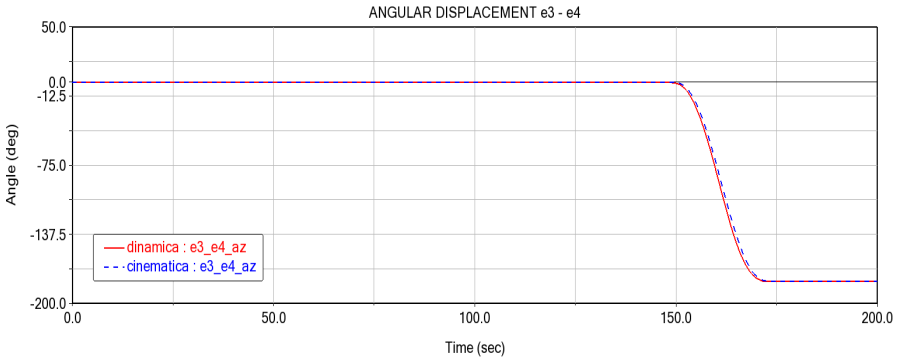

(a) Angular displacement

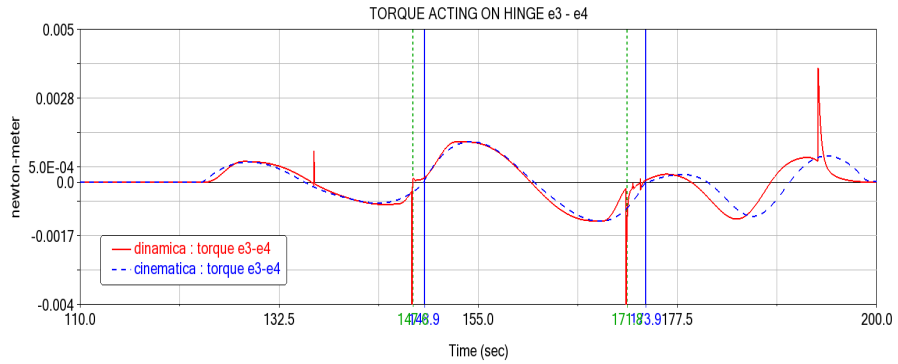

(b) Torque trend

Figure 4.14: Trend of torque acting on the hinge and rotation between e_3 and e_4

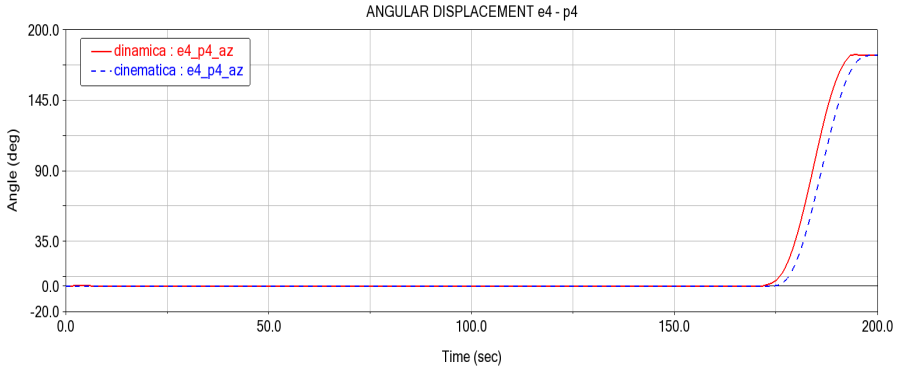

(a) Angular displacement

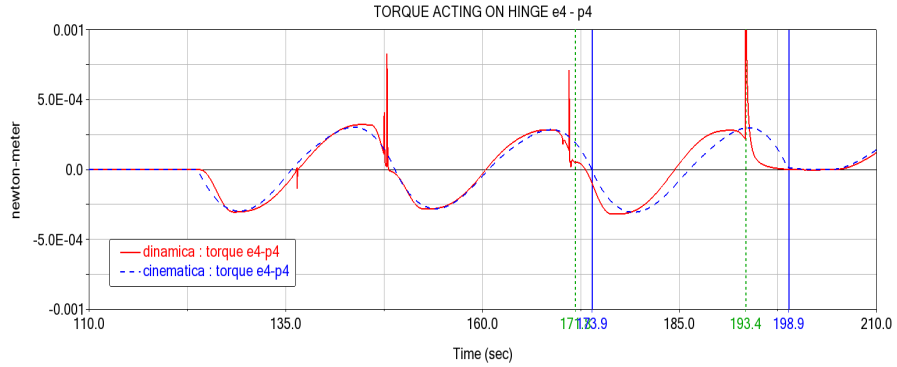

(b) Torque trend

Figure 4.15: Trend of torque acting on the hinge and rotation between e_4 and p_4

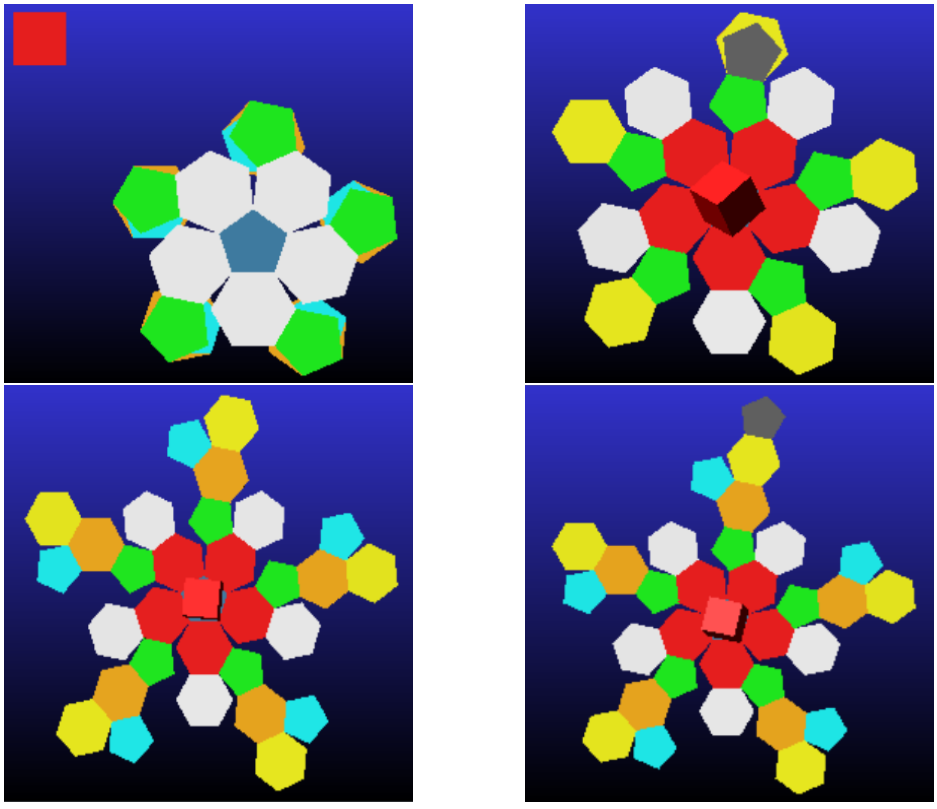

Figure 4.16: Frames of chaser's deployment phases

4.2.2 Capture phase

In the capture phase, a methodology analogous to the deployment phase has been employed.
The closing phase of the device, aimed at collecting the debris, is initiated upon activation of the sensor, designated as *SENSOR_z*. This activation occurs when the center of mass of the chaser reaches a distance of less than or equal to 0.7 meters from the center of mass of the target.
The hexagonal plates rotate at an angle of 37.38° with respect to the adjacent pentagonal plates and at an angle of 41.81° with respect to the hexagonal plates.
As previously stated in the paragraph 2.4, the capture phase has undergone modifications in comparison to the preliminary study [7]. The capture phase has been subdivided into five steps, each lasting five seconds. In the capture phase, the plates that remain stationary in the deployment also rotate, i.e. all those that are depicted in the first image in the figure 4.16. It has been chosen to involve in the first capture step all the hexagonal plates surrounding the central pentagon, and in the second step all the pentagonal plates connected to them.
This improves and simplifies the control of the entire movement and also reduces the torques required to complete it.

The philosophy behind the definition of torques is analogous to that employed in the deployment phase. In order to elucidate this phenomenon, the hinge connecting the pentagonal plate, designated as p_{1e} and the hexagonal plate, denoted by e_1, during the second step is examined as a case study. A similar approach is adopted to analyze the hinge linking the pentagonal plate, referred to as p_2 with the hexagonal plate, labeled as e_3 in this case, for the third step. In this manner, the reasoning can be more readily comprehended, as both of these movements are preceded and followed by other steps.

A thorough examination of the torque relative to the motion between p_{1e} and e_{1e} obtained from the kinematic analysis reveals a certain oscillatory pattern throughout the time of the capture. Consequently, the temporal interval during which the observed motion occurs between these two plates must be determined. The aforementioned phenomenon can be ascertained by examining the kinematic simulation report to identify the specific moment at which the sensor, designated as *SENSOR_capt0*, is triggered. This particular sensor is responsible for evaluating the angular displacement between the pentagonal plate, designated as p_1, and the hexagonal plate, denoted as e_1. The sensor is activated under specific conditions, namely when the angle between these plates exceeds or equals 37.38°. This threshold is defined as the completion of the first capture step.
As illustrated in Figure 4.17, the time interval commencing at this instant and concluding five seconds later is isolated (vertical blue lines). That is to say, this time interval encompasses the duration of the second step. As is evident, the initial value of the torque required for movement is not zero; therefore, this value must be stored somehow.
This objective is realized through the implementation of a sensor that assesses the torque's value upon the occurrence of the event defined by the sensor.
Given this initial value, it is then possible to compute the sum of *STEP5*, which

endeavors to delineate the trend of the torque derived from the kinematics:

$$\begin{gathered} STEP5(time, SENVAL(SENSORcapt0), SENVAL(SENSOR\_p1e\_e1e), \\ SENVAL(SENSORcapt0)+1, C_{max})+ \\ STEP5(time, SENVAL(SENSORcapt0)+1, 0, SENVAL(SENSORcapt0)+4, \\ -(C_{max}+C_{min}))+ \\ STEP5(time, SENVAL(SENSORcapt0)+4, 0, SENVAL(SENSORcapt0)+5, C_{min}) \end{gathered} \tag{4.4}$$

This sum of functions goes into the force function that governs the movement of the two plates throughout the duration of the simulation.
With regard to the deployment, a PD control is utilized for the remaining duration. The complete function of the torque acting on this hinge is then defined as follows:

$$\begin{gathered} IF(SENVAL(SENSOR\_z):0, -0.1(\theta_{p1e\_e1e}-0)-1.2(\dot{\theta}_{p1e\_e1e}), \\ IF(SENVAL(SENSOR\_capt0):0, -0.1(\theta_{p1e\_e1e}-0)-0.8(\dot{\theta}_{p1e\_e1e}), \\ IF(SENVAL(SENSOR\_capt1):0, \\ IF(\theta_{p1e\_e1e}-37.38 : STEP5..., 0, -0.01(\theta_{p1e\_e1e}-37.38)-0.4(\dot{\theta}_{p1e\_e1e})), \\ -0.01(\theta_{p1e\_e1e}-37.38)-0.4(\dot{\theta}_{p1e\_e1e})))) \end{gathered} \tag{4.5}$$

The sensor *SENSOR_capt1* is responsible for evaluating the rotational movement of the pentagonal plate *pentagono 2* with respect to the hexagonal plate *esagono 1*. The sensor is activated when the angular displacement exceeds or equals 37.38 degrees. This threshold is met upon the completion of the second capture step.
The force function, as delineated, ensures that, provided the chaser is situated at a distance greater than 0.7 meters from the target, the PD control system maintains the angle between p_{1e} and e_{1e} at a value of zero. Upon arriving at a distance of 0.7 meters from the target, thereby initiating the capture phase, it still maintains the angle equal to zero until the sensor *SENSOR_capt0* is activated, signifying the completion of the first step.
At this point, the system permits a gradual rotation of p_{1e} with respect to e_{1e} by means of a sum of *STEP5*. Upon completion of the second step, the angle is maintained at 37.38° until the conclusion of the simulation, once more with a PD control.

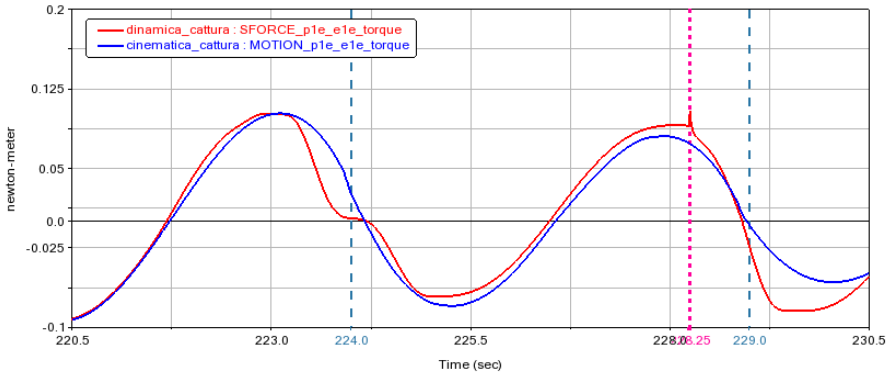

Figure 4.17: Comparison of the kinematic and dynamic torque acting on the hinge between p_{1e} and e_{1e}

It is evident that the second closing step does not occur in a precise time span of 5 seconds; rather, it occurs in a time span of 4.25 seconds. This is due to the

impossibility of perfectly tracing the trend obtained from the kinematic analysis, as the *STEP5* has its own mathematical function which is different and smoother. However, the trend of the torque is deemed acceptable, and the angle gradually and relatively smoothly transitions from zero to 37.38° as depicted in the figure 4.18.

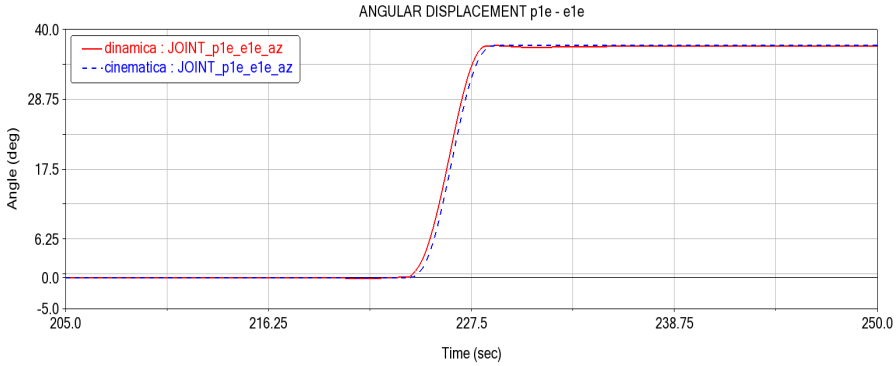

Figure 4.18: Comparison of the angular displacement of plate p_{1e} with respect to e_{1e}

In regard to the third step, the movement between the hexagonal plate *esagono 3* and the pentagonal plate *pentagono 2*, which was previously utilized as an example for deployment, is also examined.
The torque is defined as follows, with the deployment part of the function excluded:

$$IF(SENVAL(SENSOR\_capt0) : -0.02(\theta_{p2\_e3} - 180) - 0.2(\dot{\theta}_{p2\_e3}),$$
$$IF(SENVAL(SENSOR\_capt1) : 0, -0.02(\theta_{p2\_e3} - 180) - 0.2(\dot{\theta}_{p2\_e3}),$$
$$IF(SENVAL(SENSOR\_capt2) : 0, STEP5..., -0.001(\theta_{p2\_e3} - 217.38) - 0.4(\dot{\theta}_{p2\_e3}))))) \tag{4.6}$$

The application of the actual movement is executed using the conventional sum of *STEP5*.
In this scenario, after the deployment phase and prior to the completion of the second closing step, the PD control system maintains the angular orientation between the two plates at 180°. Upon activation of the sensor *SENSOR_capt1*, the *STEP5* functions effect a displacement of the plate until the angle between it and the other element is altered from 180° to 217.38°. This results in a $\Delta\theta$ of 37.38°.

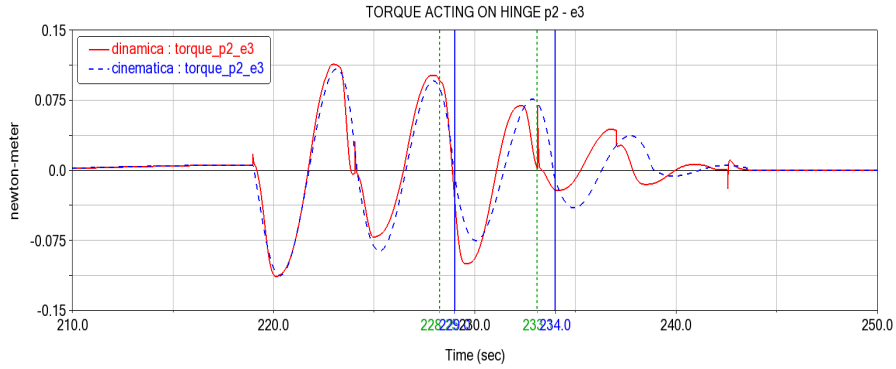

Figure 4.19: Comparison of the torque acting on the hinge between p_2 and e_3

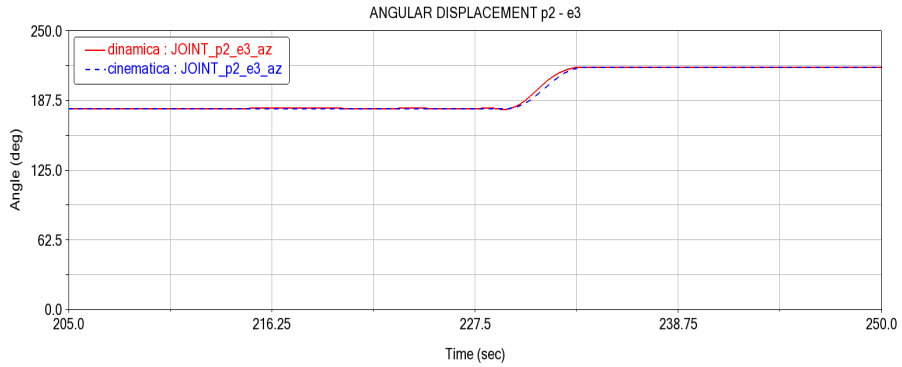

Figure 4.20: Comparison of the angular displacement of plate p_2 with respect to e_3

```
! Insert ACF commands here:
SIMULATE/DYNAMIC, END=250.0, DTOUT=1.0E-02
DEACTIVATE/SENSOR, ID=6
SIMULATE/DYNAMIC, END=250.0, DTOUT=1.0E-02
DEACTIVATE/SENSOR, ID=5
SIMULATE/DYNAMIC, END=250.0, DTOUT=1.0E-02
DEACTIVATE/SENSOR, ID=2
SIMULATE/DYNAMIC, END=250.0, DTOUT=1.0E-02
DEACTIVATE/SENSOR, ID=31
SIMULATE/DYNAMIC, END=250.0, DTOUT=1.0E-02
DEACTIVATE/SENSOR, ID=3,10,11,12,13,14,15,16,17,18,19
SIMULATE/DYNAMIC, END=250.0, DTOUT=1.0E-02
DEACTIVATE/SENSOR, ID=4,20
SIMULATE/DYNAMIC, END=250.0, DTOUT=1.0E-02
DEACTIVATE/SENSOR, ID=32
SIMULATE/DYNAMIC, END=250.0, DTOUT=1.0E-02
DEACTIVATE/SENSOR, ID=7
SIMULATE/DYNAMIC, END=250.0, DTOUT=1.0E-02
DEACTIVATE/SENSOR, ID=1
SIMULATE/DYNAMIC, END=250.0, DTOUT=1.0E-02
DEACTIVATE/SENSOR, ID=33,34,35,36,37,38
SIMULATE/DYNAMIC, END=250.0, DTOUT=1.0E-02
DEACTIVATE/SENSOR, ID=21,22,23,24,25
SIMULATE/DYNAMIC, END=250.0, DTOUT=1.0E-02
DEACTIVATE/SENSOR, ID=8,26,27,28,29,30
SIMULATE/DYNAMIC, END=250.0, DTOUT=1.0E-02
DEACTIVATE/SENSOR, ID=9,39,40,41,42,43,44,45,46,47,48
SIMULATE/DYNAMIC, END=250.0, DTOUT=1.0E-02
DEACTIVATE/SENSOR, ID=49
SIMULATE/DYNAMIC, END=250.0, DTOUT=1.0E-02
DEACTIVATE/SENSOR, ID=50,51
SIMULATE/DYNAMIC, END=250.0, DTOUT=1.0E-02
DEACTIVATE/SENSOR, ID=52
SIMULATE/DYNAMIC, END=250.0, DTOUT=1.0E-02
```

Figure 4.21: Simulation script

The simulation script developed for this analysis is also provided here. Given the presence of multiple sensors, a scripted simulation is required, in which each sensor must be appropriately deactivated in order to allow the simulation to progress. In the sensor settings, the option *Terminate current simulation step and continue simulation script* was enabled.
This script enables the execution of a dynamic simulation lasting 250 seconds, allowing the visualization of the chaser's deployment phase and the initial capture of the target. However, the simulation is intentionally halted before the target makes contact with the chaser's plates, which would occur later under the defined initial conditions.
The impact phase with the target is not analyzed within the scope of this study.
In each line of the script, the sensors corresponding to a specific step are deactivated

sequentially: first those monitoring alignment, then those related to deployment (in stepwise order), and finally those controlling the closure of the chaser (also in stepwise order).

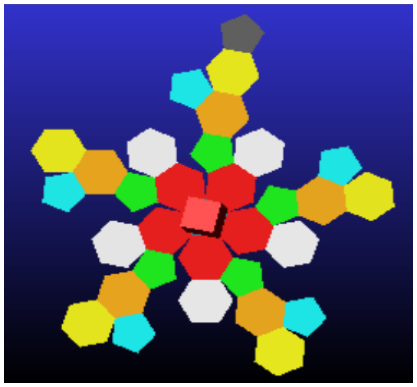

(a) Approaching the target

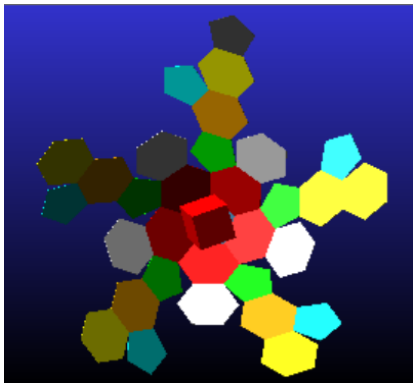

(b) Capture phase, step 1

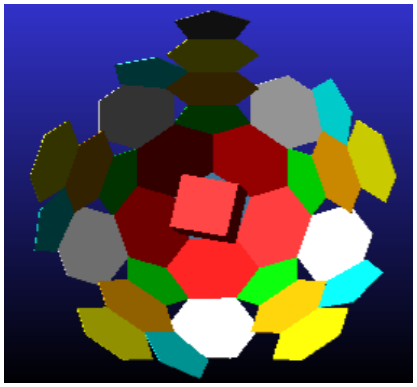

(c) Capture phase, step 2

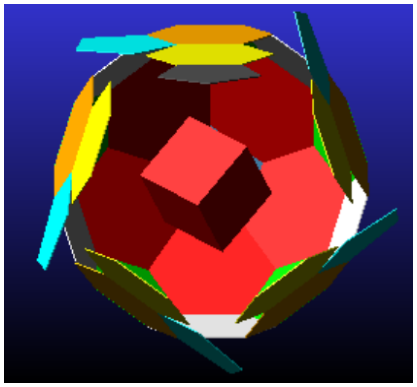

(d) Capture phase, step 3

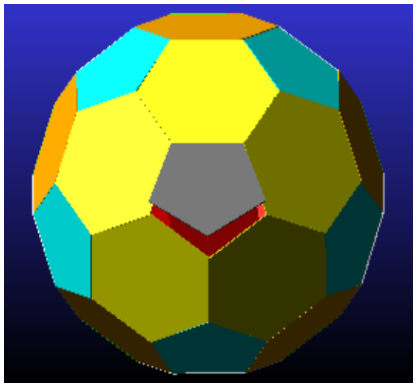

(e) Capture phase, step 4

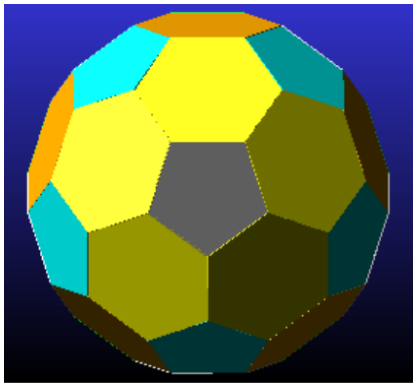

(f) Capture phase, step 5

Figure 4.22: Frames of capture phases

4.3 Dynamic analysis - flexible model

All of the preceding analyses have been conducted on the rigid model. It is now necessary to introduce the flexibility of the bodies.
Prior to initiating the analysis, all contact forces inherent within the model were eliminated. These forces corresponded to interactions between rigid bodies and were characterized by a contact model of the *Impact* type. This model is not well-suited

for simulating flexible bodies. In consideration of the actuation system and the dimensional parameters previously delineated, it is evident that there have been no alterations. The geometry of the device remains unmodified. Elimination of contact forces does not result in change, as the phase of contact with the target is not thoroughly explored in this study, as previously mentioned.
Given the identical geometry, the inertias of the bodies are equivalent to those of the rigid model. Consequently, the torques necessary for deployment and closure remain constant, as illustrated in Figure 4.23. This figure presents the torques exerted on all joints, derived from the kinematic analysis of the flexible model. It is noteworthy that these values are equivalent to those depicted in Figures 4.2 4.6.
However, the method used by Adams to calculate the inertias of the bodies is subject to variation. In the dialogue box for each of the bodies, the option of *partial coupling* is selected in Inertia Modeling, as also imposed in modal analyses in MSC Nastran.

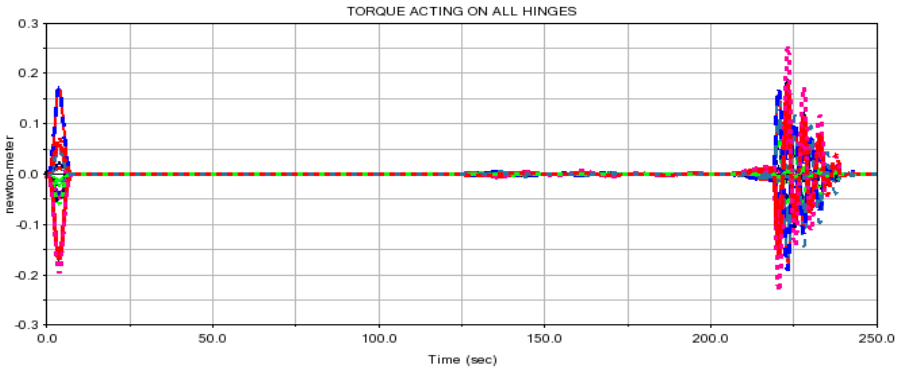

Figure 4.23: Torques acting on all hinges in the flexible model, kinematic simulation

Subsequently, the dynamic simulation is restarted, and the resulting torque profiles are shown in the Figure 4.24.
Representative frames from the simulation are also displayed, providing a visual overview of the deployment and capture phases.

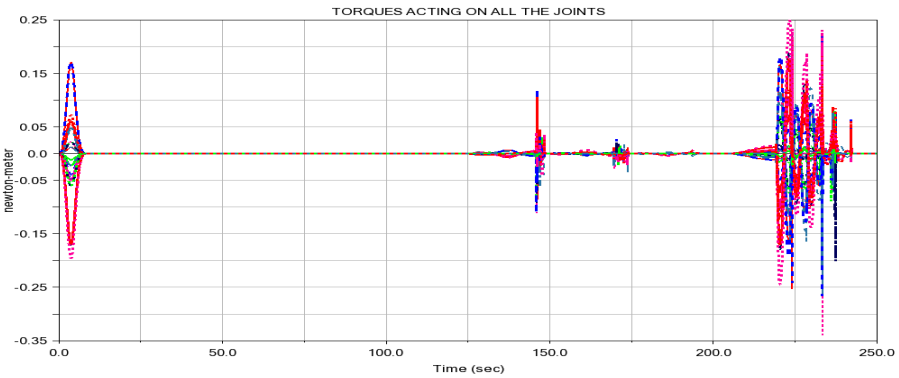

Figure 4.24: Torques acting on all hinges in the flexible model, dynamic simulation

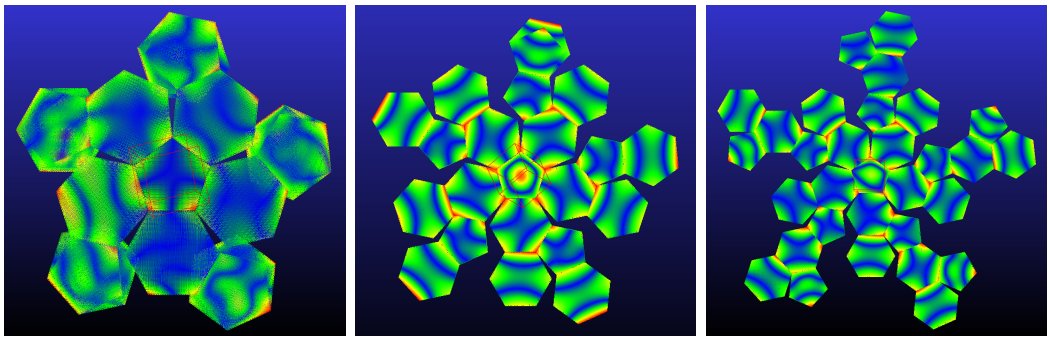

(a) Compact configuration (b) Deployment step 1 (c) Deployment step 2

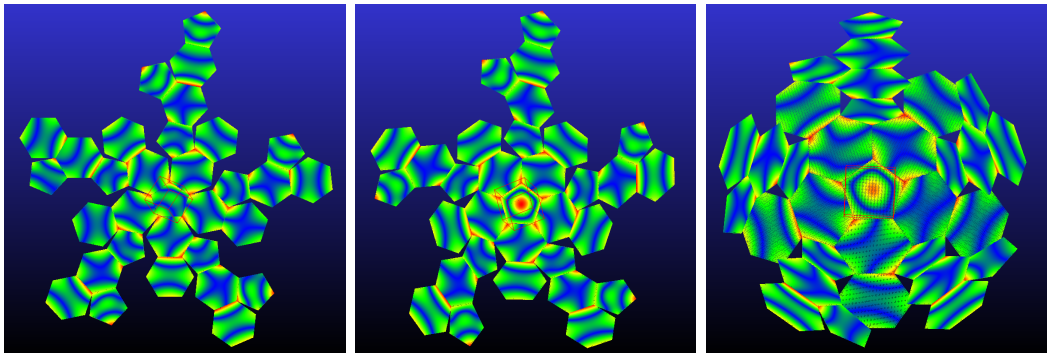

(d) Deployment step 3 (e) Capture step 1 (f) Capture step 2

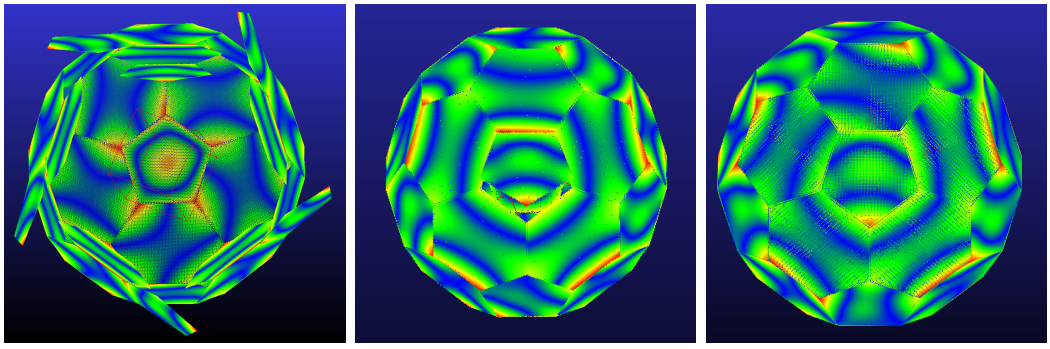

(g) Capture step 3 (h) Capture step 4 (i) Capture step 5

Figure 4.25: Frame of the dynamic simulation on flexible model

At this point, the same trends are reported as in the chapter 2.4 of the three alignment and tracking forces, as well as the relative distances and velocities in the three directions. This is done to demonstrate how the trends are indeed similar to the results of the kinematic analysis.

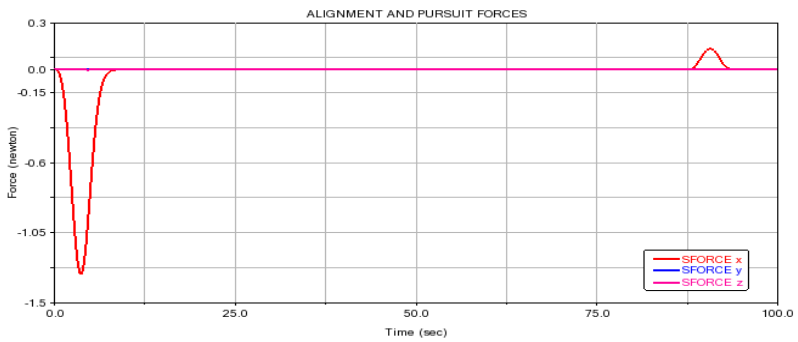

(a) Trend during alignment phase

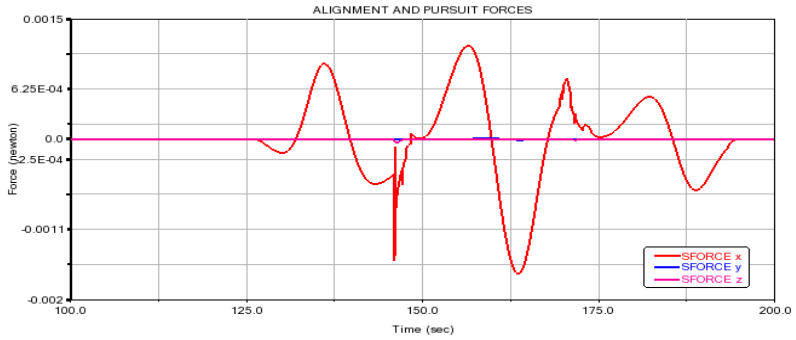

(b) Trend during deployment phase

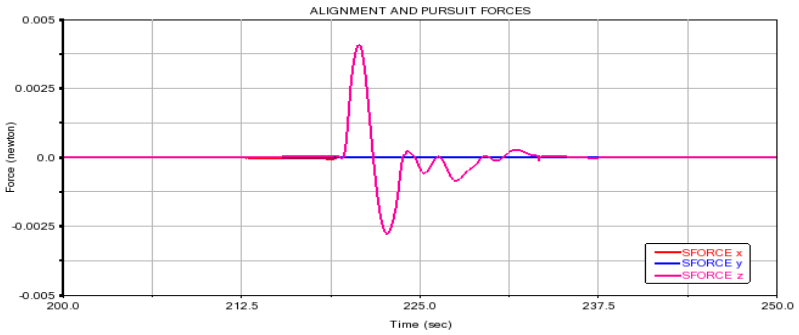

(c) Trend during capture phase

Figure 4.26: Trend of alignment and pursuit forces, dynamic analysis

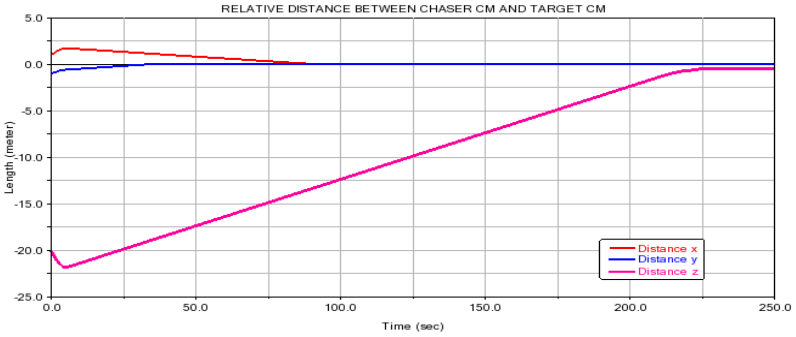

Figure 4.27: Relative distance between chaser's center of mass and target's center of mass, dynamic analysis

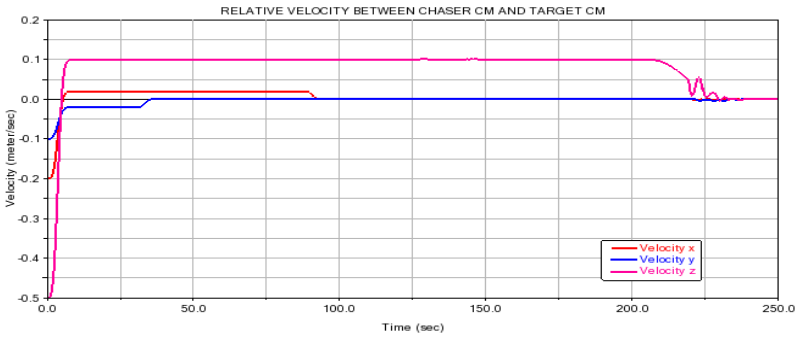

Figure 4.28: Relative velocity between chaser's center of mass and target's center of mass, dynamic analysis

At this point, the analysis is complete and meaningful conclusions can be drawn. In this study, the initial target position and speed were randomly assigned. The future goal is to automate the entire process so that the simulation is valid for any initial configuration of the target.
As discussed in this chapter, the only variables that influence the torque laws implemented via the *STEP5* functions are the minimum and maximum values assigned to these functions. The stiffness and damping parameters for the PD control system, on the other hand, have been calibrated as a function of the chaser geometry, which remains unchanged when the target's initial conditions change.
Therefore, it can be concluded that the process is entirely automatable. By storing only the minimum and maximum torque values from the kinematic analysis, the input parameters for the *STEP5* functions can be automatically estimated, as they will generally fall within a small range around these stored values. Once this is done, the corresponding dynamic simulation can be generated automatically.

4.4 Actuation system architecture

The results indicate that the maximum torque required to actuate the system is 0.34 Nm in absolute value, as illustrated in Figure 4.24.
It is now necessary to comprehend the implementation of the actuation system on the device. To this purpose, a comprehensive search was conducted to identify existing systems and assess their technological sophistication.
As presented in the [22], numerous examples of space applications of the company's components are exhibited in the actuation systems of various devices, including the Mars 2020 Perseverance Rover, the Mars Helicopter Ingenuity, the ExoMars, and others. This indicates the elevated reliability of these components, which are currently employed extensively in the space sector.

The device under consideration necessitates the utilization of rotary actuators to facilitate its deployment and subsequent folding for capture. Given its 32-plate configuration, interconnected by 31 hinges, the implementation of 31 actuators would necessitate mounting them, which would result in a substantial increase in weight. However, given the presence of symmetry across five fingers, a configuration involving five rotary actuators is selected, accompanied by a passive transmission system to facilitate movement across all plates. This is also possible because the actuation occurs in steps, meaning that each actuator is required to move at most two plates at the same time.

A rotary actuator is an electromechanical device consisting of:

- Electric motor, which generates high-speed rotation but low torque.
- Gear, which reduces speed while increasing output torque.

This basic system is integrated with position sensors for feedback and a controller for velocity and position control.
The motor and gearhead are mounted along the hinge axis.
Among the components available in the manufacturer's catalogue, not all are mutually compatible.

The selected electric motor is the EC flat brushless model with a diameter of 20 mm and integrated Hall sensors, enabling closed-loop control of both speed and position. This configuration offers greater precision compared to motors with integrated electronics, although it requires an external controller.
According to the datasheet [23], this motor provides a nominal torque of 7.59 mNm and a stall torque of 17.2 mNm.
Regarding the gear unit, it is necessary to select one that is compatible with the chosen motor and capable of delivering an output torque of at least 0.34 Nm.
Among the available options, the proposed solution is the three-stage GPX 22 UP planetary gearhead, with a diameter of 22 mm, Ultra-Performance version [24].
This configuration is the same as the one used in the Mars 2020 Perseverance Rover.
The selected gearhead features a reduction ratio R of 111:1, an efficiency of $\eta = 90\%$, and a maximum admissible torque of 4.3 Nm.
Therefore, the maximum output torque of the system can be calculated as:

$$T_{out} = T_{motor} \cdot R \cdot \eta = 1.71828 \ Nm$$

As can be observed, this value is lower than the maximum admissible torque of the gearhead, and, most importantly, it is significantly higher than the maximum torque required to actuate each of the device's plates. A conservative choice is made because this is a preliminary design, and several factors, such as the efficiency of the transmission system, are not considered in this study.

Another aspect to be verified is the space requirement of this configuration. According to the datasheets, the motor has a length of 14 mm, while the gearhead measures 41.9 mm. When both components are mounted coaxially, the total length amounts to 55.9 mm, which is significantly smaller than the 20 cm side length of the plates.
Based on the component datasheets, the EC flat motor has a mass of 22 g, while the GPX 22 UP gearhead has a mass of 95 g. This results in a total mass of 117 g for each actuator unit. Considering that five actuators are required for the full deployment system, the combined mass of the actuation units amounts to 0.585 kg. When added to the 18.76 kg mass of the chaser's deployable plates, the overall system mass reaches 19.345 kg. This value remains well within the limit defined by requirement `[R-PHY-010]`, thereby ensuring compliance.

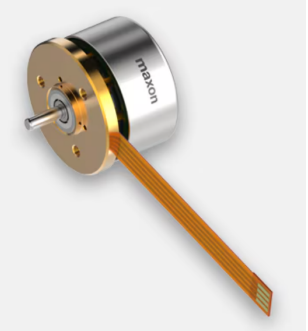

(a) EC flat motor

(b) GPX 22 UP gearhead

Figure 4.29: Actuators components

4.4.1 Sensor feedback and closed-loop control

In a controlled deployment and closure system such as the one proposed in this study, the adoption of sensors is an essential requirement to ensure the accuracy, controllability, and automaticity of the system [R-MECH-040].
Sensors are indispensable for the implementation of a closed-loop control system, wherein the system's operation is perpetually evaluated against the targeted values to rectify any discrepancies in real time.
The proposed mechanism is characterized by a sequential, step-by-step progression, with each subsequent step commencing upon the completion of the preceding one. Consequently, it is necessary to monitor the angle of rotation and angular velocity of each body, as provided by the implemented PD control.
An important advantage of this particular motor selection is that it incorporates Hall-effect sensors that are integrated into the motor's structure. These sensors detect changes in the magnetic field generated by the motion of the rotor and provide essential feedback on the rotation speed and relative angular position.

Within the context of a closed-loop control system, the system perpetually compares the measured angular position and speed with the desired values. The controller calculates a corrective torque based on the deviation (proportional term) and its variation over time (derivative term). This approach has been demonstrated to result in smooth and stable movement.

The presence of integrated sensors serves to reduce the necessity for external components, thereby simplifying the overall system design. Should greater precision be required in subsequent developments, it will be possible to integrate magnetic or optical encoders to improve the quality of position feedback.

4.4.2 Transmission system

To transmit the torque obtained from the five motors to all 31 joints, it was determined that a mechanical transmission with high-strength flexible cables was the optimal solution.
In particular, high-strength synthetic fiber cables, such as Kevlar® or Dyneema®, have found widespread application in the space field. These materials are characterized by a high strength-to-weight ratio and very high tensile strength, as well as a high tolerance to the extreme environmental conditions in which they must operate. The utilization of these components is predominantly for deployable systems.

The selected solution draws inspiration from the study [25], in which the authors present an innovative deployable boom based on a cable system.
This solution enables a substantial reduction in weight and footprint compared to solutions with rigid shafts. The authors designed the cable system to ensure that the necessary tension is maintained to facilitate efficient torque transmission.

In the configuration selected for this study, such a transmission is employed to avoid the use of rigid shafts, while maintaining the system's flexibility and lightness.
Another advantage is the capacity to transmit torque along intricate pathways. In this instance, the device is configured into five levels, where in the compact configuration. However, a thorough examination of cable tension is imperative to

avert a decline in efficiency.

A potential alternative to the aforementioned transmission system would be the implementation of a miniaturized actuator at each joint. While such a solution would undoubtedly be more precise, it would also result in a substantial increase in weight.

Below are some diagrams illustrating the chosen architecture, with particular focus on the positioning of the actuators (Figures 4.30b and 4.30c), as well as on the deployed and capture configurations.
The transmission system cables, originating from the gearbox outputs, can be seen connecting all the joints through flexible routing paths.

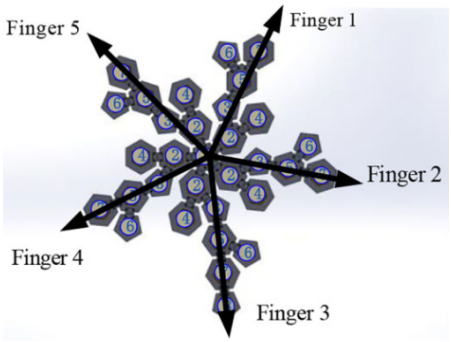

(a) Five-fingers simmetry [8]

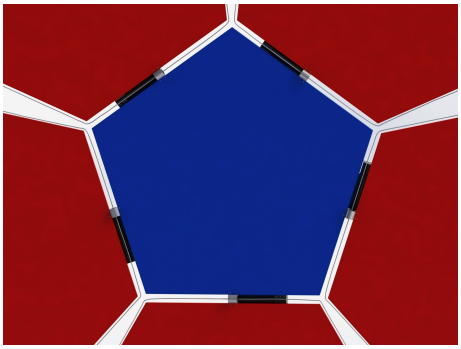

(b) Actuators positioning – front view

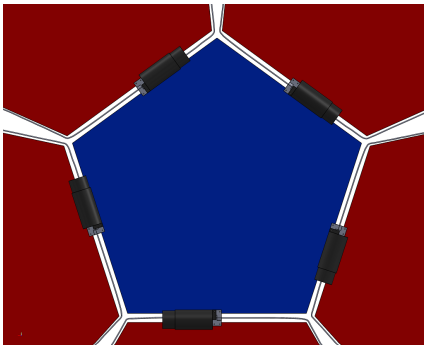

(c) Actuators positioning – back view

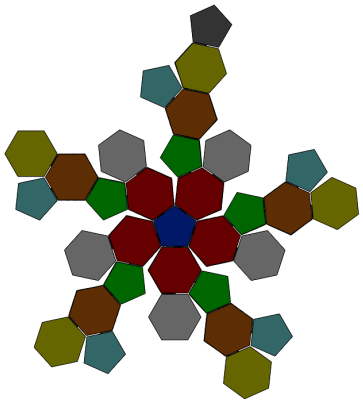

(d) Deployed configuration

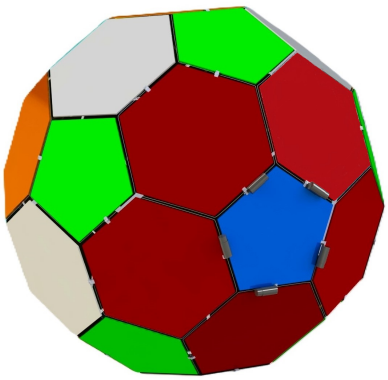

(e) Capture configuration

Figure 4.30: Architecture of the actuation system

A Simulink model has also been developed to provide a clearer understanding of the operation of the actuation system adopted in this work.
Figure 4.31a illustrates, as an example, the signal flow for the actuation of a single plate during the deployment phase. A signal input (*SENSOR_avv*) is provided to the actuators to initiate the deployment. The actuators generate a torque that follows a profile defined by the sum of three quintic polynomials (*STEP5*). This torque is transmitted through the system's cables, which are modeled as an ideal transmission line using a unitary *Gain* block in Simulink.
The plate is represented by a *Gain* block in which the inverse of its moment of inertia is entered. In this way, the applied torque is divided by the moment of inertia to compute the angular acceleration. Two *Integrator* blocks follow, converting the angular acceleration first into angular velocity, and then into angular displacement. The torque reaches the plate, where a sensor monitors its deployment angle. When the angle reaches 180°, the sensor is triggered and sends a signal to the PD control system. The desired angle is then maintained by the controller applying a torque via the actuators, thereby closing the control loop.

Figure 4.31b shows the same scheme, reorganized into functional blocks to better highlight the components of the system architecture.
An input signal is used to command the actuators, which generate the required torques. These torques are transmitted through the transmission system to all the joints of the chaser.
Each plate is equipped with a sensor that measures its angular position. Once activated, the sensor sends a signal to the controller, which in turn applies the torque computed by the PD control system.

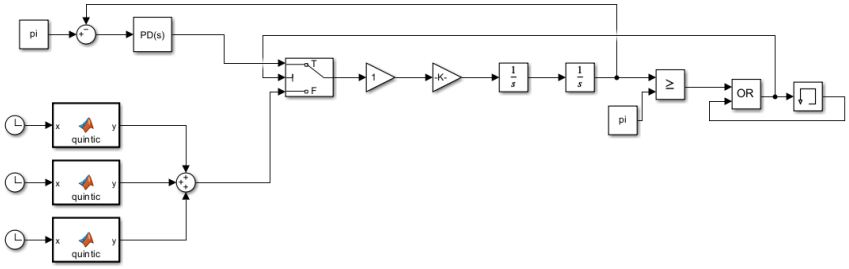

(a) Single plate actuation diagram

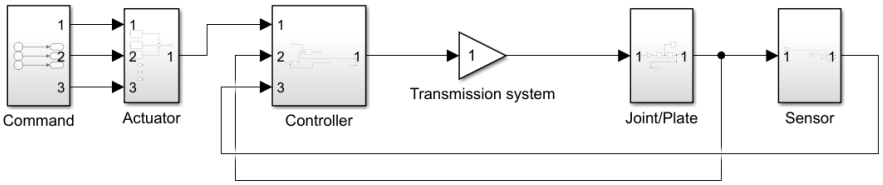

(b) Architecture block diagram

Figure 4.31: Simulink model

Chapter 5

Verification plan

The European Cooperation for Space Standardization (ECSS) ECSS-E-ST-10-02C standard [21] delineates the formal procedures for planning and documenting the verification of mission requirements in space projects.
In accordance with the ECSS-S-ST-00C guidelines [20], the requirements are formulated in accordance with the criteria of clarity, measurability, and verifiability, which are necessary for effective verification planning.
Verification planning and control are of the essence in ensuring that the system meets the stipulated design and mission requirements.
Verification planning is the process of formulating a comprehensive and coherent strategy for demonstrating product conformity to requirements. This strategy must include the selection of the most appropriate verification methodologies. Verification shall be accomplished by one or more of the following verification methods [21], `p.15-16`:

- **test**: measuring product performance and functions under representative simulated environments;
- **analysis**: performing theoretical or empirical evaluation using techniques agreed with the Customer;
- **review of design**: using approved records or evidence that unambiguously show that the requirement is met;
- **inspection**: visual determination of physical characteristics.

The Verification Plan (VP) serves as a foundational document, delineating the verification objectives, the requirements to be verified, the verification methods selected for each requirement, the acceptance criteria, the resources allocated for verification, and the temporal sequence of verification activities. The following attempt will be made to define a plan for the verification of the identified requirements. It is important to acknowledge that the document presented here is not a exhaustive VP document according to the ECSS standard, but rather a segment of it. The objective of this initiative is to establish a foundation for the subsequent development of comprehensive and essential documentation.
In accordance with the established ESA standards, the VP serves as the foundational element for the subsequent delineation of the Assembly, Integration, and Verification Plan.

The VP underscores the significance of establishing a clear link between each requirement and the corresponding verification activities. Each requirement must be explicitly linked to one or more verification methods, and the outcomes of these verifications must be meticulously documented and stored.
Another critical element that deserves attention is the time-related aspect of the process. It is imperative that the schedule aligns with the project's activities to facilitate the timely identification and resolution of any issues. The allocation of adequate resources is essential, with consideration given to the risks and costs associated with each activity.
The oversight of verification activities must encompass the monitoring of progress, the management of anomalies, and the review of results according to quality and safety objectives.
It is essential that all verification activities, encompassing test procedures, analysis reports, inspection reports, and demonstration results, are meticulously documented.
Due to its enormous importance, the VP is a document that starts to be drawn up at an early stage of the project. However, its integrity is subject to verification throughout the project's lifecycle. All modifications are meticulously documented and archived.
The subsequent step is to define the verification strategy for each identified requirement, specifying the methods chosen in compliance with the ECSS standards and justifying these choices according to the characteristics of the requirement itself.

5.1 Verification methods per requirement

R-MECH-010	The device shall complete full deployment within 75 seconds from the reception of the command

Given the absence of a physical prototype of the device, the verification of this requirement was planned through numerical analysis.
A dynamic analysis of the system in the simulated environment was conducted, from which the time required for the complete deployment of the device was extracted. Specifically, the sensor *SENSOR_avv*, which serves as a marker for the initiation of the deployment command, is activated after 123.67 seconds from the beginning of the simulation. The sensor *SENSOR_disp3* , indicating the completion of the final deployment phase, is activated at 193.34 seconds from the simulation's initiation. Therefore, the total time required to transition from the compact to the deployed configuration is 69.67 seconds, thereby substantiating the requirement.
However, a verification by testing is considered when the prototype will be realized.

R-MECH-020	The deployment of the device shall occur without abrupt discontinuities in velocity, ensuring a smooth and continuous motion profile

This qualitative requirement was verified by numerical analysis.
It was chosen to model the dynamic behaviour of the deployment by means of *STEP5* functions. This function approximates a step function by means of a quintic

polynomial, which has continuity in the first and second derivatives, i.e., in velocity and acceleration. This approach enables the avoidance of discontinuities and sudden peaks. A numerical analysis was conducted to assess the trend of angular velocities over time. This analysis revealed the absence of sudden peaks, as illustrated in Figure 4.11.

R-MECH-030	The device shall close smoothly, without any sudden or abrupt movements, and shall complete the capture process within 30 seconds

Also for this requirement, numerical analysis was employed to verify the requirement due to the unavailability of a physical prototype.
The concept of *smooth* was comprehended in this context as the absence of discontinuities in angular velocities. The closure phase was also modeled in the MSC Adams environment with *STEP5* functions.
In consideration of the temporal demands required to transition from the deployed to the capture configuration, an examination was conducted of the temporal points at which the sensors designated as *SENSOR_z* and *SENSOR_capt4* were extrapolated from the outcomes of the dynamic analysis. The first one is activated at 218.97 seconds from the initiation of the simulation, while the second one is activated at 242.23 seconds. Therefore, the total time is 23.26 seconds, which is consistent with the established requirement.
Once the prototype has been realized, verification by testing is scheduled to take place.

R-MECH-040	The device shall operate automatically

The method of verification selected for this requirement is numerical analysis.
In the mathematical model previously delineated, a system of sensors has been integrated to facilitate the automated initiation of each step.
The initiation of each subsequent step, whether it pertains to deployment or closure, is triggered by the completion of the preceding step, thereby eliminating the need for external intervention.
Consequently, the requirement can be considered verified.

R-MIS-010	The device shall be capable of capturing debris with dimensions up to $25 \times 25 \times 25$ cm^3 (equivalent to 15.6 dm^3) in LEO

Since no physical prototype is available, verification of the requirement was conducted by numerical simulation. A cubic target measuring $25 \times 25 \times 25$ cm^3 was modeled to represent the maximum size of the debris to be captured, in accordance with the mission requirement.
The analysis was conducted under conditions that were considered to be conservative, with the objective of ensuring the validity of the result.
At a subsequent stage of the project, verification is expected to be completed by conducting functional testing on a physical prototype.

R-MIS-020	The device shall not generate any debris during the mission, including during deployment, operation, and deorbiting phases

The verification of this requirement was conducted through numerical analysis, design review, and testing. The device was designed to ensure a controlled, continuous, and impact-free opening and closing mechanism.
However, as previously stated, the impact phase with the target was not thoroughly examined in this study, with the objective of enabling de-orbiting.
The chapter 6 offers several solutions to the presented problem. For a comprehensive verification of the requirement, we refer to the project's future developments.

R-STR-010	The device shall have a volume less than or equal to 35 dm^3 in its compact configuration at launch

At this preliminary stage, the requirement can be readily verified through analysis by calculating the volume using simulation software. In the subsequent stages, once a prototype has been fabricated, it will undergo a verification process that includes an inspection.
The volume was calculated from the maximum dimensions of the device in its compact configuration at the time of launch.
The device's dimensions are thus determined to be $1.32 \times 1.32 \times 0.02$ m^3, resulting in a volume of $34.848 dm^3$ and thereby confirming the requirement.

R-STR-020	The materials used in the structural components shall not exhibit delaminations under operational and environmental loads

In the preliminary phase of the project, this requirement can be verified by means of FEM analysis to assess the interlaminar stresses in the composite materials used and to identify any critical zones.
In the subsequent phases of the project, the use of non-destructive techniques, and therefore tests on the prototype, is envisaged to verify the absence of delamination during the operational phases.
However, this particular analysis was not part of this study. Therefore, the necessity of such an analysis will need to be verified in the subsequent phases of the project.

R-STR-030	The device shall be designed to endure the typical radiation environment encountered in Low Earth Orbit (LEO)

This requirement is verified through analysis and review of the design.
In this study, particular attention was directed toward the problem presented in this requirement by the selection of CFRP as the material of the plates, which are widely used in the space sector, also for its resistance in the LEO environment.
However, a more exhaustive thermal analysis will be necessary. This analysis will entail calculating the device's actual radiation exposure during its operational life. The *Space Environment and Effects Tool*, present within *Ansys STK* [26], will be utilized to perform this calculation.

R-PHY-010	The device shall have a mass that is less than 20 kg

The verification of this requirement is conducted at a preliminary stage using the estimate obtained from the geometric model created in the simulation software.
The findings of this study demonstrated that the mass of the realized model is determined to be 18.76 kg. Including the weight of the actuation system, the device has a mass of 19.345 kg, thereby partially verifying the requirement.
However, at a subsequent stage, when a prototype of the device is fabricated, the requirement must be verified by inspection of the product and measuring its actual mass.

R-MAT-010	The plates shall be manufactured using Carbon Fiber Reinforced Polymer (CFRP)

This requirement is linked to the parent requirement `R-STR-030`, which stipulates that the device's design must withstand the standard radiative environment of LEO orbit. The employment of CFRP is further driven by its demonstrated resilience to space radiation.
The verification of this requirement is carried out by inspection, accompanied by the review of pertinent documentation and certificates furnished by the supplier. These documents serve to substantiate the material's composition as CFRP.
However, a preliminary verification can be conducted through analysis, as CFRP has been incorporated into the FEM model as a plate material.

R-MAT-020	The plates shall be manufactured with a thickness of 0.125 mm

The verification of this requirement is conducted through inspection, encompassing the direct measurement of the thickness of the plates and the layers themselves during the manufacturing process.
At the preliminary stage of this study, a layer thickness of 0.125 mm is designated in the material definition of the FEM model. Consequently, an initial verification by analysis can be considered.
The utilization of CFRP enabled the conception of plates with sufficient thinness to meet the requirement `R-PHY-010`.

R-MAT-030	The laminate shall exhibit quasi-isotropic behavior

The requirement for quasi-isotropic behavior is achieved by means of a symmetrical and balanced stacking sequence (child requirement `R-MAT-040`) to avoid delaminations in the material (parent requirement `R-STR-020`).
The verification process entails numerical analysis, incorporation of a symmetrical stacking sequence within the material definition, and balanced oriented layers. Subsequent testing, involving mechanical examinations of the specimens, is employed to validate the performance of the material.

R-MAT-040	The laminates shall have a symmetric and balanced stacking sequence

This requirement is related to the parent requirement `R-MAT-030`. A symmetrical and balanced stacking sequence is employed to attain an isotropic behavior of the composite material.
This requirement is verified through a review of the technical documentation provided by the manufacturer. The quality of the finished product is verified through an inspection process that is carried out during and after the production cycle.
However, a symmetrical and balanced configuration of the laminate has already been defined in the FEM model. Therefore, a preliminary verification of the requirement by analysis can be considered to have been carried out.

5.2 Verification Matrix

The *Verification Matrix* is a fundamental tool in requirements management and verification.
In accordance with the guidelines in the ECSS, it is designed to facilitate comprehensive oversight of requirements and their verification. This approach is intended to ensure clarity during the system validation process and to enable streamlined review activities by the customer or the certification authority.
In the initial phase of a project, as is the case here, the fundamental matrix must contain the following elements [21], p.40-41:

- Requirement identifier
- Requirement text
- Traceability between requirement
- Levels and stages of verification
- Methods
- Link to the relevant section of the verification plan

In light of the stipulated requirements, an effort is underway to compile a preliminary Verification Matrix, which is expected to be instrumental for the successful execution of this project.

Req. ID	Text	Methods	Ver. status	Notes
R-MECH-010	The device shall complete full deployment within 75 seconds from the reception of the command	Analysis, Test	Partially verified	Adams simulation completed; Test scheduled
R-MECH-020	The deployment of the device shall occur without abrupt discontinuities in velocity, ensuring a smooth and continuous motion profile	Analysis	Verified	Adams simulation
R-MECH-030	The device shall close smoothly, without any sudden or abrupt movements, and shall complete the capture process within 30 seconds	Analysis, Test	Partially verified	Adams simulation completed; Test scheduled
R-MECH-040	The device shall operate automatically	Analysis	Verified	Adams simulation
R-MIS-010	The device shall be capable of capturing debris with dimensions up to $25 \times 25 \times 25$ cm^3 (equivalent to 15.6 dm^3) in LEO	Analysis, Test	Partially verified	Adams geometric model completed; Test scheduled
R-MIS-020	The device shall not generate any debris during the mission, including during deployment, operation, and deorbiting phases	Analysis, Review, Test	To be verified	-
R-STR-010	The device shall have a volume less than or equal to 35 dm^3 in its compact configuration at launch	Analysis	Verified	Adams geometric model
R-STR-020	The materials used in the structural components shall not exhibit delaminations under operational and environmental loads	Analysis, Test	To be verified	FEM Analysis for delamination prediction; Non-Destructive Testing
R-STR-030	The device shall be designed to endure the typical radiation environment encountered in Low Earth Orbit (LEO)	Analysis, Review	To be verified	Thermal analysis; Radiation environment analysis via STK SEET
R-PHY-010	The device shall have a mass that is less than 20 kg	Analysis, Test	Partially verified	Empirical evaluation completed; Inspection scheduled
R-MAT-010	The plates shall be manufactured using Carbon Fiber Reinforced Polymer (CFRP)	Analysis, Inspection	Partially verified	`R-STR-030` (parent) CFRP assigned in FEM model; Inspection scheduled post fabrication
R-MAT-020	The plates shall be manufactured with a thickness of 0.125 mm	Analysis, Inspection	Partially verified	`R-PHY-010` (parent) Laminate thickness set in FEM model; Inspection scheduled post fabrication
R-MAT-030	The laminate shall exhibit quasi-isotropic behavior	Analysis, Test	Partially verified	`R-MAT-040` (child), `R-STR-020` (parent) FEM model with quasi-isotropic lay-up; Machanical tests planned
R-MAT-040	The laminates shall have a symmetric and balanced stacking sequence	Analysis, Review, Inspection	Partially verified	`R-MAT-030` (parent) Symmetric and balanced lay-up set in FEM model; Review and Inspection scheduled

Table 5.1: Verification Matrix

Chapter 6

Open issues and future developments

Some aspects of the project remain to be investigated in future developments.
The project's potential developments are outlined below, along with some proposed solutions.

6.1 Low-velocity impact with the target

First, as previously mentioned, a significant issue to address is the contact between the chaser and the target.
This study focuses on the deployment and closing mechanisms of the chaser. However, once the target is captured, it must be braked to de-orbit, which is the mission's main objective.
Although this aspect is not discussed in detail here, possible solutions or hints for future work are provided.

Thanks to the improvements described in Section 2.4, it is possible to brake the chaser smoothly before capturing the target. As can be seen in Figure 4.28, the relative velocities are very low, on the order of 0.05m/s.
However, contact with the target cannot be avoided, even at low speed, so a solution must be found.
As far as the simulation is concerned, after introducing the flexible bodies, a different method of simulating contact must be employed. The *Impact* method used in the rigid-body model is not suitable. This is because the Adams algorithm calculates contact forces as follows:

$$F_n = K \cdot g^e$$

where g is the penetration of one geometry into the other. However, the chaser plates are modeled as two-dimensional bodies with two-dimensional shell-type elements, while the target is modeled as a three-dimensional body.
Even though shell-type elements permit penetration during impact, it is necessary to identify an alternative method for simulating this phenomenon, as the formulation is considerably more complex in the case of flexible bodies. Additionally, the target was defined with cubic geometry, which is characterized by its angularity. This angularity introduces numerical challenges during impact simulation, as the edges of the target intersect with the chaser plates.

Regardless of the simulation, other solutions can be adopted to improve the capture and deorbiting of debris.
The chaser plates are designed to be made of CFRP, an advantageous composite material that, like all composites, presents the problem of delamination. This issue can be mitigated by using certain laminations, as described in 3.2.1 and as has already been done. This lay-up also allows impact forces to be distributed more effectively.
However, CFRP is not a material that resists impact very well. Therefore, techniques can be employed to enhance its performance.

6.1.1 Ultrahigh molecular weight polyethylene fiber hybrid composites

The study [27] analyzes the mechanical behavior of hybrid composite materials consisting of CFRP and ultra-high molecular weight polyethylene (UHMWPE) under low velocity impacts.
UHMWPE has exceptional energy absorption capacity due to its plastic nature, fiber deformability, excellent abrasion resistance, and low coefficient of friction. The study evaluates how integrating UHMWPE layers within CFRP laminates improves energy absorption capacity and reduces impact damage.
Through experimental analysis, the author demonstrates that inserting alternating layers of UHMWPE between CFRP layers reduces the depth of impact damage, increases the penetration threshold, and results in less concentrated delamination. The author also shows that better performance is achieved using symmetrical configurations.
Another salient point in favor of this particular material is its high molecular weight, which consequently results in its low density of approximately 930kg/m^3. This density is lower than that of CFRP.
The adoption of a hybrid CFRP/UHMWPE configuration for the chaser plates would therefore increase the energy dissipation capacity during impact with the target, limit the propagation of damage due to impact, and avoid catastrophic delamination, which could occur in a pure CFRP structure.

If such a configuration were adopted, the insertion of layers of UHMWPE into the 32 layers of CFRP utilized to date would result in a laminate designated $[90/45/0/-45/\text{UHMWPE}]_{4sym}$. The utilization of a thickness of 0.125mm for each layer in the new material would result in a total thickness of 5mm for the plates.
In order to calculate the weight increase that would result from choosing this solution, one can consider a density of UHMWPE of $930 kg/m^3$. This results in a mass of 0.519 kg for the pentagonal plate and 0.7616 kg for the hexagonal plate. The chaser would then transition from a mass of 18.76 kg to 21.46 kg.
In the event that this solution is adopted, a parametric analysis must be conducted to determine the optimal compromise between performance and weight.
It is also necessary to evaluate the actual possibility of integrating entire layers of UHMWPE, or whether to insert it in a diffused form uniformly within the mix, or even only in the outer layers. The study [27] demonstrated that the incorporation of UHMWPE in quantities of 15g/m^2 led to the optimal maximization of energy absorption.

6.1.2 Short aramid fiber veil

An alternative approach to enhancing impact resistance and energy absorption capacity may be found in the study cited in the paper [28]. The authors evaluated the incorporation of interlaminar plies consisting of short aramid fibers (SAF) within CFRP laminates, which were neither bonded nor woven.
These plies, which are extremely thin (approximately 20μm), are placed between the CFRP layers prior to cure, without undergoing chemical treatment or being bonded with additional resin.
During the polymerization process, the plies are compressed and maintained in their position by the surrounding laminate layers.
The findings of this study demonstrated that the incorporation of these plies into the laminate composition led to an enhancement in the impact strength of the laminate and an improvement in the residual compressive strength.
Additionally, this method does not modify the conventional manufacturing process of CFRP composites and leads to an insignificant increase in mass, a crucial factor for the device analysed here.

In the study [28] a series of low-speed impact tests were conducted on CFRP panels. The behavior of the modified laminates was compared with that of unreinforced versions of increasing thickness. In the absence of SAF, the impact causes carbon fibers to escape and form a through-hole. The incorporation of aramid veils significantly alters the material's response. In thin specimens such as CF15-SAF6, which have a thickness of 3.18mm, the out-of-plane deformations are lower than in specimens with greater thickness that have not been modified.
The most favorable outcome was achieved with CF15-SAF12, exhibiting a thickness of 3.57 mm, resulting in a deflection reduction of 50.8 % compared to the corresponding CF15 specimen (2.92 mm). A positive effect was also noted on the damaged area, which was reduced in the case of the reinforced laminate.
The incorporation of SAF has been demonstrated to enhance the energy absorption capacity and restrict the propagation of damage. This solution is characterized by a negligible increase in mass, amounting to less than that of UHMWPE. However, the implementation of these two solutions in conjunction results in the creation of a hybrid laminate that exhibits a substantially enhanced low-speed impact resistance when compared to that of CFRP alone.

6.1.3 Kevlar®/carbon fiber sandwich composites

A further approach to increasing the energy absorption capacity of low-velocity impacts could be to use sandwich panels instead of simple CFRP panels. Sandwich panels have found widespread application in various engineering disciplines due to their unique structural design, which consists of two robust faces separated by a lightweight core material. This core, typically composed of foam or honeycomb, contributes to the panels' lightweight yet robust properties, making them suitable for a range of engineering applications. This configuration enables the attainment of elevated flexural rigidity while maintaining minimal mass. The fundamental principle underlying the utilization of sandwich structures entails the distribution of tensile and compressive loads across the walls, with the core functioning to enhance stress distribution.
The study [29] proposed an analysis of the increased energy dissipation capacity

due to impacts on structures of this type. The analysis focused on sandwich panels with a polyurethane foam core and CFRP outer faces. The objective of the present study is to evaluate the impact resistance and structural integrity of the panel after impact. To this end, the top plate of the panel is being modified by replacing some layers of CFRP with layers of Kevlar®.
Impact tests were conducted on sandwich panels of this type, and the results were compared with those obtained on plain CFRP faces.
The results obtained were subsequently analyzed by means of imaging techniques to assess the damage propagation modes.
The study demonstrated that sandwich panels composed of a CFRP/Kevlar® composite exhibited superior performance in comparison to panels with CFRP-only faces. These findings demonstrate a substantial reduction in visible and internal damage, an enhancement in residual compressive strength, and a reduction in delamination between the inner layers. Furthermore, the deformation on the back face was found to be more contained, and energy absorption was more distributed, thus avoiding local stress concentrations.
The introduction of Kevlar® contributes to two primary functions: first, it protects the external structure of the laminate, and second, it ensures greater strength in the post-impact phase. Consequently, this results in an increase in the fatigue life of the plates. This is a significant advantage in the case of the device under analysis in this work, given its expected operational lifespan in orbit.

In the study [29] sandwich panels with outer faces composed of four layers of CFRP were analyzed, replacing one, two, three and four layers with Kevlar® on the upper face. Furthermore, analyses were conducted on cases involving the integration of hybrid CFRP/Kevlar® layers.
The most optimal outcomes were achieved with hybrid panels with 1-2 layers of Kevlar®. Increasing the number of layers of Kevlar® would result in a greater capacity for energy absorption; however, this would also lead to a significant loss in terms of the stiffness of the outer faces.

Even without adopting sandwich panels, it is worth considering the replacement of a few layers of CFRP with Kevlar® in the plates of the device studied in this work. A calculation has been performed to estimate the variability in device mass. It can be posited that the device will replace four layers on the inner face of the plates that will impact the target. This would ensure the maintenance of the same thickness of 4 mm, while concomitantly enhancing performance in this regard. Kevlar® has a density of approximately 1440 kg/m^3. Consequently, the pentagonal plate comprising 28 layers of CFRP and 4 layers of Kevlar® would have a mass of 0.435 kg. In contrast, the hexagonal plate with the same configuration would have a mass of 0.657 kg.
Therefore, the total mass of the device would be reduced from 18.76 kg to 18.36 kg. This would result in a net savings of 0.4 kg, accompanied by an enhanced response to impact, despite a marginal decline in stiffness.

These methodologies represent potential solutions to the problem of impact with the target. A hybrid solution combining the three approaches could be considered, necessitating an analysis to identify the optimal compromise between weight, stiffness, impact resistance, and production cost.

6.2 Integration with an orbital servicing platform

The capture device developed in this work is designed to autonomously perform the phases of target tracking, deployment, and capture once released in orbit.
However, it must be initially transported and positioned by a dedicated servicing platform. This platform, which may be an orbital shuttle, or another type of carrier, plays a crucial role in deploying the system into an optimal proximity to the target.
Furthermore, after the capture has occurred, the platform may be required to retrieve the device and the captured debris to safely complete the de-orbiting phase. This operational architecture signifies a series of significant integration challenges, encompassing not only mechanical complexities but also electrical interfacing and mission planning.

The proposed approach offers significant advantages over conventional single-use debris removal systems. By enabling the recovery and reuse of the capture device, the system enhances both cost-efficiency and mission flexibility. Such capability allows multiple debris removal operations to be conducted within a single mission, reducing the need to launch a new spacecraft for each target. This modular strategy, which decouples the capture phase from the de-orbiting phase, facilitates scalable mission architectures that can be readily adapted to meet the growing demands of active debris removal in increasingly congested orbital environments.

Chapter 7

Conclusions

This work address the modeling of a system for active space debris capture based on origami principles. The proposed device is inspired by the geometry of the truncated icosahedron, as presented in the reference paper. This configuration combines compactness in the launch configuration with an effective spherical shape for the capture phase.

Starting from the foundation of prior work, the mission profile is optimized, focusing on the dynamics of debris pursuit, the deployment process, and the target capture sequence.
A multibody dynamic analysis is subsequently carried out using MSC Adams, aimed at the preliminary sizing of the actuation system. Starting from the results of the kinematic analysis, a mathematical model is developed to ensure smooth and controlled motion throughout all phases. To this end, a simple yet effective PD control system is implemented, based on sequential activations monitored by sensors.
To achieve a more realistic representation of the device's behavior, flexible bodies are introduced into the model using the CMS technique. The same dynamic analysis is then performed on this flexible-body configuration, confirming the consistency of the results.

Based on the outcomes obtained, an actuation system architecture with five independent actuators is defined, in accordance with the natural subdivision of the mechanism into five sections. The actuators transmit torque to the chaser joints through flexible cables, ensuring compactness and low mass. The integration of rotational sensors within the control architecture enables closed-loop operation and real-time monitoring of plates positions.

The work demonstrates the feasibility of the concept from both a dynamic and actuation standpoint, providing a solid foundation for future developments. A natural continuation of the project will involve the detailed modeling of the contact phase with the target and the study of its de-orbiting. Further material analysis will also be required, as suggested. Once the overall architecture is consolidated, the development of a physical prototype will be possible, to be tested in a controlled environment with the aim of validating the system for potential application in LEO.

Bibliography

[1] ESA Space Debris Office. *ESA Space Environment Report 2024*, Darmstadt Germany, July 19, 2024
Ref: GEN-DB-LOG-00288-OPS-SD
https://www.esa.int/Space_Safety/Space_Debris/ESA_Space_Environment_Report_2024

[2] Donald J Kessler and Burton G Cour-Palais. Collision frequency of artificial satellites: the creation of a Debris belt. *Journal of Geophysical Research: Space Physics* (1978-2012)

[3] Izzo D., Martens M., The Kessler Run, On the Design of the GTOC9 Challenge, Acta Futura, 2018 https://doi.org/10.5281/zenodo.1139022

[4] Responsible Space for sustainability, IAC 75th, Milan Italy 14-18 October 2024 https://www.asi.it/wp-content/uploads/2024/04/Gestione_rifiuti_spaziali_CardellicchioGiallongo.pdf

[5] Yan-Bin Jia. *Gaussian and Mean Curvatures*, Dec 10, 2024 https://faculty.sites.iastate.edu/jia/files/inline-files/gaussian-curvature.pdf

[6] Tanaka Yuto. An Origami-Inspired Deployable Space Debris Collector, *International Conference on Intelligent Robots and Systems (IROS)*. IEEE, 2023 https://doi.org/10.1109/IROS55552.2023.10341589

[7] Mastria, Gregorio. Supervisors: Alfonso Pagani, Daniele Catelani. *Analisi Multi-Corpo e Progettazione di un meccanismo di cattura per detriti spaziali e IOS basato su principi origami*. Master's Degree Thesis, Polytechnic of Turin, July, 2024

[8] Sun Chong, Wan Wenya, Deng Lisheng. *Adaptive space debris capture approach based on origami principle*. International Journal of Advanced Robotic System, November-December 2019 https://doi.org/10.1177/1729881419885219

[9] Cretella, Vincenzo. Supervisors: Alfonso Pagani, Afzal Suleman, Abdolrasoul Sohouli. *Topology Optimization of Origami Structures based on Crease Pattern and Axial Rigidity*. Master's Degree Thesis, Politecnico di Torino, October 2023

[10] Giodice, Maurizio. *Modellazione parametrica e comportamento meccanico di superfici adattive in architettura: analisi e sperimentazione*. PhD thesis in Structural and Geotechnical Engineering, Sapienza University of Rome, 2016/2017

[11] Gengxiang Wang, Zepeng Niu, Ying Feng. Article: *Improved Craig–Bampton Method Implemented into Durability Analysis of Flexible Multibody Systems*, 2nd February, 2023 https://doi.org/10.3390/act12020065

[12] Hexagon Manufacturing Intelligence, *MSC Adams View User's Guide, Version 2021.3*, 2021. link

[13] Hexagon Manufacturing Intelligence, *MSC Adams Solver User's Guide, Version 2021.0.2*, 2021. link

[14] Hexagon Manufacturing Intelligence, *MSC Adams Flex User's Guide, Version 2023.2*, 2023. link

[15] Hexagon Manufacturing Intelligence, *MSC Nastran 2022.1 Quick Reference Guide, Version 2022.1*, 2022. link

[16] H. B. Dexter, *Composite Materials for Space Applications*, NASA Technical Memorandum 103626, NASA Langley Research Center, 1991. https://ntrs.nasa.gov/api/citations/19910009925/downloads/19910009925.pdf

[17] International Organization for Standardization, *ISO 11567:2018 – Carbon fibre — Determination of filament diameter and cross-sectional area*, 2018. https://www.iso.org/standard/70573.html.

[18] ScienceDirect Topics, *Carbon Fiber Properties*. https://www.sciencedirect.com/topics/materials-science/carbon-fiber-properties

[19] Kapurch, Stephen J., ed. *NASA Systems Engineering Handbook*, DIANE Publishing, 2010. link

[20] European Cooperation for Space Standardization (ECSS) Secretariat, *ECSS System – Description, Implementation and General Requirements, ECSS-S-ST-00C Rev.1*. ESA-ESTEC, Noordwijk, The Netherlands, 15 June 2020. link

[21] European Cooperation for Space Standardization (ECSS) Secretariat, *ECSS-E-ST-10-02C Rev.1 – Verification*, 1 February 2018. link

[22] Drive Systems for Space Applications, Maxon Group, 2023. https://www.maxongroup.net.au/medias/sys_master/root/9227156127774/Space-Catalog-2023-EN.pdf?

[23] Maxon Motor, Motor EC Flat 20 Datasheet, 2025. https://www.maxongroup.com/maxon/view/product/motor/ecmotor/ecflat/ecflat20/351005

[24] Maxon Motor, Planetary gearhead GPX 22 UP Datasheet, 2025. https://www.maxongroup.com/maxon/view/product/gear/planetary/GPX/GPX22/GPX22-3-Stufig-UP/GPX22UPKLSL0111CPLW?

[25] Dong, K., Li, D., Lin, Q., Qiu, H., Cong, Q., Li, X. *Design and analysis of a novel hinged boom based on cable drive* Chinese Journal of Aeronautics, (2022), 35(3): 592–606 https://doi.org/10.1016/j.cja.2021.04.006

[26] Ansys, STK Premium (Space) *advanced analytical tools and higher f idelity modeling in the space domain*, 2022. STK Premium Product Sheet

[27] Zhou et al. *Low-velocity impact properties of carbon fiber/ultrahigh molecular weight polyethylene fiber hybrid composites*, Sep 21, 2023. https://doi.org/10.1002/pc.27760

[28] Yuan, B., Tan, B., Hu, Y., Shaw, J., & Hu, X. (2019). Improving impact resistance and residual compressive strength of carbon fibre composites using un-bonded non-woven short aramid fibre veil. *Composites Part A: Applied Science and Manufacturing*, Volume 121, 2019, Pages 439–448 https://doi.org/10.1016/j.compositesa.2019.04.006

[29] Gustin, J., Joneson, A., Mahinfalah, M., & Stone, J. Low velocity impact of combination Kevlar/carbon fiber sandwich composites. *Composite Structures 69* (2005), 396–406. https://doi.org/10.1016/j.compstruct.2004.07.020